

CLARKSON UNIVERSITY

**A 532 nm Chaotic Fiber Laser Transmitter for Underwater
Lidar**

A Thesis

By

Luke K. Rumbaugh

Department of Electrical and Computer Engineering

Submitted in partial fulfillment of the requirements

for the degree of

Master of Science

(Electrical Engineering)

23 April 2013

Accepted by the Graduate School

_____, _____
Date, Dean of the Graduate School

Report Documentation Page			Form Approved OMB No. 0704-0188		
Public reporting burden for the collection of information is estimated to average 1 hour per response, including the time for reviewing instructions, searching existing data sources, gathering and maintaining the data needed, and completing and reviewing the collection of information. Send comments regarding this burden estimate or any other aspect of this collection of information, including suggestions for reducing this burden, to Washington Headquarters Services, Directorate for Information Operations and Reports, 1215 Jefferson Davis Highway, Suite 1204, Arlington VA 22202-4302. Respondents should be aware that notwithstanding any other provision of law, no person shall be subject to a penalty for failing to comply with a collection of information if it does not display a currently valid OMB control number.					
1. REPORT DATE 24 APR 2013		2. REPORT TYPE		3. DATES COVERED 00-00-2013 to 00-00-2013	
4. TITLE AND SUBTITLE A 532 nm Chaotic Fiber Laser Transmitter for Underwater Lidar			5a. CONTRACT NUMBER		
			5b. GRANT NUMBER		
			5c. PROGRAM ELEMENT NUMBER		
6. AUTHOR(S)			5d. PROJECT NUMBER		
			5e. TASK NUMBER		
			5f. WORK UNIT NUMBER		
7. PERFORMING ORGANIZATION NAME(S) AND ADDRESS(ES) Clarkson University,8 Clarkson Ave ,Potsdam,NY,13699			8. PERFORMING ORGANIZATION REPORT NUMBER		
9. SPONSORING/MONITORING AGENCY NAME(S) AND ADDRESS(ES)			10. SPONSOR/MONITOR'S ACRONYM(S)		
			11. SPONSOR/MONITOR'S REPORT NUMBER(S)		
12. DISTRIBUTION/AVAILABILITY STATEMENT Approved for public release; distribution unlimited					
13. SUPPLEMENTARY NOTES					
14. ABSTRACT					
15. SUBJECT TERMS					
16. SECURITY CLASSIFICATION OF:			17. LIMITATION OF ABSTRACT Same as Report (SAR)	18. NUMBER OF PAGES 126	19a. NAME OF RESPONSIBLE PERSON
a. REPORT unclassified	b. ABSTRACT unclassified	c. THIS PAGE unclassified			

The undersigned have examined the thesis entitled '**A 532 nm Chaotic Fiber Laser Transmitter for Underwater Lidar**' presented by **Luke K. Rumbaugh**, a candidate for the degree of **Master of Science (Electrical and Computer Engineering)** and hereby certify that it is worthy of acceptance.

Date

Dr. William D. Jemison

Date

Dr. Abul N. Khondker

Date

Dr. Ming-Cheng Cheng

Date

Dr. Erik M. Bollt

CONTENTS

LIST OF TABLES	v
LIST OF FIGURES	vi
ACKNOWLEDGMENT	x
ABSTRACT	xii
1. INTRODUCTION	1
2. BACKGROUND AND LITERATURE REVIEW	6
2.1 Motivation	6
2.1.1 Problem Statement	6
2.1.2 Challenges in Underwater Operation	6
2.1.3 State of the Art	10
2.1.4 Desired Transmitter Specifications	13
2.2 Relevant Previous Work	15
2.2.1 Underwater Lidar Transmitters	16
2.2.1.1 Airborne Lidar	16
2.2.1.2 Water-based Ranging and Detection	18
2.2.1.3 Water-based Imaging	19
2.2.1.4 Water-based Communications	20
2.2.2 Laser Types	22
2.2.3 Modulation Waveforms	25
2.3 Proposed Transmitter Solution	27
3. THEORY AND SIMULATION	29
3.1 Chaotic Fiber Laser Transmitter Detailed Design	29
3.1.1 Fiber Ring Laser	29
3.1.1.1 Theory of Fiber Lasers	29
3.1.1.2 Ring Lasers as Oscillators	32
3.1.1.3 Temporal Output Signal	34
3.1.1.4 Signal Output Relation to Target Applications	35
3.1.2 Fiber Amplifiers	39
3.1.2.1 Theory of Fiber Amplifiers	39
3.1.2.2 Common Fiber Amplifier Designs	39

3.1.2.3	Amplified Spontaneous Emission and Amplifier Performance Limits	42
3.1.2.4	Amplifier Dynamics and Response to High Frequency Signal	43
3.1.3	Frequency Doubler	43
3.1.3.1	Theory of Second-Harmonic-Generating Crystals . .	43
3.1.3.2	Frequency Doubling System Design	44
3.2	Transmitter Calculations and Simulations	44
3.2.1	Fiber Ring Laser	44
3.2.1.1	Lasing Wavelength and Threshold (Analytical Solution)	44
3.2.1.2	Lasing Power and Efficiency (Analytical Solution) . .	47
3.2.1.3	Comparison of Performance of Various Designs . . .	47
3.2.2	Fiber Amplifiers	51
3.2.2.1	Pump Absorption and Small-Signal Gain (Analytical Solution)	51
3.2.2.2	Steady-State Signal Amplification in Saturating Conditions (Numerical Simulation)	52
3.2.2.3	Comparison of Steady-State Performance of Various Designs	54
3.2.2.4	Amplified Spontaneous Emission and Amplifier Limits (Numerical Simulation)	57
3.2.2.5	Modulated Signal Amplification Dynamics (Numerical Simulation)	57
3.2.3	Frequency Doubler	62
3.2.3.1	Efficiency and Output Power	62
3.2.3.2	Beam Shaping and Power Density	62
3.3	Applications and Proposed Implementation	66
3.3.1	Rangefinding	66
3.3.2	Channel Identification	67
4.	EXPERIMENTAL RESULTS	69
4.1	Transmitter Experimental Setup	69
4.1.1	Fiber Ring Laser	69
4.1.1.1	Feedback-Reflector Unidirectional Ring Laser	69
4.1.1.2	Lasing Threshold, Power, and Efficiency	69
4.1.1.3	Temporal Output Signal	70
4.1.1.4	Analysis of Chaotic Behavior	80

4.1.1.5	Implementation of Alternative Designs	84
4.1.2	Fiber Amplifiers	86
4.1.2.1	Two-Stage Core/Cladding Pumped Amplifier Chain	87
4.1.2.2	Amplified Spontaneous Emission and Amplifier Limits	89
4.1.2.3	Modulated Signal Amplification Dynamics	89
4.1.3	Frequency Doubler	89
4.1.3.1	Free Space Optical SHG Setup	89
4.1.3.2	Efficiency and Output Power	90
4.1.3.3	Beam Shaping and Power Density	92
4.2	Transmitter Experimental Results	92
4.2.1	Chaotic Fiber Laser Transmitter Setup	92
4.2.2	Performance Comparison to Simulation	93
4.3	Application Proof-of-Concept Experiments	95
4.3.1	High Resolution Ranging by Correlation	95
4.3.2	Channel Identification	98
5.	CONCLUSION	100
5.1	Transmitter Design and Experimental Results	100
5.2	Application Experimental Results	101
5.3	Future Work	102
	REFERENCES	104

LIST OF TABLES

2.1	Desired Transmitter Specifications	15
2.2	Comparison of Laser Technologies	22
2.3	Comparison of Wideband Modulation Waveforms	25
2.4	Proposed Transmitter Specifications	28
3.1	Fiber Ring Laser Calculation Parameters (Ytterbium)	48
3.2	Performance Comparison Between Ring Laser Designs	50
3.3	Performance Comparison Between Coupling Ratios (Reversing-Reflector)	50
3.4	Preamplifier Input Values	55
3.5	Preamplifier Output Values	56
3.6	Preamplifier YDFA Dynamic Simulation Parameters	59
3.7	Gain Amplifier YDFA Dynamic Simulation Parameters	59
4.1	1550 nm Feedback Reflector Ring: Components Used	70
4.2	1064 nm Premplifier: Components Used	87
4.3	1064 nm Gain Amplifier: Components Used	87

LIST OF FIGURES

1.1	Underwater Lidar Using Green Light	2
1.2	Applications for Chaotic Transmitter	4
2.1	Absorption and Scattering of Light by Water and Dissolved Particles . .	7
2.2	Scattering Geometry	8
2.3	Scattering Effects in Transmission and Imaging Systems	9
2.4	Frequency Dependence of Scattering Events	9
2.5	Airborne Lidar	17
2.6	Water-based Ranging and Imaging	18
2.7	Water-based Communications	21
2.8	Commercially Available Laser Diodes	24
3.1	Chaotic Transmitter Block Diagram	29
3.2	Rare-Earth Dopant Energy Levels	30
3.3	Rare-Earth Dopant Absorption and Emission Spectra	31
3.4	Laser Reflector Cavity	33
3.5	Laser Ring Cavity	33
3.6	Ring Laser Emission Spectrum	34
3.7	Mode Locking by Phase Coherency	36
3.8	Autocorrelation of Various Wideband Signals	38
3.9	Common Fiber Amplifier Configurations	40
3.10	Double-clad Fiber	41
3.11	Frequency Doubling Using Nonlinear Crystal	45
3.12	Example Gain Map for Ytterbium-doped Fiber Laser	45
3.13	Gain Maps Showing Effect of Parameter Variation	46
3.14	Laser LI Curve	48

3.15	Gain Map for the Reversing-reflector Ring Laser	51
3.16	Preamplifier Small-signal Gain	52
3.17	Preamplifier Steady-state Gain Saturation	54
3.18	Preamplifier Steady-state Gains for Varied Parameters	55
3.19	Preamplifier ODE Simulation Results	56
3.20	Gain Amplifier ODE Simulation Results	56
3.21	Fiber Amplifier Dynamic Simulations	61
3.22	Amplifier Dynamic Simulation Using 1 GHz Intensity Modulation . . .	61
3.23	Second Harmonic Generation Efficiency and Bandwidth	63
3.24	IR Beam Interaction with Crystal for Short and Long Rayleigh Lengths	64
3.25	Ranging Setup Using Chaotic Transmitter	66
3.26	Channel Identification Concept Using Broadband Signal with an Adap- tive Filter	67
3.27	Underwater Modulation Response Using Chaotic Transmitter	68
4.1	1550 nm Feedback Reflector Ring: As Built	70
4.2	1550 nm Feedback Reflector Ring: Gain Map for As Built Components	71
4.3	1550 nm Feedback Reflector Ring: Power Curve	71
4.4	Change in Output Signal Behavior with Pump Power (Long)	72
4.5	Change in Autocorrelation with Pump Power (Long)	73
4.6	Simultaneous Polarization Traces (Long)	74
4.7	Change in Output Signal Behavior with Pump Power (Ultralong)	76
4.8	Change in Autocorrelation with Pump Power (Ultralong)	77
4.9	Simultaneous Polarization Traces (Ultralong)	78
4.10	Comparison of Modes Between Long and Ultralong Cavities	79
4.11	Average Mutual Information	80
4.12	Average Mutual Information vs Autocorrelation	81
4.13	2D Phase Plots	82

4.14	3D Phase Plot	83
4.15	Frequency Spectra for Several Fiber Ring Laser Designs	85
4.16	Chaotic Transmitter Block Diagram	86
4.17	Amplifier Power Output Versus Launched Pump Power	88
4.18	Preamplifier and Amplifier Experimental Setups	88
4.19	Intensity Modulation Transmitted by Amplifier	90
4.20	Frequency Doubling Optical Setup	90
4.21	Frequency Doubling Crystal	91
4.22	Green Output Power Versus Infrared Input Power	91
4.23	Frequency Spectrum After SHG Doubling	92
4.24	Final Transmitter Detailed Setup As Built	93
4.25	Final Transmitter Performance As Built	94
4.26	Digital Correlation of Phase-shifted Waveforms for Ranging	96
4.27	Rangefinding Proof-of-concept Using Digital Receiver	96
4.28	General Transceiver Setup for Ranging and Imaging	97
4.29	Channel Identification Setup Using Broadband Signal	98
4.30	Channel Identification Results Using Noise and Chaotic Signals	98

ACKNOWLEDGMENT

*"Where there is no guidance the people fall,
But in abundance of counselors there is victory."*

— Proverbs 11:14

My first and most important thanks go to Jesus, for his friendship and patient help both in the last two years and throughout life, and to Cara, for being at once a wonderful support for me and the architect of a beautiful home to return to each day.

To William, Hudson, and Soraya: all my love, and my hope for you to find joy in whatever you try your hand at, whether Duplos or lasers.

This project has been blessed with good leadership, wide-ranging talent, and helpful supporters. It seems to me it must be unusual to be simultaneously so surrounded by goodwill and good engineers. Thanks to:

- Dr. William Jemison for his insightful guidance, patience, and excellence.
- Dr. Yifei Li (UMass Dartmouth) for many good ideas and helpful feedback.
- Dr. Bollt (chaotic analysis), Dr. Cheng (simulation), Dr. Khondker (laser modeling) and Dr. Yao (simulation) for their assistance in this work.
- Mark Southcott (mechanical engineering & IT) and David Illig (distasteful math & professoral aura) for their many and diverse contributions.
- Dr. Linda Mullen, Alan Laux, and Dr. Brandon Cochenour (all NAVAIR, Pax River, MD), for helpful discussions and for providing equipment and lab space for this work.
- Dr. Cetin Cetinkaya kindly provided the optical power meter and oscilloscope used to make the results shown.

This work was sponsored by the US Navy's Office of Naval Research under grant # N000141010906, and by the American Society for Engineering Education through the NREIP.

ABSTRACT

This project develops a new optical source for underwater ranging and imaging work. This source is based on an ultra-long cavity infrared fiber laser that generates a chaotic, wide bandwidth, high frequency signal, as is desirable for underwater applications. Amplification and frequency doubling of the infrared seed signal are performed to generate a green signal that can be used for underwater lidar. This transmitter is novel in that it offers high range resolution, high resilience to backscatter, completely unambiguous range, minimum dwell time, and no external modulator, while operating at high powers for long-range sensing.

The seed signal is generated by a fiber laser whose cavity includes a long passive fiber. This fiber forces the lasing of multiple, closely spaced longitudinal modes, which form a wideband intensity modulation on the infrared laser output, with a quasi-continuous power spectral density from DC to >1 GHz. This wideband signal has a sub-nanosecond autocorrelation peak and so offers high resolution for correlation-based ranging systems. Its high frequencies are also ideal for underwater work since they allow suppression of the backscatter. The laser exhibits several physical advantages: its modulation is generated internally, removing the need for external devices; it is light and compact; there are minimal heat dissipation concerns; and it is relatively insensitive to vibration or temperature. Finally, the system scales easily to high powers.

A ytterbium-doped fiber laser generates about 50 mW of this continuous-wave wideband signal at 1064 nm. Since water attenuates this wavelength quickly, a nonlinear crystal is used for second-harmonic generation, producing 532 nm green light. This crystal's efficiency increases quadratically with input power, so to achieve efficient frequency doubling the infrared signal is amplified to 5 W. This is done using two ytterbium-doped fiber amplifier stages, whose output is focused into the frequency doubling crystal. This single pass doubler generates a 50 mW green beam that is collimated and sent out for use in the water.

Analytical and numerical simulations are presented for fiber laser and the fiber

amplifiers. These results are compared to the experimental results. Nonlinear analysis is performed to characterize the chaotic properties of the experimental signal. Ranging and imaging system designs are proposed that leverage this signal's unique properties for high resolution unambiguous ranging underwater. Two proof-of-concept experiments are performed: the first demonstrates ± 2 cm ranging accuracy achieved with this signal, while the second uses the signal to estimate the response of an unknown channel.

CHAPTER 1

INTRODUCTION

Effective transmission of wide bandwidth signals through water is a requirement for many interesting applications. Imaging, rangefinding, water quality testing, communications, and 3D mapping can all benefit from high frequency wideband signals, and so there has been considerable interest in developing radio frequency (RF) wireless transceiver platforms for use underwater. Hybrid lidar-radar (HLR) approaches have shown great promise for such approaches [1], and we now present a novel HLR transmitter that is designed from the ground up for difficult underwater environments. This source is a chaotic fiber laser that uses fiber amplifiers and a frequency doubling crystal to generate a high power green signal for underwater lidar.

Lidar, or laser radar, employs a collimated optical signal (i.e., a laser) for highly directional illumination, and is well suited for use underwater [2]. Underwater imaging is often performed with diffuse light and wide angle cameras, but high power, directional lidar offers much better propagation through the water, and so increases imaging ranges. Likewise, diffuse sources can be used for communications, but the range is extended using lasers [3]. Sonar is used to great effect for coarse, long-distance rangefinding and mapping, but lidar offers unmatched spatial resolution and precision targeting. Lidar has much higher bandwidth than sonar for communications, as well as inherent security since the point-to-point transmission makes intercept unlikely [4]. In all its applications, lidar's unique advantages can augment existing technology and offer enhanced performance. Hybrid lidar-radar is an extension of lidar, in which the intensity of the laser source is modulated to provide bandwidth for enhanced performance. Radar signals are intensity-modulated onto the optical carrier, so that after the signal is transmitted and reflected off a target, information about the target can be deduced (similar to radar and lidar systems used in the air). Communications signals can also be modulated onto the carrier, just as in free-space or fiber optical systems. HLR has been shown to be effective

for rangefinding and imaging (as in Figure 1.1), but the underwater environment imposes unique requirements that must be carefully managed.

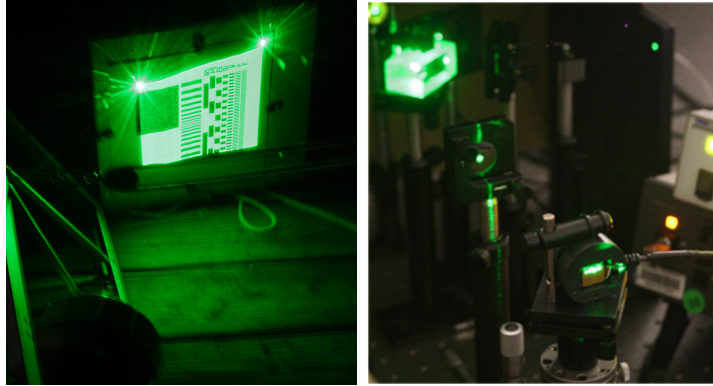


Figure 1.1: Underwater Lidar. Left: Hybrid lidar-radar imaging system. Right: Chaotic green optical signal generated in our lab.

In ocean optics, blue-green wavelengths are used to minimize absorption [5], and high-frequency signals are desirable for suppression of backscatter degradation [1]. (These considerations will be discussed in Chapter 2.) Traditional laser sources include solid-state, dye, and gaseous lasers [6]; these offer high powers in the blue-green, but they require external bulk modulators whose capacitance prevents operation at frequencies above the backscatter. Direct green diodes have only recently entered the market, and both their power and speed are currently marginal for underwater applications at significant range. Direct blue diodes are more mature, and can be used in the open ocean. However, blue is strongly absorbed in phytoplankton-dense shallow waters [7], and blue diodes are not efficient at high frequencies. Thus indirect infrared-to-green fiber laser based sources are the technology of choice for long-range work in rivers, harbors, and coastal settings [2, 8, 9]. Ytterbium-doped fiber lasers and amplifiers efficiently generate high power light at 1064 nm, and by doubling the frequency in nonlinear second-harmonic generating (SHG) crystals, 532 nm green light can be produced [10, 11]. Such “synthetic green” sources exhibit unique advantages: they need no external modulators; they are compact and lightweight; they have virtually no heat dissipation concerns; and they scale easily to very high powers [12]. Continuous-wave (CW) synthetic green transmitters have been demonstrated for high speed communications underwater [4], and

HLR synthetic green modulated pulse sources have been used for ranging and imaging [13, 14].

The synthetic green transmitter that we now introduce offers several advantages over previously published sources, due to its unique waveform specifically developed for high performance underwater. Its output has wide instantaneous bandwidth at high frequencies, and is completely non-repeating, with chaotically interacting modes [15]. By adding a long passive fiber in the ring cavity, we have enforced narrow mode spacing that has the effect of making the power spectral density (PSD) quasi-continuous from DC to >9 GHz, enhancing the chaos and sharpening the autocorrelation [16, 17]. This rich frequency domain content allows high resolution ranging, imaging, detection, and channel identification underwater. The laser's CW nature means there are no high-voltage gating or minimum range concerns, and as it is non-repeating it allows unambiguous range to arbitrary distances. Furthermore the signal is chaotic, which opens up new paths to securely encrypted ranging and communications [18, 19].

We demonstrate the usefulness of this transmitter for the listed applications by two proof-of-concept experiments. In the first, ± 2 cm accuracy is achieved for unambiguous ranging, imaging, and detection. In the second experiment, an "unknown channel" is identified using the transmitter in conjunction with an adaptive filter.

We present this novel source in full in the following chapters:

- Chapter 2: Background and Literature Review. We discuss the background motivation for wide bandwidth and high frequency signal sources, noting their advantages for transmission through turbid water. We present and evaluate existing means of generating these signals, and give the advantages of our new fiber laser source.
- Chapter 3: Theory and Simulation. Detailing the fiber laser source, we show system design including analytical and numerical calculations and simulations. We chart the path from low-power infrared to high-power green. Applications are proposed and system experiments outlined.
- Chapter 4: Experimental Results. We demonstrate the operational system

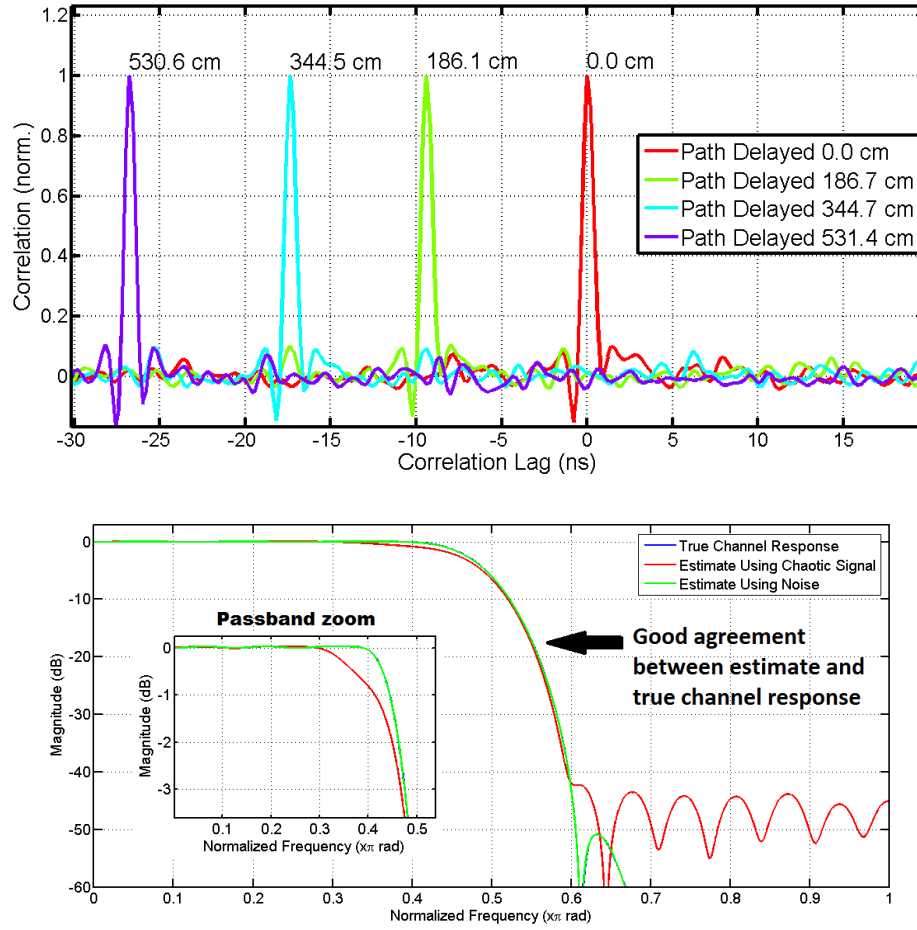


Figure 1.2: Applications for the Chaotic Lidar Transmitter. Top: Sub-centimeter ranging is achieved using the chaotic lidar transmitter and a digital receiver. Bottom: The chaotic signal can be used with an adaptive filter to estimate the frequency response of an unknown channel.

and give experimental results. We show how the seed signal is amplified to high-power infrared, and then frequency doubled from infrared to green (as in Figure 1.1). We characterize the hybrid lidar-radar signal of the system, including its chaotic properties. We present experimental results for ranging using this source, showing ± 2 cm accuracy in a proof-of-concept demonstration (Figure 1.2). Finally, we show how the transmitter can be used to determine the unknown frequency response of an underwater channel (Figure 1.2).

- Chapter 5: Conclusion. The contributions of this project to the fields of fiber

lasers, underwater ranging, and water science are enumerated. The next steps of improvement of this transmitter are noted, and future work proposed using this source.

CHAPTER 2

BACKGROUND AND LITERATURE REVIEW

2.1 Motivation

2.1.1 Problem Statement

Underwater imaging, ranging, and detection require a source that can deliver a useful signal to a target. On its return, the signal must be large enough to process, and processing must result in high-quality measurement data. Specifically, the received signal intensity should be clearly detectable in the presence of noise and clutter, with enough dynamic range to provide high resolution information about the target's reflectivity and its distance. High spatial resolution is required for multiple target detection and detailed imaging and mapping.

2.1.2 Challenges in Underwater Operation

These requirements can be difficult in the underwater environment because it presents two primary challenges: absorption and scattering [2, 5, 8, 20]. Most of the electro-magnetic spectrum is quickly absorbed underwater (see Figure 2.1). There is a window of dramatically increased transmission in the visible light spectrum, particularly at blue and green. Acoustic waves have even better transmission, which has been exploited for sonar that has performance on the kilometer scale [21, 22] (For comparison note that acoustic waves see typical absorption values between $10^{-5} m^{-1}$ and $10^{-2} m^{-1}$ depending on frequency) . However, light has the advantages of much higher bandwidth, and much lower dispersion angles than acoustic waves. Since bandwidth maps to precise time resolution, and low dispersion gives high spatial resolution, light is an attractive alternative to—or, complement to—sonar in short-range scenarios. In order to maximize range, optical sources should operate in the low-absorption blue-green region at high powers; the range achieved by a system will depend on the light receiver's sensitivity relative to the transmitter's initial power, the absorption of the water channel, and the dispersion of the light as it travels.

The dispersion of light from an uncollimated (i.e. diffuse) source is generally

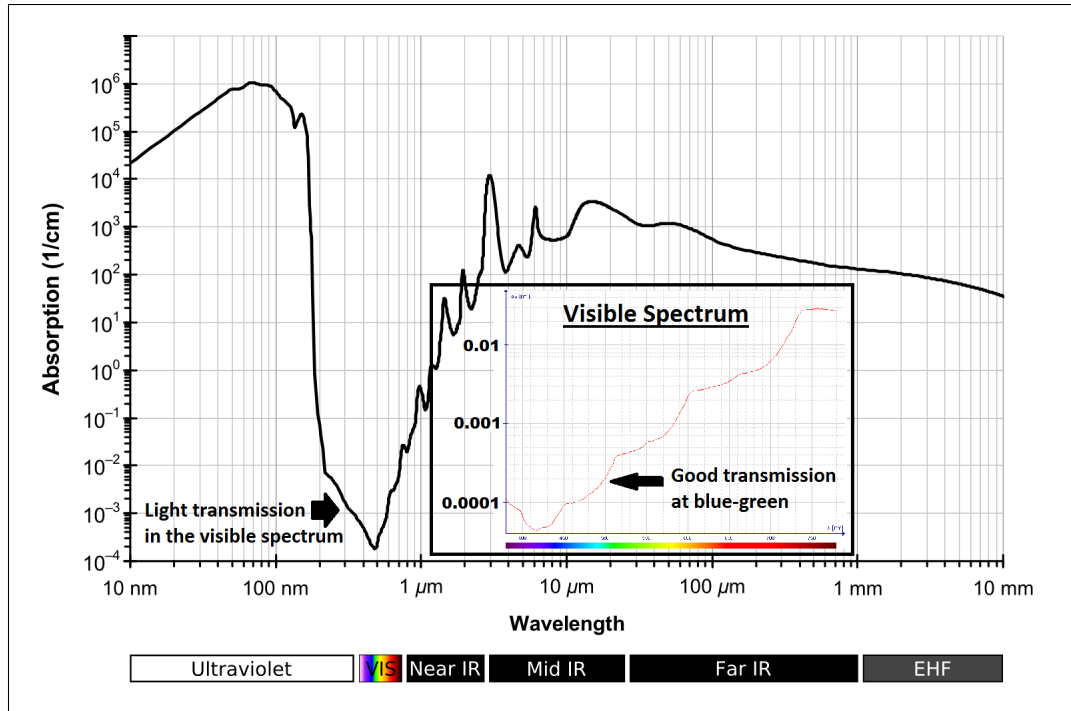


Figure 2.1: Absorption and scattering by water and dissolved particles. Top: Absorption coefficient of water versus wavelength for light; the blue-green region shows the lowest absorption. Bottom: Absorption and scattering values for sample water environments [5].

driven by the divergence angle of the light as it leaves the source. However, lasers generate collimated light with very low initial dispersion (i.e. beam divergence) angles, so the dispersion of the beam is primarily due to scattering in the channel medium. While pure water does scatter light, by far the larger scattering agent in real-world operation will be dissolved particles; the size, albedo, and density of these particles will govern the frequency and angle profile of scattering [5, 7, 22–24]. The number of scattered photons is of course proportional to the number of photons still in the beam, so much of the scattering occurs shortly after the beam leaves the transmitter.

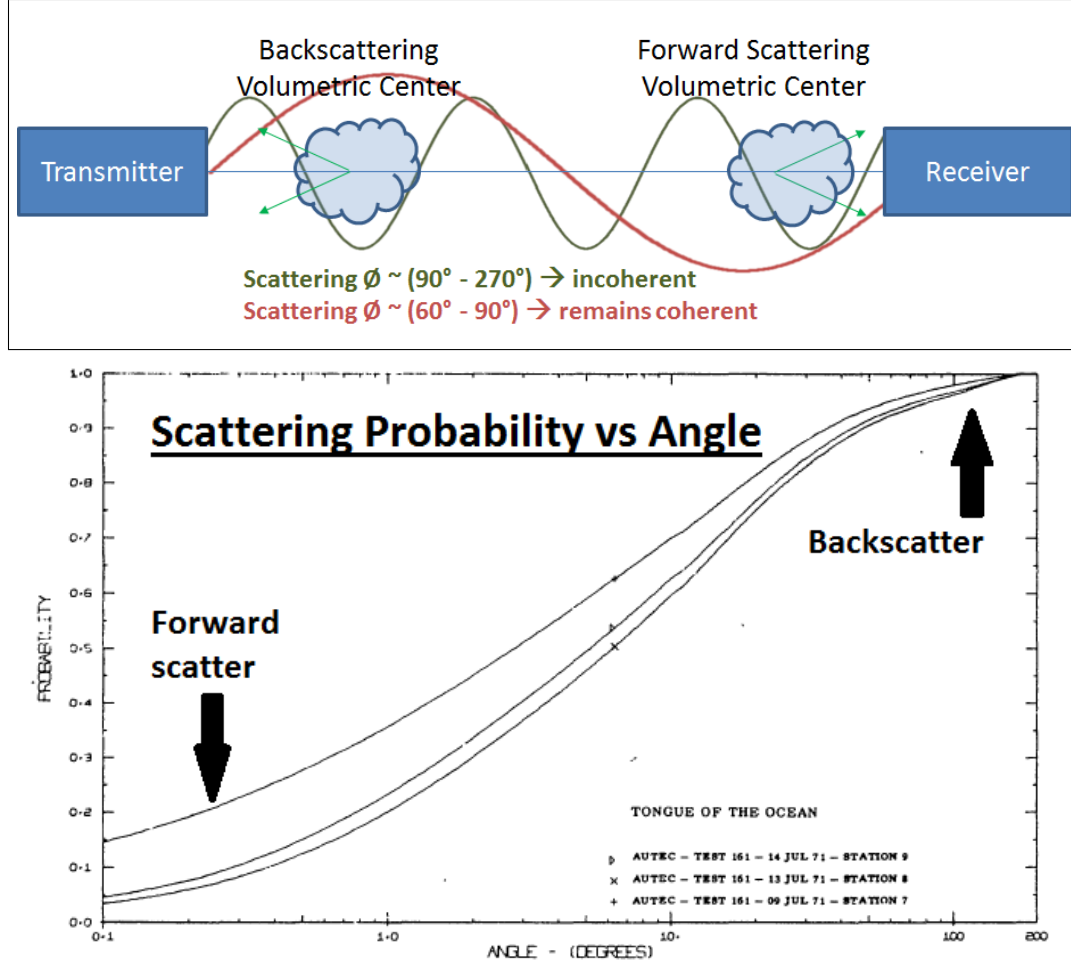


Figure 2.2: Scattering of light by water and dissolved particles. Top: Scattered photons detected by the receiver (“backscatter”) have different phases than the direct beam; the phase shift depends on the modulation wavelength. Bottom: Backscatter ($\sim 180^\circ$) is both the most probable and the least desirable scattering direction [23].

Absorption and scattering are typically described by exponential coefficients that represent the average number of photons absorbed, or scattered, per transmission length. These coefficients vary with water conditions (Figure 2.1). In the simple case where the receiver sees none of the scattered light, the received power is

$$P_{rx} = P_{tx} e^{-cz} \quad (2.1)$$

where P_{tx} is the transmitted power, a is the absorption coefficient, b is the scat-

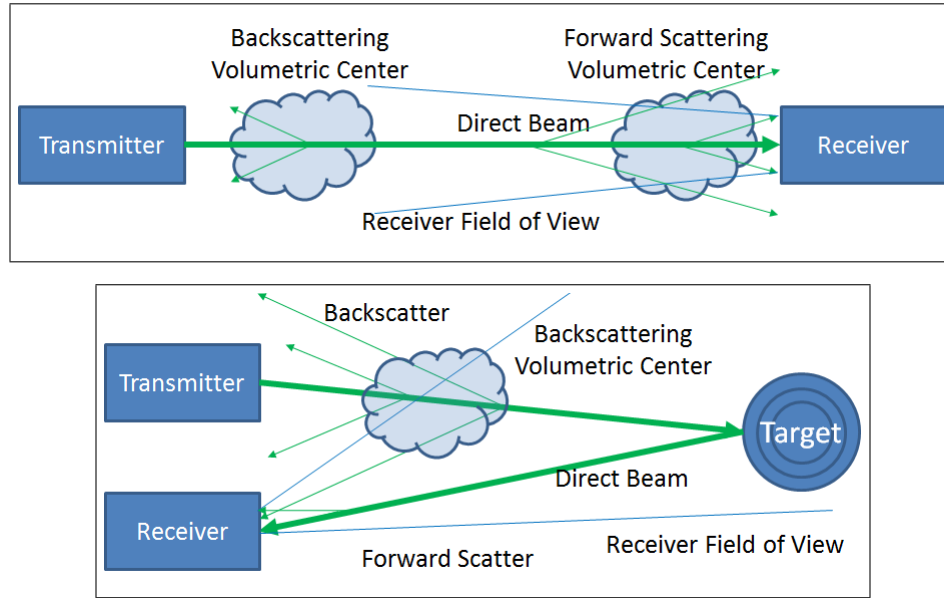


Figure 2.3: The effect of scattering in transmission (bistatic) and ranging/imaging (monostatic) applications. When the modulation wavelengths are long, scattering events have little effect on the phase. When they are short, the phase shift is significant. Top: Forward scattering introduces unwanted phase shifts in the bistatic case. Bottom: Backscattering dominates the monostatic case; at short modulation wavelengths the scattering can randomize the phase of the backscattered light, effectively making it look completely unmodulated.

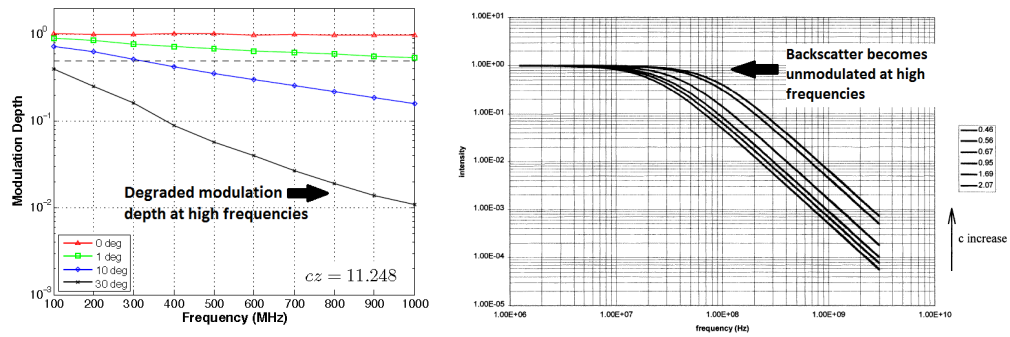


Figure 2.4: Frequency dependence of scattering events. Left: The effect of forward scattering is to degrade high modulation frequencies [25]. Right: Backscattered light may be modulated at low frequencies, but its modulation depth falls off exponentially as frequency increases [26].

tering coefficient, and $c = a + b$. In the more common case where the receiver does see a fraction k of the scattered light, the simple modification

$$P_{rx} = P_{tx} e^{-(a+b(1-k))z} \quad (2.2)$$

gives the correct power [27]. However, when we consider the case of an intensity-modulated light beam, scattering is of utmost importance because it changes the path length travelled by each photon (i.e. it performs a phase shift) and thus degrades the signal (see Figure 2.2). The concept of modulation depth must then be introduced to describe the *usable* signal light seen by the receiver. Briefly, the modulation depth m is the ratio of modulated light to unmodulated light:

$$m = I_{pp}/2I_{avg} \quad (2.3)$$

where I_{pp} is the peak-to-peak intensity swing of the light signal's modulation, and I_{avg} is the average intensity of the entire light signal. Scattering has the effect of decreasing the modulation depth, which can be conceptually thought of as reducing the signal-to-clutter ratio, or the contrast, of the signal, thus making detection of the target more difficult [28].

2.1.3 State of the Art

Lasers are coherent as well as collimated; therefore they not only allow high spatial resolution, but also extremely high temporal resolution by detection of the coherent wavefront location (as done in e.g. interferometry and optical coherent tomography where millimeter-resolution maps are required [29]). However, any scattered light seen by the receiver will have a different phase because of the scattering path change, and since the wavelengths are so short, even a small path change will essentially randomize the phase of a photon. Since interferometry is thus only possible in the most ideally clear waters, a more robust solution is to intensity-modulate the optical beam with a known radio frequency (RF) signal (as done in e.g. fiber optic communications). When the modulation imposed is a signal useful for range detection, such an approach has been termed Hybrid Lidar-Radar (HLR) [1, 30].

Common radar signals that can be used in HLR include single tone sinusoids, dual tones [31], frequency chirps [32], and modulated pulses [14]. Whatever the waveform, the HLR approach allows the receiver to determine the range to the target by some detection of the RF waveform, which has much longer wavelengths and is thus more robust against scattering by the channel. The temporal resolution of HLR is given by

$$\Delta t = 1/B_{rf} \quad (2.4)$$

where B_{rf} is the bandwidth (maximum RF frequency minus minimum RF frequency) of the modulation (not of the optical carrier). Thus there is a strong motivation to operate at wide bandwidths.

The RF coherence in HLR is much less sensitive to scattering than the optical coherence in interferometry, simply because the wavelengths are 10^6 times longer. However, as the modulation frequencies get high enough, the wavelengths shorten until they are on the order of scattering events; that is to say, a once- or twice-scattered photon will have a phase that is essentially random compared to the unscattered “direct” beam [25]. Figure 2.3 illustrates this problem for both bistatic and monostatic applications. In a bistatic (i.e. point-to-point) transmission arrangement, it can be intuitively understood that scattered light seen by the receiver will have an invalid phase if the additional path length due to scattering is a significant fraction of the transmitted wavelength, and that scattered light is thus clutter that must be removed or it will degrade the signal [22, 27, 28]. Folding this arrangement back on itself, the monostatic case will see a similar effect on the round-trip reflected light, but the primary concern is the backscattered light [33, 34]. Since most of the backscattering happens close to the receiver, backscattered photons may all travel similar path lengths, and thus their phases may be similar if the modulation wavelength is long. In this case, the backscatter can appear as a point target that is much stronger than the actual target. However, if the modulation wavelength is short, the backscatter phases will be randomized, so that the backscattered light will look like unmodulated DC. When this occurs, the backscattered light can be removed from the signal simply by splitting the signal into its modulated RF and

unmodulated DC components (easily done with a frequency filter after the beam has been detected and converted from optical to electrical). Thus, while scattering can degrade a signal, high modulation frequencies allow discrimination between scattered and direct light. In light of this, HLR systems should be designed to operate at high modulation frequencies.

The pitfall of high modulation frequency is ambiguous range. Ambiguity in a range measurement occurs when the round-trip time of flight to a target is longer than the period of the modulation signal. In this case, there is no way to determine to which period a measurement belongs; is a phase measurement of e.g. 30° from a target at 30° round trip distance away, or at $(360 + 30)^\circ$, or $(720 + 30)^\circ$? The maximum unambiguous range to a target is given by $R = c_0 T/2$, where c_0 is the speed of the waveform in the medium and T is the repetition period of the modulation. An ideal HLR modulation scheme would be completely non-repeating; short of this it would use a long period for an unambiguous range much greater than the anticipated maximum operating range.

Successfully demonstrated HLR systems have taken several forms. The most mature are single-tone continuous-wave (CW) transmitters, which have been most effective at high frequencies [34, 35]. Double-tone CW implementations have been used to significantly extend the unambiguous range. [31] “Slow-pulsed” systems measure the time of flight to obtain target distance [36]; fast pulse trains mimic CW in suppressing backscatter but have higher peak powers [28]. Modulated pulse (MP) sources are very promising, as they combine the high peak powers of pulsed lidar with the unambiguous range and temporal resolution of high bandwidth CW [13, 14, 37]. Psuedo-random noise (PRN) schemes, frequency-modulation CW (FMCW), and stepped frequency-domain reflectometry (FDR) [32] have also been proposed as means of increasing temporal resolution while maintaining long ambiguous range.

Current systems generate these waveforms in several ways. Mode-locked lasers produce fast pulses directly in the cavity; frequency-doubled infrared (1064 nm to 532 nm) mode-locked sources have been the single most common transmitter used in water sensing [2, 36, 38, 39]. CW modulation can be produced by sending a CW beam from a solid-state laser into an electro-optic crystal modulator. Alternatively, direct

modulation of diode feed current is possible by impedance matching the RF signal voltage to the diode input [35,40]. Finally, modulated pulses can be produced either by exciting a mode-locked laser with an RF source [1], or by intensity-modulating the output of a mode-locked fiber laser [13,14].

2.1.4 Desired Transmitter Specifications

All HLR systems attempt to maximize power and minimize absorption. They all make trade-offs between mitigating backscatter by operating at high frequency, while trying to maintain a long unambiguous range. Wide bandwidth is desired to maximize temporal resolution.

Specific values constrain any HLR transmitter design. These include link budget concerns (i.e. power):

- Desired operating range. Most systems would look for performance to at least 5 m round trip, and hope for 10-20 m even in turbid waters. This is usually cast in attenuation lengths, where ranging or imaging at >10 total attenuation lengths is considered a good performance [9,41].
- Exponential power decrease. Typical coastal attenuation coefficients c are between 0.5 and 2.5 m^{-1} . At $c = 2.0 \text{ m}^{-1}$, 5 m represents 10 attenuation lengths (here $L = cz$), so the received power $P_{rx} = P_{tx}e^{-10} = 45 \times 10^{-6}P_{tx}$. At 10 m, $P_{rx} = 2 \times 10^{-9}P_{tx}$. Thus the transmitted power must be much higher than the needed power at the receiver.
- Receiver sensitivity and bandwidth. Commercial avalanche photo diodes (APDs) can detect RF modulation from DC to 1 GHz on signals in the range of 10 nW [42]. This allows 10 attenuation lengths at $P_{tx} < 1 \text{ mW}$, or 20 attenuation lengths for $P_{tx} = 6 \text{ W}$. Commercial photomultiplier tubes (PMTs) have much better sensitivity but typically very low bandwidth — though at least one custom PMT has been reported to have performance to 1 GHz with photon-counting sensitivity [28,43].
- Receiver dynamic range. Low modulation depth is typical; the desired signal may be thousands of times smaller than the backscatter, in which case the

receiver must have enough dynamic range to detect the signal (at the bottom of the range) without being saturated by the backscatter (at the top). This depends on desired operating range: most backscattered light will travel <4 attenuation lengths [44], so if operation is desired at 10 lengths, the backscatter-to-signal ratio will be at least $e^{-4}/e^{-10} = e^6 = 403 = 26$ dB. At 20 lengths, the dynamic range must be at least $e^{14} = 1.2 \times 10^6 = 61$ dB. This is mostly a receiver issue, but should be understood by the transmitter designer.

Effective ranging and imaging requires consideration of additional factors:

- Temporal resolution. The resolution of a measured time to target is inversely proportional to the modulation bandwidth by $\Delta t = 1/2B_{rf}$. Since sensitive receivers are currently limited to 1 GHz bandwidth, resolution will be no smaller than 0.5 ns, or 11 cm range resolution (speed of light $c_{water} = c_0/1.33 = 2.25 \times 10^8$ m/s). Smaller bandwidths will see correspondingly larger resolutions.
- Unambiguous range. The farthest distance that can be unambiguously ranged using periodic signals is determined by the repetition period of the waveform, and is $R = c_0T/2$. For signals with discrete frequency steps, the maximum unambiguous range may be further restricted by $R = c_0/2\Delta f$, where Δf is the distance between discrete frequencies. Thus a single tone CW modulation of 100 MHz gives an unambiguous range of 11 m, while dual tones of 100 MHz and 110 MHz give a much safer $R = 110$ m. FMCW with a 1 MHz baseband signal will have $R = 1100$ m; FDR using 10 MHz steps gives $R = 110$ m. Noiselike waveforms offer completely unambiguous ranging: a 32-bit PRN code at 1 GHz repeats in 4.3 seconds for a theoretical range of 6.4×10^8 m, while chaotic signals never repeat.
- Backscatter. The magnitude of still-modulated backscattered light resembles a low-pass filter with a cutoff frequency f_{co} between 10 and 100 MHz (where f_{co} is increasing linearly with the turbidity) [26]. The magnitude that is still modulated then falls off exponentially at about 20 dB/decade. For a turbidity $c = 2.0 \text{ m}^{-1}$, $f_{co} = 80$ MHz, so the modulated backscatter will be 40% of

its original value at 100 MHz modulation, while at 300 MHz just 6% of the backscattered signal remains modulated (the rest having “washed out” to DC).

- Pixel dwell time. The number of pixels in an image n_{pixels} , and the desired image refresh rate f_{image} , dictate the length of time per pixel by $t_{pixel} = n_{pixels}/f_{image}$. For a 640x480 pixel image refreshing at 1 Hz, just 3 μs can be used to process each pixel. Any transmitter waveform used must then run at least at 300 kHz (and correspondingly faster for large images or faster refresh rates).

Using these constraints, some example specifications may be drafted.

Table 2.1: Desired Transmitter Specifications

Parameter	Baseline	Desired	Performance (Assumptions)
Power	50 mW	10 W	Allows 13 or 18 att. lengths (100 nW at RX)
Frequency	200 MHz	500 MHz	Backscatter at 15% or 2% mod. ($c = 2.0$)
Bandwidth	200 MHz	800 MHz	Resolution 50 or 13cm
Dwell Time	10 μs	1 μs	Refresh rate 1/3 or 3Hz (640x480p)
Rep. Rate	50 MHz	10 MHz	Unambiguous range 22 or 110m

While these values are just samples, they indicate desired performance and thus inform the selection of transmitter waveforms and technologies.

2.2 Relevant Previous Work

Proposing a new transmitter requires both an understanding of what has been implemented before, and a grasp on the options available. In this review we will discuss some of the many useful laser systems that have been built to perform imaging and ranging, and note their compatibility with the specifications outlined above. A vast majority of existing systems operate in free space; a small fraction have been designed specifically for underwater work. We will concentrate on these underwater systems, while noting opportunities to leverage techniques from the mature and rapidly advancing worlds of free space lidar and radar.

This review will first cover existing underwater systems, and discuss where opportunity for improvement may lie. Thus motivated, a decision chain follows. Selections

of laser type, waveform family, specific signal, and laser topology must be made in turn, and the options and factors for each selection are discussed. Selection of supporting technology (in our case, amplifiers and frequency doublers) is treated briefly.

2.2.1 Underwater Lidar Transmitters

Previously published lidar systems for underwater work can be placed in one of four categories.

1. Air-to-water surveillance lidar.
2. Water-to-water ranging and detection.
3. Water-to-water imaging.
4. Water-to-water communications.

While the applications are distinct, many of the specifications are the same. For convenience, it is still helpful to review existing systems category by category. Note that we will only briefly mention diffuse sources, including LEDs, projectors, and flashbulbs, since they are designed for wide field of view (FOV) operation in clear water, at short working distances [2,8,9,41]. There is little overlap in specifications for this similar, but distinct, application space.

2.2.1.1 Airborne Lidar

Airborne lidar (also termed “aerial laser hydrography” or “aerial laser bathymetry”) was introduced in the 1965 by NAVAIR (at NADC Warminster, Pa.), and developed by the American and Australian militaries for reconnaissance [46–48]. It has been successfully transferred to commercial and civil applications as well, with the capability of wide-coverage mapping of coastal and riverine structures using high-power slow-pulsed lasers [49–52]. Typical systems use mode-locked Nd:YAG solid-state bulk lasers (discussed below) with frequency doubling from the near infrared (NIR) to green, achieving >5 mJ pulses at 1-500 kHz repetition rate (where the rep. rate is adjusted based on desired maximum range). Both infrared and green are usually

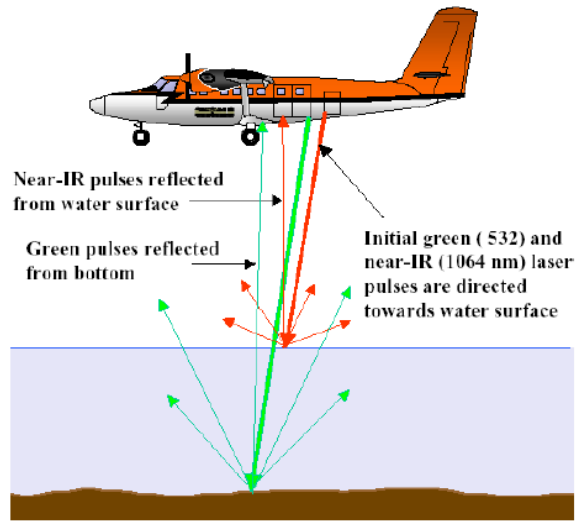


Figure 2.5: Airborne lidar using frequency-doubled 1064 nm pulses. This is common for wide-area surveillance and coastal mapping (Image [45]).

transmitted together; the infrared gives a strong return at the air-water interface, while the green penetrates the water and allows detection of scattering particles, submerged objects, and the seafloor/riverbed. (A particularly exotic application of this NIR/green pulsing approach was realized on NASA’s Global Laser Altimeter System (GLAS) in 2003, a satellite-based pulsed system that recorded cloud, vegetation, ice, and land topography for 7 years before pump diode failure forced it into retirement.) Recent innovations in airborne lidar include “full-waveform” systems, which use GHz data acquisition and processing rates to achieve <10 cm ranging resolution, and sophisticated signal processing to compensate for the challenge of imaging from a moving platform [45]. Comparing these slow-pulsed systems to the desired specifications outlined, we note that while their powers and unambiguous ranges are significant, their unmodulated waveforms do not provide for any frequency-domain separation of signal from backscatter, and so their application is limited in turbid waters. (Commercial maximum range specifications are between 1 and 3 Secchi disks, i.e. 1.7 and 5.1 attenuation lengths.) Thus these transmitters do not have the frequency content necessary to meet our range specifications.

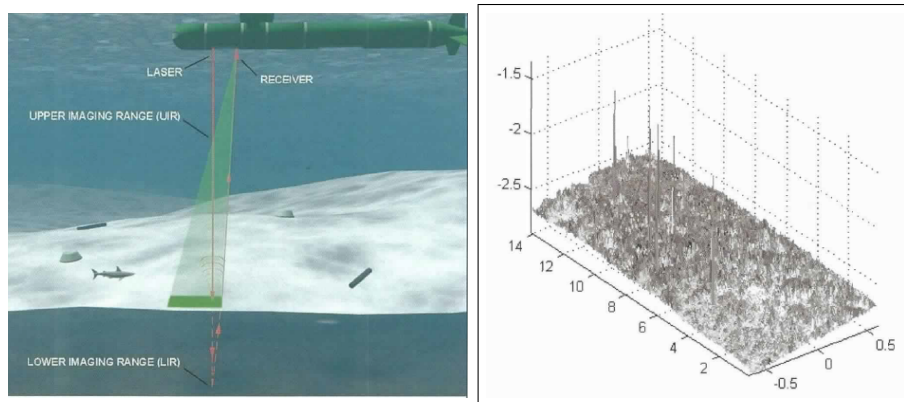


Figure 2.6: Water-to-water ranging and imaging systems. Left: Concept for submarine-based minesweeping, floor-mapping. Right: Millimeter resolution 3D image of seafloor grasses collected by UCSD's 3D Sea Scan system (Images [9]).

2.2.1.2 Water-based Ranging and Detection

Water-based lidar systems used for ranging and detection are designed for high range resolution. As we have seen, this dictates high frequencies, so that the means of backscatter reduction is readily available. In order to achieve unambiguous ranging, some low frequency content must be present as well, so high bandwidth is necessary. Dwell time is not usually a restricting consideration for pure ranging and detection systems. Slow-pulsed time-of-flight systems are the most traditional approach to ranging, and have been used underwater in combination with gated receivers and polarization filters [53, 54]. Hybrid lidar-radar was introduced in 1995 by Mullen et al, when they used 3 GHz modulation of a mode-locked Nd:YAG pulsed laser to separate the backscatter from the target return [1]. Following this demonstration of the potential for frequency-domain separation, a litany of high frequency CW ranging sources were developed. The simplest is a single-tone transmitter as used by Mullen's group, which can achieve <5 -cm resolution out to 7 total attenuation lengths [35]. Pulsed lasers were modulated at high frequency by Pellen and his colleagues, to provide backscatter rejection and <10 -cm resolution to about 7 total attenuation lengths [13, 37]. Innovations for further suppression of the backscatter in ranging and detection include spatial filtering, in which the homogeneity of the water environment and movement of a vehicle are leveraged to drastically re-

duce backscatter by means of a spatial delay-line canceller [31]. To address the problem of short unambiguous range when operating at high frequencies, CW dual-tone approaches have used sequential transmission of two closely spaced frequencies. Frequency-Modulated CW (FMCW) uses wide bandwidth to achieve high resolution ranging with long unambiguous ranges, while Frequency Domain Reflectometry (FDR) offers high resolution, long unambiguous range, and a full reconstruction of the various reflectors encountered [32].

Among these systems that perform ranging, the most successful have been those with high frequency modulation, and of those, several meet the specifications outlined above. For example, the modulated pulse (MP) lasers [14, 37] achieve high powers in the pulse, and high frequency/wide bandwidth in the modulation. When used with pseudo-random (PRN) modulation, it is also essentially unambiguous. Similarly, FMCW and FDR sources deliver wide bandwidth and high frequencies at moderate CW powers [32]. In both cases, there is a tradeoff between repetition rate and resolution: for FMCW, a slower repetition rate makes the frequency detection harder at the output; for MP, as the repetition rate increases, the number of bits per pulse decreases, and the temporal resolution of its autocorrelation is degraded. Thus FMCW trades unambiguous range for resolution, while MP trades dwell time for resolution. Both sources remain strong choices and meet the desired specifications, but would be improved upon by a non-repeating CW source that did not have to make tradeoffs to maximize resolution.

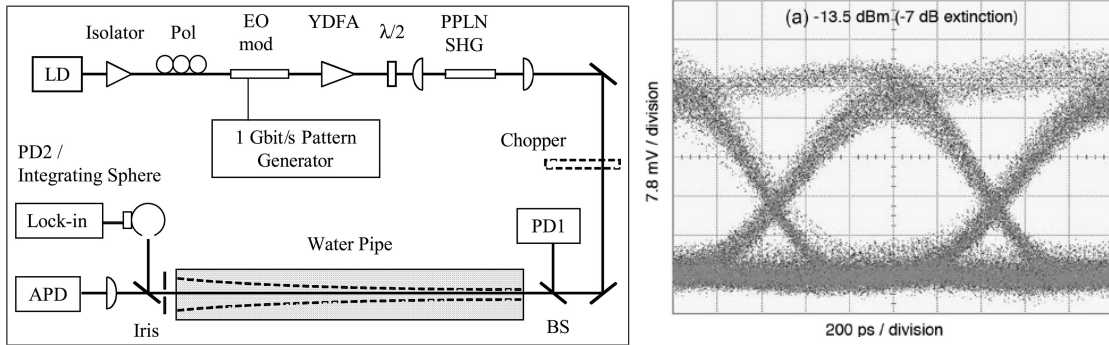
2.2.1.3 Water-based Imaging

Water-based imaging systems use lasers for significantly extended imaging range versus traditional systems [9, 41]. However, with the use of collimated lasers comes the requirement for scanning, and thus the dwell time per pixel is a concern. Imaging systems can be two-dimensional (i.e. a contrast or false-color plot) or three-dimensional (i.e. a range map with each pixel's intensity overlaid). The first Navy-sponsored underwater optical work, at Diamond Island in the 1960s, focused on getting long-range contrast images by scanning pulsed Nd:YAG lasers [2]. Significant work continued through the 1970s, especially at the Scripps Institute of

Oceanography and the Naval Undersea Center, both in San Diego [8] (both facilities remain active in underwater optical R+D today). Pulsed and CW argon gas lasers appeared early on, in conjunction with complex gating, spatial blocking, and polarization schemes to reduce the backscatter [39, 53]. Using fan-shaped beams, some systems scanned full lines of laser light rather than single dots; this practice required more signal processing to reconstruct the image but reduced scanning requirements [55]. Significant performance improvement in 2D imaging was realized using a Laser Line Scanner (LLS) approach, in which the transmitter and the receiver are synchronously scanned across the scene [56]. (This approach has been shown to offer optimal, i.e. diffraction-limited, performance.) Since the introduction of HLR, modulated imaging systems have been developed, including the Time Varying Intensity (TVI) system used by Mullen’s group at NASC Patuxent River using ≤ 200 MHz modulation [57]. Alternatives include a host of pulsed LLS systems that provide 3D mapping using time-of-flight, including a novel receiver-array approach that uses triangulation to garner sub-millimeter range resolution [36]. While these systems boast good performance to 6-7 attenuation lengths, there is a strong emphasis on improvement by signal processing [58], and all transmitters fall into the familiar slow-pulsed time of flight or single-tone-modulated CW categories. Thus none of them meet our transmitter specifications, since they do not provide for backscatter removal (in the pulsed case) or unambiguous range (in the CW case).

2.2.1.4 Water-based Communications

The viability of underwater optical communications has emerged much more recently than the imaging or ranging applications. Where communications was once thought of as a long-range, low-bandwidth application for which acoustic transmission was well-suited, the advent of autonomous underwater vehicles (AUV) has made immediate the idea of short-range, high-speed communications — for example, as a point-to-point download-and-sync operation from sensor AUV to controller ship. A few early studies discussed the feasibility and the scattering mathematics of underwater links, and proposed applications such as submarine-to-satellite communications [59–61], including a few demonstrated field tests [62], but the last five



LD: Laser diode; Pol: polarization controller; EO mod: Electro-optic modulator; YDFA: Ytterbium-doped fiber amplifier; $\lambda/2$: Half-wave plate; PPLN SHG: Nonlinear crystal; [A]PD: [Avalanche] Photodetector

Figure 2.7: Water-to-water 1 GHz communication using a frequency-doubled fiber laser (Images [4])

years have seen a boom in active work [4, 22, 25, 27, 28, 40, 63–68]. Both diffuse LEDs and collimated laser diodes have been considered as sources; the best argument for lasers is their long range and inherent security, while LEDs are much cheaper and are widely available at all wavelengths. For our applications, the superior range of lasers are necessary. Laser communications systems include modulated CW transmitters [27, 40], as well as pulsed sources encoded by pulse-position modulation (PPM) [60, 69]. Recent comparisons of modulation techniques in the underwater environment have suggested that PPM or on-off-keying (OOK) with Reed-Solomon encoding can produce efficient, reliable links [40, 70]; for the most part, the implemented schemes use direct modulation of diodes. One interesting source introduced by Spawar San Diego was used for 1 GHz communication; they used an intensity-modulated 1064 nm fiber-coupled diode [4]. This signal was amplified by ytterbium-doped fiber amplifiers (YDFAs) and sent through a second-harmonic generating (SHG) crystal to produce 532 nm green light. The resultant 7 mW of green was lower than our desired specifications, but was still sufficient to effectively send data at >8 attenuation lengths. This transmitter is notable because it produced wide bandwidth, at high frequencies, in a non-repeating CW code with no ambiguous range. Its power was not high, but neither was it limited by the technology used; while the application did not require higher power, the power could have been easily boosted by another amplifier. Thus while communications is not our imme-

Table 2.2: Comparison of Laser Technologies

Type	Avg. Power	Frequency	Comments
Solid-state	10^2 W	200 MHz	Nd:YAG $\eta < 10\%$ [6], EM
Gas ion	10^2 W	200 MHz	Argon $\eta < 1\%$ [6], EM
Dye	10^1 W	200 MHz	Rhodamine 6G $\eta < 1\%$ [6], EM
Diode	10^{-1} W	350 MHz	InGaN $\eta < 20\%$ [71]
Fiber Laser	10^2 W	> 10 GHz	Yb ³⁺ SHG $\eta < 20\%$ [72, 73]

EM: External modulator; η : Wall-plug efficiency; SHG: Second-harmonic generation (532 nm)

diate application, the technology used by the Spawar team meets our specifications and may be useful.

2.2.2 Laser Types

Blue-green lasers are valuable for many applications, but there are limited options for generating blue-green light. Traditional gas, dye, and solid-state bulk lasers have long been used to generate high powers, but they are large and require high currents. Small and efficient semiconductor diodes are preferable, but they are only recently commercially available, and their powers are still low. Variant methods of getting blue or green lasing include diode-pumped solid-state (DPSS) and “synthetic green” (or, “blue”) schemes, both of which use an infrared diode to excite blue-green lasing.

Solid-state, dye, and gas lasers are the three oldest laser families. Solid-state bulk lasers are based on pumping energy into crystal or glass that has been doped with transition metal or rare-earth ions. Similarly, dye lasers flash-pump liquid organic dyes to stimulate lasing. Gas lasers rely on high electrical currents to excite ionized gases. Whatever the means, the electrons are excited to high energy states, from which they can emit photons and contribute to lasing. Flash bulbs and other bulk lasers have been common for pump lights to stimulate excitation, but semiconductor diode lasers are now often used, thanks to their compactness and low heat signatures. Since electrons orbit in discrete energy bands, their emission also happens at discrete frequencies, referred to as transition levels. These levels correspond to photon wavelength, and thus dictate what laser wavelengths are available. Gaseous ion transition levels in the blue and green include argon (488, 514 nm), copper

vapor (510 nm), and helium-cadmium (442 nm), all of which require large pump powers, careful handling, and in the case of argon, active cooling to deal with the heat. There are no direct solid-state blue-green transitions, but neodymium-doped YAG crystal lasers (Nd:YAG)) is commonly doubled from 1064 nm to 532 nm. Dye lasers are tunable over wide ranges, and so there are several options for blue and green emission. The common problems with these three traditional laser families are low efficiency, large footprint, high pump power requirements, and most critically, limited options for RF modulation. These lasers can emit CW light, or they can be mode-locked to generate pulse trains. If CW light is sourced, an external bulk modulator must be used; such modulators are commercially available only to ~ 200 MHz and require very high voltage RF sources. Using mode-locked pulse trains has more potential, but as the repetition rate is governed by the physical dimensions of the cavity, there is little opportunity for tailoring the modulation in response to channel conditions.

Semiconductor laser diodes are much newer than the free-space solid-state, dye, and gas lasers. They have quickly opened up new applications due to their small size, power efficiency, and wide emission bandwidths. Indium gallium nitride (InGaN) is the primary material with a direct bandgap corresponding to the blue-green range, and laser diodes using InGaN are commercially available at virtually all wavelengths of interest from 405 to 530 nm. Here the issues are power and modulation frequency. Powers are limited to ≤ 200 mW in the blue, and even lower in the green (see Figure 2.8) [74–76]. Meanwhile, modulation depth begins to fall off around 200 MHz, with 350 MHz a typical 3 dB point [74]. At higher frequencies, the output signal is mostly DC light; thus in power-limited or dynamic-range-limited applications, the system will not be able to operate at high frequencies or wide bandwidths. Diodes are an active field of research and development, and improvements are continuous; still, currently available technology severely limits the modulation schemes that can be employed for underwater lidar.

Fiber lasers use rare-earth-doped fibers as a gain medium. They can include free-space components, but modern lasers are typically all-fiber, using fiber-coupled semiconductor diode lasers as the pump source, doped fiber as the gain medium, and

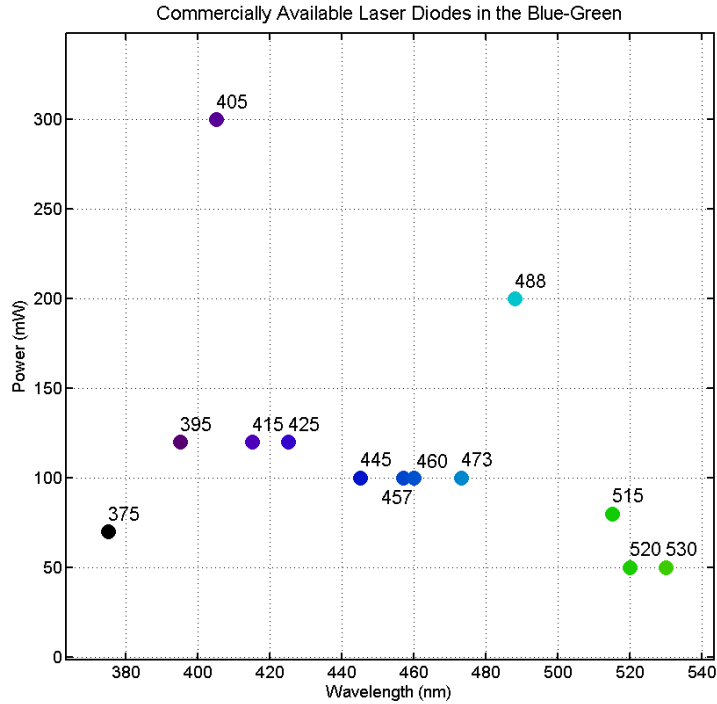


Figure 2.8: Commercially Available Laser Diodes

passive fiber components for the resonator cavity. The dopants are distributed homogeneously throughout the glass host, just as dopant ions are deposited in crystals in solid-state lasers. Typical dopants include neodymium, thulium, praseodymium, ytterbium, and erbium, but the latter two are by far the most common. Erbium-doped fiber lasers (EDFLs) and amplifiers (EDFAs) operate at 1550 nm, the wavelength used for telecommunications and for eye-safe free-space lidar. Ytterbium-doped fiber lasers (YDFLs) and amplifiers (YDFAs) at 1064 nm have been developed more recently, and are common in high-power-density industrial applications like cutting, marking, and welding [72, 77, 78]. Ytterbium-doped fibers (YDFs) are particularly efficient absorbers of pump light, so very high pump powers can be used with good efficiency and relatively short fibers. The short fibers also allow for high-power pulse generation and amplification (long fibers can lead to nonlinearities with high peak powers), and so YDFLs are often used for picosecond and even femtosecond pulsing [77, 79]. Cladding-pumped YDFLs and YDFAs allow high-power, wide beam multi-mode pump lasers to be used, and YDF systems can now operate in the kW

Table 2.3: Comparison of Wideband Modulation Waveforms

Scheme	Pros	Cons
Modulated Pulse	$\uparrow d_{max}$, $\uparrow B$, $\uparrow P_{peak}$	Complex, \downarrow PSLR
FMCW	$\uparrow d_{max}$, $\uparrow B$, $\downarrow Z_{cpu}$	SLM source
FDR	$\uparrow d_{max}$, $\uparrow B$, ≥ 1 target	SLM source, $\uparrow t_{dwell}$, $\uparrow Z_{cpu}$
Noise radar	$\uparrow d_{max}$, $\uparrow B$, \uparrow PSLR, no EOM	$B > B_{specified}$

P_{peak} : Peak power; d_{max} : Unambiguous range; B: Bandwidth; PSLR: Peak-to-sidelobe ratio; Z_{cpu} : Processing load; EOM: Electro-optic modulator; SLM: Single-longitudinal mode

average powers, or near-MW peak powers in the case of pulsed systems [80]. Fiber lasers have the additional advantages of being compact and rugged, with relatively little concern for heat buildup or temperature dependence. They can also be modulated at GHz frequencies thanks to the small capacitance of the 10 μm crystal used in the modulator; 40 Gbps interferometers are routinely used in binary telecommunications [81]. While 1064 nm light is not appropriate for underwater use, frequency doubling can be used, just as in Nd:YAG systems, to obtain 532 nm light using fiber lasers. Thus high powers, small form factor, and wide bandwidth at high frequencies should all be possible in a fiber-laser based system.

Of the laser technologies discussed, the frequency-doubled fiber laser stands out for underwater lidar. Free-space lasers are large, inefficient, and cannot be modulated at high enough frequencies to suppress backscatter. Diodes are low power, and have problems with modulation depth at high frequency. Fiber lasers, on the other hand, can be high-power and can be modulated at very high frequencies. Thus we have elected to use a ytterbium-doped fiber laser as the basis for the new chaotic transmitter.

2.2.3 Modulation Waveforms

There are many useful waveforms for accurate ranging, where the primary selection criteria are unambiguous range and resolution. Having decided on a fiber-laser based design, we can use CW or pulsed, and we can use a modulator to impose almost any conceivable waveform for transmission. We have previously noted that of the myriad modulation waveforms previously used and proposed, modulated pulses (MP), frequency-modulated CW (FMCW), and frequency-domain reflectom-

etry (FDR) meet all desired specifications for our transmitter (Section 2.2.1.3). Each does ultimately have a repetition-rate vs. unambiguous range tradeoff, but for short ranges (≤ 50 m) this is not a primary concern. However, we can now suggest a modulation scheme that has not been used before in underwater lidar, but has been successfully demonstrated for a variety of ground/wall-penetrating radar applications, as well as optical reflectometry and free-space lidar. “Noise radar” uses a wideband, non-repeating noise-like signal to probe a target; the correlation of the return signal with the transmitted signal then reveals the round-trip distance to the target [82–84]. This technique can use a true wideband noise generator, or it can use chaotic wideband signals. Advantages are relatively simple processing, a completely unambiguous range, and high resolution.

Since FMCW, FDR, MP, and noise radar can all be implemented in fiber lasers at very high bandwidths, the channel transmission constraints — i.e. the backscatter cutoff frequency and the maximum frequency resolvable by the receiver — will likely determine the usable bandwidth available for our system. Thus, choosing a modulation scheme becomes a question of unambiguous range, and of complexity and cost of implementation. A comparison is presented in Table 2.3. Since the noise radar is non-repeating, it has a slight advantage in unambiguous range, but it is in implementation that differentiations can be made. FMCW and FDR will both require a CW fiber laser source, preferably single-frequency, that can then be modulated by an interferometer and amplified (1064 nm CW diodes are available only at low powers, so another amplifier stage may be necessary). An FMCW receiver is fairly simple, requiring very little processing; FDR is much more complicated, and it is difficult to implement in real-time. Moreover, FDR requires long dwell times for full discrete frequency sweeps, and so it may not be appropriate for fast-scanning imaging work. Modulated pulses require a mode-locked fiber laser source, modulated with an interferometer before amplification and transmission. MP systems also require synchronized management of stored energy in the fiber, which is not trivial, and which can easily lead to destroyed components and unintended pulses if stray stimuli find the gain medium when energy is built up. They also have high sidelobes in the correlation function: the correlation of the macropulse is a broad triangle,

superimposed with the sinusoidally periodic correlation of the high-frequency bits. Detection is thus much harder than for a thumbtack autocorrelation, as produced by the noise radar.

Noise radar is commonly implemented by injecting optical feedback into an optical semiconductor diode. Interestingly, a fiber ring laser can also be used to generate wideband chaos, because ring lasers are essentially optical feedback loops. Chaotic (deterministically non-repeating) mode interactions are generated within the resonator ring, and the resulting signal is both wideband and noise-like [16]. Thus fiber ring lasers can be used as seeds for noise radar systems without any interferometer or RF signal generator to perform the modulation. Additionally, synchronized chaotic lidar systems have been shown to deliver significant performance gains over traditional noise radar, so there is the possibility of leveraging the nonlinear dynamics of the chaotic ring laser for further improvement [19].

Thus there are some advantages in implementation for the noise radar, both on the transmitter side, where no modulator is necessary, and on the receiver side, where the unambiguous sharp peak can be easily detected. Meanwhile using the noise radar avoids potential pitfalls such as long dwell time and slow processing (FDR), dangerous energy build-up and poor peak-to-sidelobe ratio (MP), and the difficulty of building a true single-frequency seed laser with reasonable power (FMCW). Taking these considerations into account, we decided to implement the noise radar approach using a chaotic ytterbium-doped fiber laser as the source.

2.3 Proposed Transmitter Solution

Having selected a fiber laser as the appropriate technology, and recognizing the unique advantages of the a noise-like waveform for correlation-based ranging, we propose to use a fiber ring laser to generate a wideband noiselike signal. Thanks to their optical feedback, such lasers are chaotic with wide bandwidth, with signals that span the high frequencies that will suppress backscatter. We note that by introducing a long passive fiber into the cavity, the resonant frequency of the cavity can be made small, and thus the lasing longitudinal modes will be closely spaced — where the limit of zero spacing corresponds to the flat continuous spectrum

Table 2.4: Proposed Transmitter Specifications

Parameter	Desired	Proposed	Comments
Power	10 W	1 W	Multi-watt NIR; allows 16 att. lengths
Frequency	500 MHz	DC—>1 GHz	Quasi-continuous frequency spectrum
Bandwidth	800 MHz	>1 GHz	Receiver-limited resolution <13cm
Dwell Time	10 μ s	TOF	SNR increases with integration
Rep. Rate	50 MHz	Arbitrary	Inverse of dwell time

NIR: Near-infrared 1064 nm; TOF: Time of flight to target and back; SNR: Signal-to-noise ratio of output signal

characteristic of perfect white noise. Thus a wideband, noise-like chaotic signal across the frequencies of interest can be generated by using a well-known laser design, with a small modification to the cavity length. (Following the variety of terminology in the literature, this laser will be referred to as the “seed laser”, the “master oscillator”, or the “signal source”.)

The seed laser will use ytterbium-doped fiber for operation at 1064 nm, and frequency doubling by an SHG crystal will generate the green signal for use underwater. Since the single-pass efficiency of the frequency doubler is expected to be low, the infrared power must be high into the doubler. The seed laser is not expected to generate nearly enough power for conversion to the specified green power levels, so ytterbium-doped fiber amplifiers will be used. The detailed design of this laser, the amplifiers, and the frequency doubler are the topic of the next chapter.

Briefly comparing the proposed transmitter with the outlined specifications, it is seen that the frequency-doubled fiber ring laser technology is appropriate for our application (see Table 2.4).

CHAPTER 3

THEORY AND SIMULATION

3.1 Chaotic Fiber Laser Transmitter Detailed Design

The chaotic fiber laser transmitter is designed to source moderate powers in the blue-green wavelengths, with wide instantaneous bandwidth at high frequency. The transmitter starts with a fiber ring laser operating at 1064 nm near-infrared (NIR), which is frequency doubled to 532 nm green light. This doubling is performed by a second-harmonic generating (SHG) crystal, and requires high NIR powers for good efficiency. Thus a fiber amplifier chain is required to boost the seed signal to sufficiently high powers prior to frequency doubling.

The fiber ring laser, the fiber amplifiers, and the frequency doubler are shown in Figure 3.1, and will be discussed in turn.

3.1.1 Fiber Ring Laser

3.1.1.1 Theory of Fiber Lasers

Lasers are based on electron energy levels, and the propensity of electrons to emit light photons when they relax from a high level to a low level. In fiber lasers, rare-earth ions are used to absorb light at one wavelength, which excites the ions' electrons to an upper energy band, and emit light at a second (longer) wavelength, as the electrons relax to a lower energy band. (Conceptually, a two-level model is easy to understand; in actuality rare-earth dopants are usually three- or four-level, as discussed below.) The energy bands for erbium and ytterbium are shown

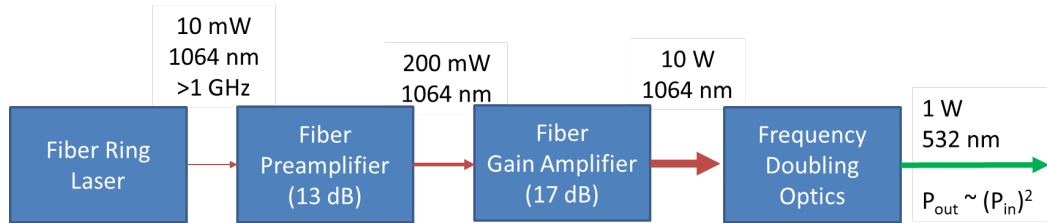


Figure 3.1: Chaotic Transmitter Block Diagram

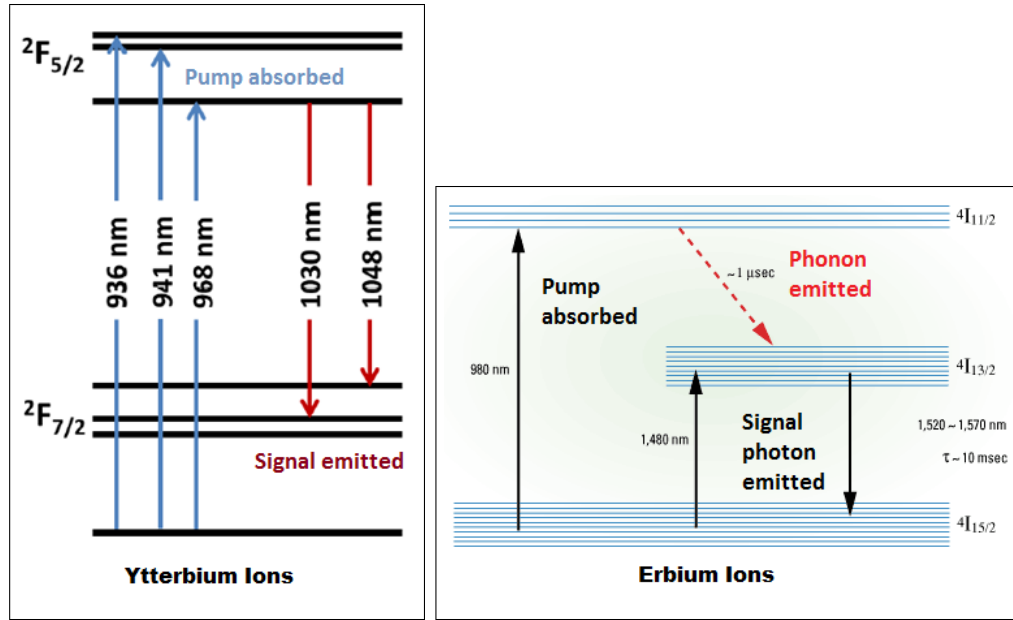
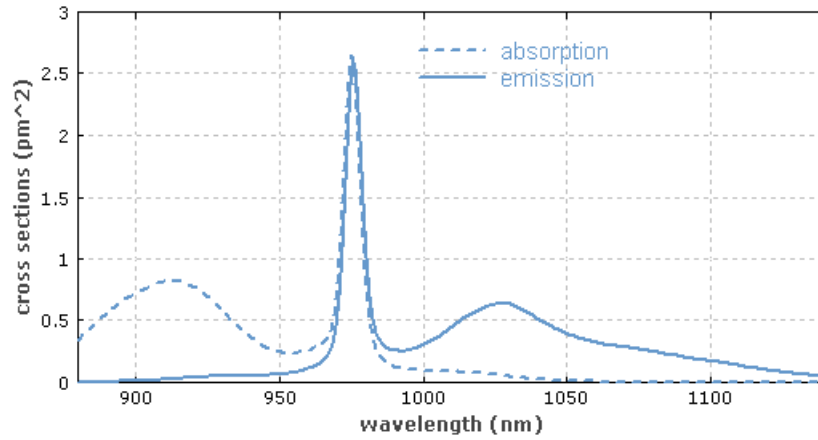


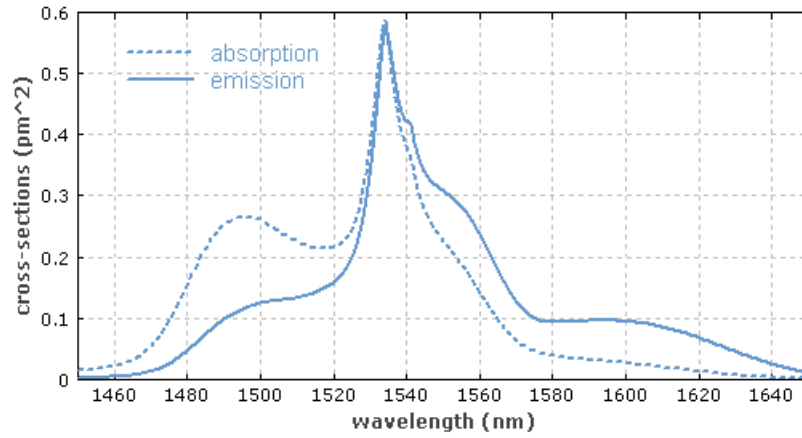
Figure 3.2: Rare-Earth Dopant Energy Levels

for emission at 1550 nm and 1064 nm, respectively, when pumped by a 980 nm light source (Figure 3.2). The most interesting property of these transitions is that emission can be either spontaneous or stimulated — that is, the relaxation may occur “naturally” with no other input, or it may occur when the electron is struck by an incident photon. In the latter case, stimulated emission occurs, and the electron emits two photons, each identical in energy and velocity to the stimulating photon. In this way, a photon (or photon stream) can be repeatedly doubled when it passes through excited electrons. This stimulated emission gain is the phenomenon leveraged to create lasers. A pump excites the electrons, a resonator forces repeated trips by the light through the excited medium, and the resultant stimulated emission generates a large beam of photons that are monochromatic (identical in wavelength) and collimated (identical in velocity).

Several important observations should be made from the energy level diagrams. First, it is clear that absorption and emission are the driving phenomena of laser systems, and must be well understood and modelled for accurate performance prediction (Figure 3.3 shows the absorption and emission spectra). It is also apparent that ytterbium’s 1064 nm transition is intrinsically more efficient than erbium’s 1550 nm emission, since the energy of the emitted photon is much closer to the pump



Ytterbium-doped fiber absorption and emission spectra



Erbium-doped fiber absorption and emission spectra

Figure 3.3: Rare-Earth Dopant Absorption and Emission Spectra

energy than is the case with the erbium. Note that the energy E of a photon is directly related to the frequency, i.e. inversely related to the wavelength, by

$$E = h\nu = hc/\lambda \quad (3.1)$$

where h is Planck's constant, c is the speed of light in the medium, ν is the photon frequency, and λ is the wavelength. Lastly, at these absorption and emission wavelengths, erbium is seen to be a three-level system, where a small phonon (mechanical) decay occurs from $^4I_{15/2}$ to $^4I_{13/2}$ before the major photon relaxation to the $^4I_{11/2}$ ground state. Ytterbium is a four-level system, where the photon relaxation is not to the ground state, but rather to a slightly excited state ($^2F_{7/2}$). It

seems logical that emission to an empty valence band will be made more readily than emission to a full band, so the four-level system has an apparent advantage in emitting to a non-ground-state, which will be nearly empty compared to the ground state. When a full analysis is performed, this indeed turns out to be a significant advantage [85, 86].

By using erbium- and ytterbium-doped fibers, we can design and implement fiber lasers that convert uninteresting pump light into very useful signals, whose wavelength, intensity modulation, polarization, and power can all be precisely controlled. Fiber lasers differ from other laser types in several primary ways. Firstly, the rare-earth doped gain media have very wide bandwidths; that is, they may spontaneously emit at wavelengths spanning tens and hundreds of nm. Secondly, their resonator cavities are significantly longer than diode, dye, or bulk lasers, and thus the cavity length itself cannot be used to fully control wavelength or intensity modulation profile. Other filtering methods must be used. Lastly, glass fibers are not intrinsically polarization maintaining, and so polarization dispersion is to be expected in the cavity. Thus the output polarization will not be purely linear, even if a linearly polarized pump is used. In our application, this is significant because the frequency doubling crystal operates only on a single polarization of light; the rest passes through unaffected.

3.1.1.2 Ring Lasers as Oscillators

The simplest form of laser is a called a Fabry-Perot laser, in which two reflectors are positioned on either side of a gain medium (Figure 3.4). One of these reflectors allows input of a pump wavelength, but is fully reflective to the desired lasing wavelength. The other reflector is only partially reflective at the lasing wavelength. This ensures several passes of the laser beam through the gain medium, which produces high powers, but it also allows some of the resonating beam to escape out the partially reflective mirror (i.e., the output coupler). A standing wave is generated between the reflectors as the beam bounces back and forth and creates an interference pattern at multiples of the cavity wavelength. Ring lasers are simply a variation of this configuration, in which the beam is guided around a ring, passing

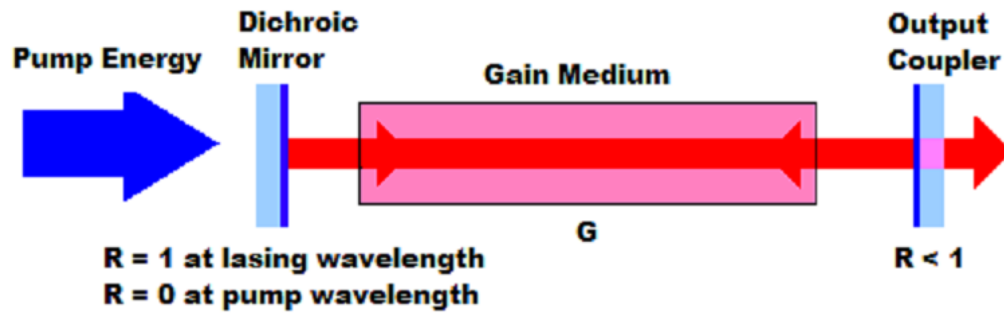
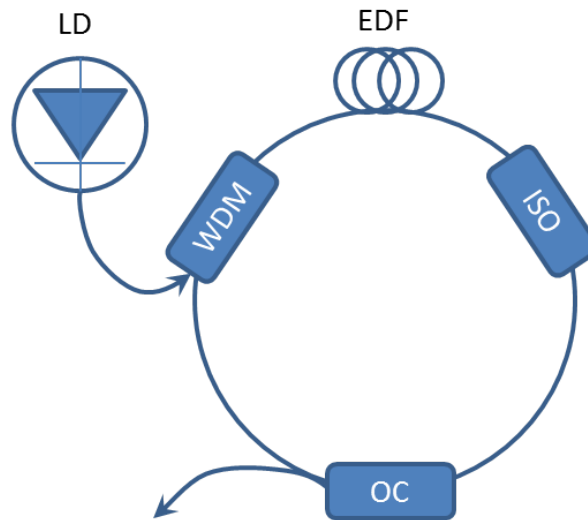


Figure 3.4: Laser Reflector Cavity



LD: Laser diode; WDM: Wavelength-division multiplexer;
EDF: Erbium-doped fiber; ISO: Isolator; OC: Output Coupler

Figure 3.5: Laser Ring Cavity

through the gain medium and the output coupler once per round trip (Figure 3.5). In this way unidirectional travelling wave lasing is obtained, instead of the standing wave; this can avoid such undesirable effects as spatial hole burning in the gain medium and interference between the counter-propagating polarizations.

Ring lasers also exert control over the intensity modulation pattern of the laser, which can be understood most immediately from examining the lasing frequencies. The simplest laser output would be single-frequency, or equivalently single-longitudinal-mode (SLM). In this case, the cavity resonant frequency would be so

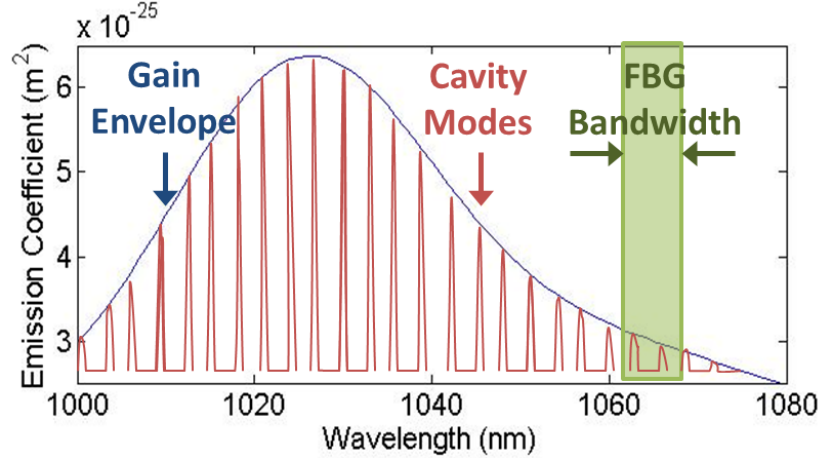


Figure 3.6: Ring Laser Emission Spectrum

high (i.e. the cavity length would be so short) that harmonics of this resonant frequency would fall outside the lasing bandwidth. In the case of bulk lasers with narrow gain bandwidth, this can sometimes be achieved. For example, the HeNe laser has a gain bandwidth of ~ 2 GHz, so a resonant frequency of ≥ 1 GHz (ring cavity length ≤ 20 cm) would result in a single mode standing at the peak of gain, and two other modes falling outside the edge of the bandwidth. In most cases, these modes would not lase since their gain would be small relative to the fundamental mode, and so single-mode operation would be achieved. Fiber lasers are quite at the opposite extreme, as shown in Figure 3.6: their gain bandwidths are many THz, and the resonant frequencies are rarely higher than 50 MHz (4 m long ring), and usually much lower. Since 0.1-1 nm gratings are usually incorporated to control the lasing wavelength, we can more realistically say lasing may occur over 10s-100s of GHz. Even so, a 50 GHz grating combined with a 20 MHz cavity allows lasing of 2500 modes. The interaction of these modes, and particularly the phase relation between them, defines the intensity modulation of the laser.

3.1.1.3 Temporal Output Signal

SLM lasers are true CW light sources. While they can be achieved in fiber lasers, they have no instantaneous bandwidth, and since our application is wideband, we do not seek an SLM solution (though in fact a widely tunable SLM source might be of great interest; see Chapter 5 for discussion of future work directions).

Multi-mode solutions can take one of several forms, depending on the phase relationship between the modes. As shown in Figure 3.7, if the modes are in phase, they will all add up constructively at a single instant in the round-trip time, and a short high power pulse will result. Phase-locking (or, mode-locking) can be readily achieved in a variety of active or passive ways, and since high instantaneous powers are desirable in many applications, mode-locked lasers are common (including in underwater lidar; see Chapter 2). Mode-locked fiber lasers are particularly useful for ultrashort pulses, since their wide frequency bandwidth makes for a very narrow impulse in the time domain. If the modes are not intentionally phase-locked, self-pulsed modulation (SPM) may still create a partially phase-locked scenario, in which periodic modulation occurs on the cavity round trip interval, usually with some pulsing behavior overlaid with less recognizable behavior. However, under some conditions the self-pulsed behavior breaks down, and the system enters a deterministically non-linear chaotic regime. In this chaotic regime, the mode phases are no longer aligned, and the system is both wideband in the frequency domain and noiselike in the time domain [85].

The mode spacing may be manipulated by changing the cavity length. A longer cavity will have a shorter resonant frequency by $f_r = c/L$ where f_r is the resonant frequency and L is the cavity length; the mode spacing (or, “free spectral range” (FSR)) is the same as the resonant frequency since each harmonic will lase. Thus by simply increasing the cavity length, the mode spacing will be decreased. When operating in the chaotic regime (where phase is essentially a non-repeating random variable), the limit of zero mode spacing would be white noise.

3.1.1.4 Signal Output Relation to Target Applications

Of the multi-mode regimes, the chaotic one is perhaps the most interesting for novel lidar systems. Ultrashort pulses are certainly useful for time-of-flight lidar, but they suffer from minimum and maximum ranges associated with gating and repetition rate (see Chapter 2). They are also difficult and even dangerous to implement, since there is such an energy build-up in the fiber during the off-state of the duty cycle. The peak powers can easily cause non-linear effects in the fiber, can

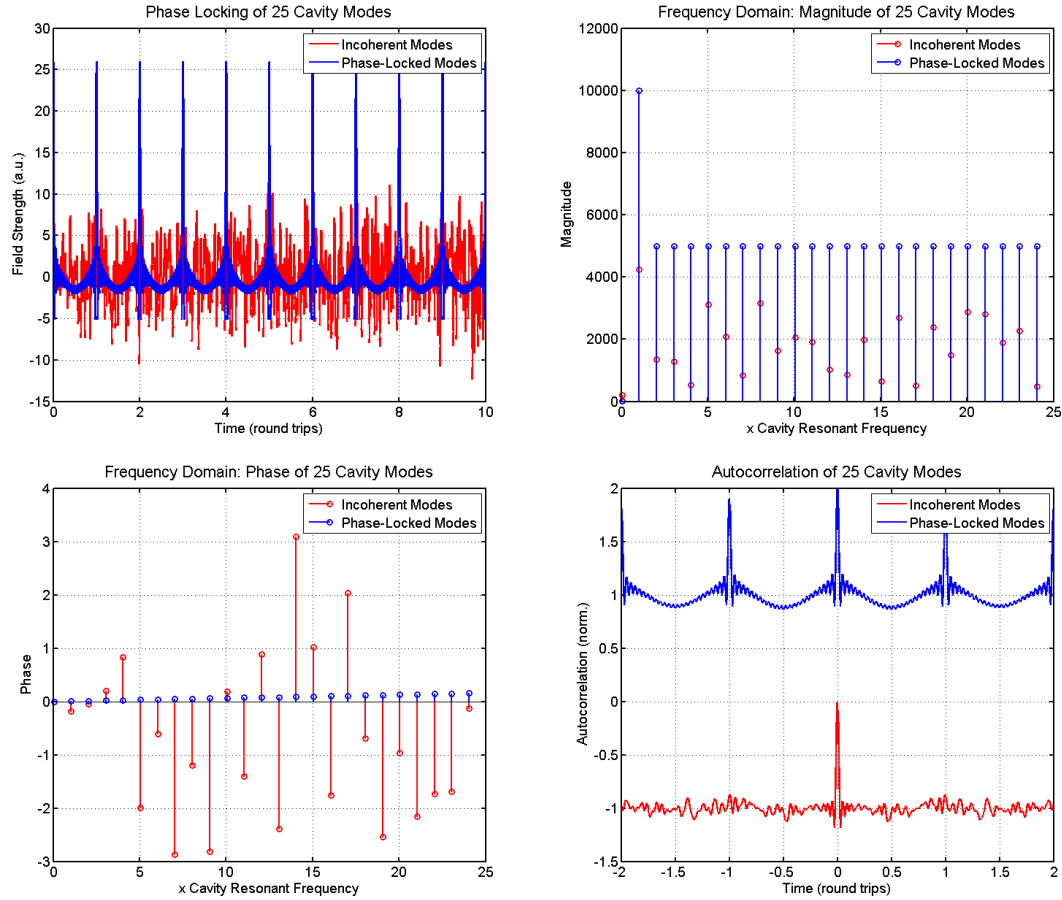


Figure 3.7: Mode Locking by Phase Coherency

burn the fiber and other optical components, and can allow sudden and unwanted high power pulses to propagate if any unintended stimulation appears in the fiber when high energies are stored. SPM operation is less dangerous, since it is in some way a CW scheme, but its maximum unambiguous range is also governed by the cavity round trip time since it is periodic. Moreover it does not lend itself to high resolution ranging since its autocorrelation is broad. The chaotic regime, meanwhile, allows for completely unambiguous ranging since it is non-repeating; it is broadly CW with little variation in energy stored in the fiber; and like true white noise, its autocorrelation is a sharp thumbtack function. Figure 3.8 shows how by increasing the number of modes, the autocorrelation function can be improved; this explains why chaotic multi-mode lasers can have such favorable autocorrelations. Thus unambiguous and high-resolution ranging can be achieved with a simple fiber ring laser

and readily available components by operating the laser in a chaotic regime.

Specific comparison may be made between the desired specifications and the performance facilitated by the chaotic seed signal. The bandwidth of the chaotic signal will effectively be the width of the grating used; this is many GHz and so is much wider than the specification. There is certainly operation at high frequencies, since there is operation at all nearly all frequencies. The range resolution will be inversely related to the bandwidth, and as the chaotic signal becomes noise-like, the peak width will be a single sample and thus the system resolution is receiver-limited. Thus a 1 GHz receiver will give 13 cm resolution, 2 GHz will give 7 cm, and so on. The signal-to-noise ratio of the output will be governed by the mode spacing (smaller spacing drives higher peak-to-sidelobe ratio), the flatness of the spectrum, and by the integration time if the dwell is over multiple time-of-flights (this is not intrinsically necessary). Thus by operating a long-cavity fiber ring laser in the chaotic regime, a correlation-based ranging system can be constructed with receiver-limited single-sample resolution, a high peak-to-sidelobe ratio, and operation at high frequencies where the backscatter is unlikely to corrupt the modulated signal. Such a scheme is discussed further in Section 3.3.1.

A second proposed application of this system is to characterize the operating channel's frequency response. The chaotic signal would contain a quasi-continuous frequency spectrum, and so by measuring the received signal and comparing it to the known transmitted signal, the instantaneous channel magnitude response can be known for the entire operating frequency range. As the frequency spacing is reduced, this response function is mapped with increasingly small frequency step size, and so the long-cavity chaotic transmitter is ideal for the application. Knowledge of the channel response would be useful for predicting which frequencies were likely to see high attenuation or corruption by scattering in a given environment. Similarly, a backscatter transfer function could be deduced by transmitting this wideband multi-mode spectrum, and observing the modulation depth of the backscattered light at each frequency. A tunable transmitter would then respond to these channel conditions to improve performance. Such knowledge would supplant dependence on models and estimations that cannot possibly account for all the various and quickly

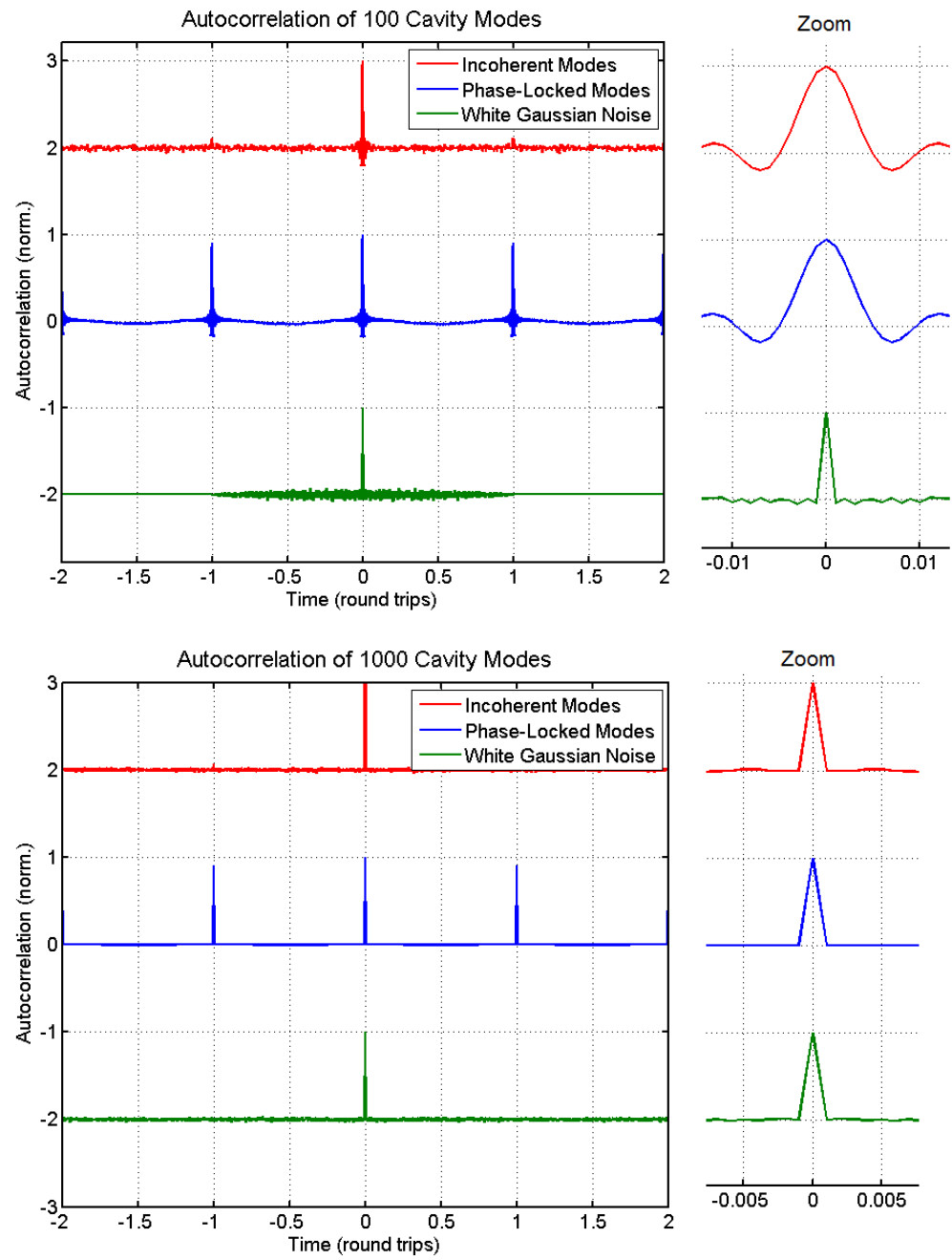


Figure 3.8: Autocorrelation of Various Wideband Signals

changing channel conditions a system might encounter in real-world operation. See Section 3.3.2 for a novel method for channel identification with the chaotic laser.

3.1.2 Fiber Amplifiers

3.1.2.1 Theory of Fiber Amplifiers

Like fiber lasers, fiber amplifiers rely on a higher-energy pump source to excite the dopant ions in the active fiber. A low-power signal can then be coupled into the active fiber; the signal is amplified by stimulated emission. The gain due to stimulated emission is determined by the excitation ratio of the ions. When the signal is small, the excitation ratio remains nearly constant through the fiber; this is the small-signal gain case. As the signal grows large, most of the excited ions in the fiber are stimulated and relax, and there is then no further amplification. Thus any fiber amplifier has a maximum achievable gain, governed by the pump power absorbed, the fiber length, and the input signal size. Numerical simulation can predict the performance of fiber amplifiers for various parameter values.

3.1.2.2 Common Fiber Amplifier Designs

Standard amplifier configurations include forward-pumped, backward-pumped, and bidirectionally-pumped arrangements, as shown in Figure 3.9. In forward-pumped amplifiers, the pump power and the signal power propagate together; the excitation is thus concentrated in the initial segment of the active fiber. Backward-pumped amplifiers have the pump at the signal output end of the active fiber, and the signal is amplified at the end of the fiber. Bidirectional pumping creates excitation at both ends of the fiber, which can lead to more uniform gain distribution. While all three amplifier configurations have been successfully used, each has pros and cons that should be considered for a given design.

In forward-pumped amplifiers, the pump and signal are coupled in to the active fiber together. The insertion loss associated with the wavelength-division multiplexer (WDM) thus reduces the input signal before the amplifier, but does not affect the signal power leaving the fiber. This may be an advantage when the signal power is sufficiently large, but the loss may reduce a small signal to the point where it will not dominate the amplified spontaneous emission (ASE) and the output will

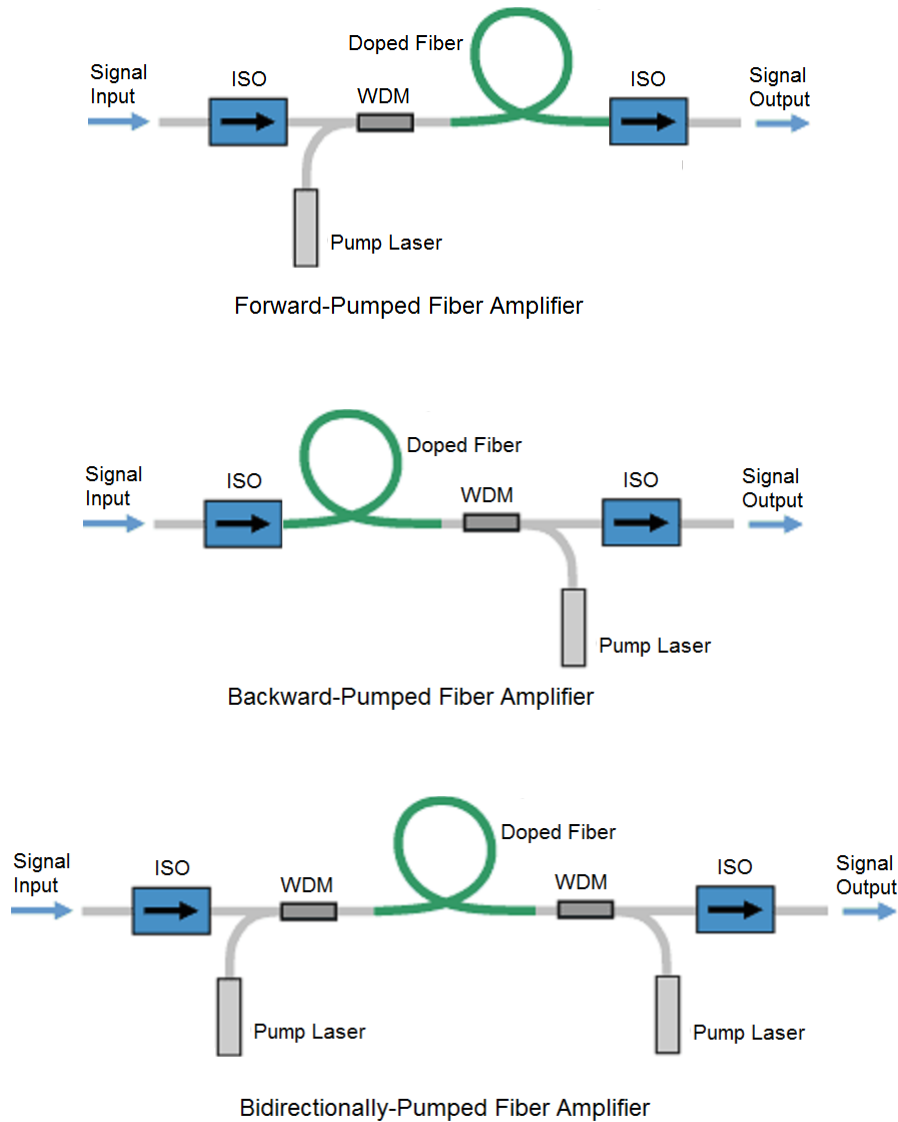


Figure 3.9: Common Fiber Amplifier Configurations

then be corrupted. Additionally, if the fiber length is too long, reabsorption may reduce the efficiency. Backward-pumped amplifiers may be more appropriate for very low powers because they maximize the signal into the amplifier, but they add insertion loss at the output, which may be critical. Backward-pumping can also reduce the ASE in high-power amplifiers. Bidirectional amplifiers may be an efficient way to use multiple pump lasers, and can combine the best of the forward and backward pumping by reducing ASE and reabsorption. However, there is insertion loss at the input and the output.

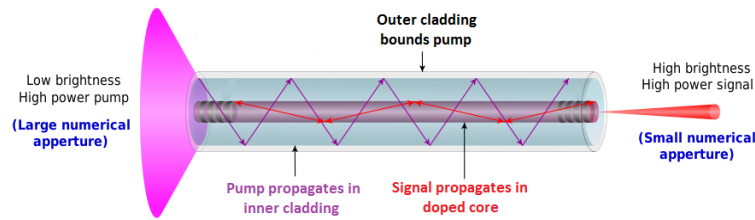


Figure 3.10: Double-clad Fiber

In all cases, isolators are usually used immediately after the seed, and at the pump outputs, and between amplifier stages, to prevent ASE and other spurious signals from being amplified backward, potentially damaging "uphill" stages. ASE and backreflections from fiber tips, splices, and mode mismatches can easily become troublesome in high gain amplifiers, and so care must be taken to protect components. Pumps are often protected as well.

Cladding-pumped fiber amplifiers have become a widely used and very effective way to generate high output powers from fiber amplifiers (see Figure 3.10). Cladding-pumped amplifiers can use much higher pump powers than core-pumped amplifiers, since they launch the pump light into multimode (large diameter, high numerical aperture) fibers. The pump diode beam can be relatively wide-angle when coupled into the fiber, and this makes it much easier to use high-power pump diodes. Compared with core-pumped single-mode (small diameter, low numerical aperture) fibers, the coupled pump powers can be several orders of magnitude higher, and average output powers of 100's and even 1000's of watts become achievable. Double-clad fibers are used in cladding-pumped amplifiers; these fibers have a core for signal propagation, an inner cladding that the pump travels down, and an outer cladding to contain the pump beam. As the pump light reflects back and forth within the inner cladding, it overlaps the core, which is doped with ions. These ions are excited by the pump light and are then stimulated by the signal, which is amplified as it moves along the core. The claddings are not doped; they exist only to contain the high-power pump beams. Cladding-pumped amplifiers can be modelled just as core-pumped amplifiers, with the addition of an overlap term indicating how much of the pump power is hitting the doped core at any given time.

3.1.2.3 Amplified Spontaneous Emission and Amplifier Performance Limits

Spontaneous emission is undesirable in an amplifier since it carries no information; it is analogous to noise in an electrical system. ASE occurs when there are more excited electrons than the signal can stimulate, and spontaneous decay occurs before stimulated emission can take place. Thus ASE is minimized by low pump powers and high signal powers. (This may explain why backward pumping is effective in reducing ASE: the pump power absorbed is lower at the signal input end of the active fiber, and higher only at the output end, after the signal has grown.) In small-signal amplifiers, ASE is typically not a concern at gains below 20 dB, but for higher gains and for high power amplifiers, ASE may well limit performance, and calculations or modeling should be performed to verify the design.

When ASE does not limit performance, fiber amplifiers can be very efficient at converting the high-energy pump light into lower-energy signal light with wavelength and modulation of interest. Clearly, the hard limit on energy conversion efficiency is the ratio of signal photon energy to pump photon energy, or,

$$\eta \leq h\nu_s/h\nu_p = \lambda_p/\lambda_s \quad (3.2)$$

Thus the wavelength ratio, known as the quantum defect, is the ultimate amplifier performance limiter. Sources of inefficiency that prevent attaining to the quantum defect include insertion loss, mode mismatches, splice losses, and reflections. Insertion loss is the unavoidable loss of power through a component; these tend to be $\leq 10\%$ for common components at 1550 nm, but can be frustratingly high (often 30-40%) for 1064 nm components. The mismatches between dissimilar fibers' effective mode field diameters (MFD) often prevent 100% coupling between the passive and active fibers: the loss L is given by

$$4/(r + \frac{1}{r})^2 \quad (3.3)$$

where $r = \frac{MFD_1}{MFD_2}$. This mode mismatch can lead to low pump or signal coupling into the amplifier. A final source of inefficiency in fiber amplifiers is reabsorption.

If the active fiber is so long that all the pump power is absorbed before the end of the fiber, the last part of the fiber will not see much excitation. Thus there will be no stimulated emission or amplification of the signal, and there will be absorption of the signal instead. This reabsorption can be avoided by calculating the optimal fiber length prior to amplifier construction.

3.1.2.4 Amplifier Dynamics and Response to High Frequency Signal

Rare-earth-doped fiber amplifiers are widely used to amplify true CW signals, pulses, and high frequency CW modulated signals. They are used at low and high powers. Thus there is generally little concern that their absorption and emission dynamics will distort the input intensity modulation, or that their power levels will become unstable. However, in the chaotic transmitter application, the amplifiers must boost high frequency CW signals to high powers, which is not commonly done. This high-frequency, high-power case is the most stressing for fiber amplifiers, and so it is appropriate to perform a numerical simulation to confirm expected behavior. This is discussed below (see Section 3.2.2.5).

3.1.3 Frequency Doubler

3.1.3.1 Theory of Second-Harmonic-Generating Crystals

Nonlinear crystals convert photon wavelengths by electromagnetic wave mixing. They can be used for second-harmonic generation (SHG), in which two incident photons of frequency ν_1 are absorbed, and a third photon of frequency $2\nu_1$ is generated (noting that energy $E_{\text{photon}} = h\nu_{\text{photon}}$, this is seen to be an exact conservation of energy). The wavelength $\lambda_{\text{photon}} = c/n u_{\text{photon}}$ is thus halved, while the power is unaltered. Potassium titanyl phosphate (KTP) is a nonlinear crystal commonly used for SHG on pulsed Nd:YAG and other infrared sources; it is often placed inside the resonator cavity of such lasers to achieve green output. By a periodic phase inversion, the crystal can be modified for efficient use as an external converter for CW infrared lasers. This periodically poled KTP (PPKTP) is the material chosen to generate green 532 nm photons from our infrared 1064 nm ytterbium fiber signal.

Periodically poled crystals are meant for narrow wavelength operation, and have a strong temperature dependence. Thus as temperature drifts, the doubled wave-

length will also change; typical optical 3 dB bandwidths are on the order of 0.1 nm. Nonlinear crystals are also designed for linear polarization, and any light that is orthogonally polarized relative to the operating plane will simply pass through with no conversion. Periodically poled crystals are designed to operate at high powers, and their efficiency increases quadratically with the incident power. In the case of our PPKTP, the manufacturer's estimate is that the output P_{532} 's conversion efficiency depends on the input P_{1064} at about 0.8%/W, or

$$P_{532} = P_{1064} * (P_{1064} * 0.008) = 0.008P_{1064}^2 \quad (3.4)$$

Thus for conversion efficiencies above, e.g. 5%, high infrared powers (> 6 W) must be used. Finally, the average intensity of the beam in the crystal must be maximized, which implies a tradeoff between small beam spot size (for maximum power density) and long beam focus length (for maximum interaction length).

3.1.3.2 Frequency Doubling System Design

The frequency doubling optical system will take a 1064 nm beam from the chaotic source, expand the beam, and then focus the beam into the PPKTP crystal (see Figure 3.11). Temperature will be controlled. The main design parameters of the doubling system are the beam width and the focusing length, which are discussed in Section 3.2.3.

3.2 Transmitter Calculations and Simulations

3.2.1 Fiber Ring Laser

3.2.1.1 Lasing Wavelength and Threshold (Analytical Solution)

Various methods of controlling the lasing wavelength are available. However, the wavelength discrimination needed for these methods to be effective depends on the free-running (uncontrolled) wavelength of the laser, which can be found using a gain map as Figure 3.12 [87]. The lasing wavelength is simply the first wavelength whose gain crosses the gain threshold as the pump power is increased. If a laser is most likely to lase at e.g. 975 nm (as in the figure, at 180 mW pump), and is "10 dB less likely" to lase at 1040 nm, then a grating will have to impose ≥ 10 dB of loss

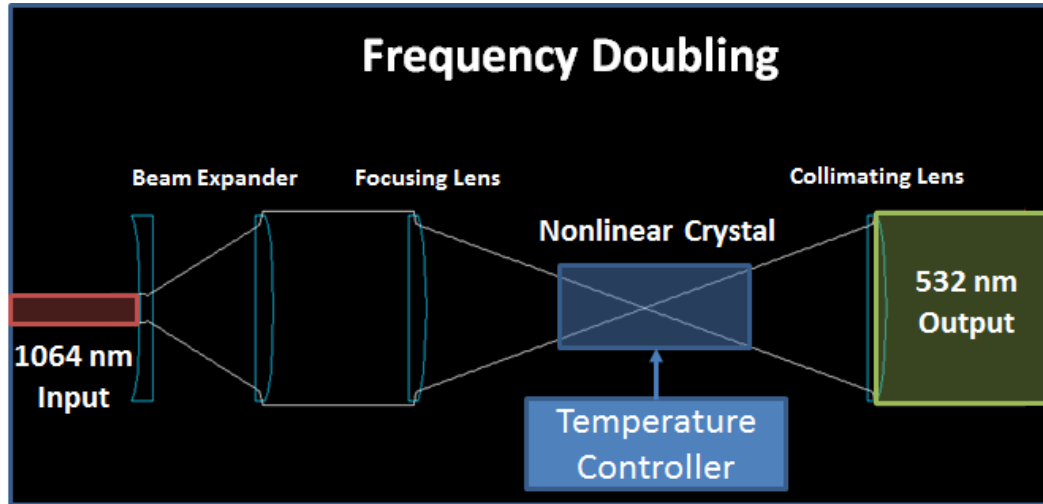


Figure 3.11: Frequency Doubling Using Nonlinear Crystal

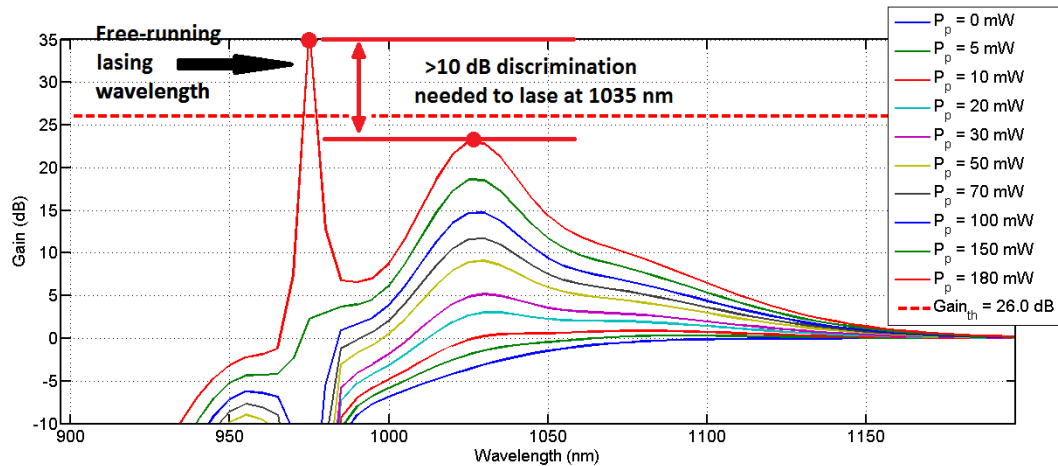


Figure 3.12: Example Gain Map for Ytterbium-doped Fiber Laser

on 975 nm relative to 1040 nm in order to achieve lasing at 1040 nm — this may or may not be easy to achieve. However, it is possible to control the free-running wavelength to a large degree, such that the “natural” operation of the laser will only need to be slightly modified to achieve the desired output wavelength. Variables by which the wavelength can be controlled include the active fiber length, the Q of the resonator, and the cavity losses including the output coupler transmission/reflection ratio.

The lasing wavelength is determined primarily by the losses δ_0 of the cavity. Lasing will occur when the round-trip gain G is higher than δ_0 , and this gain is not

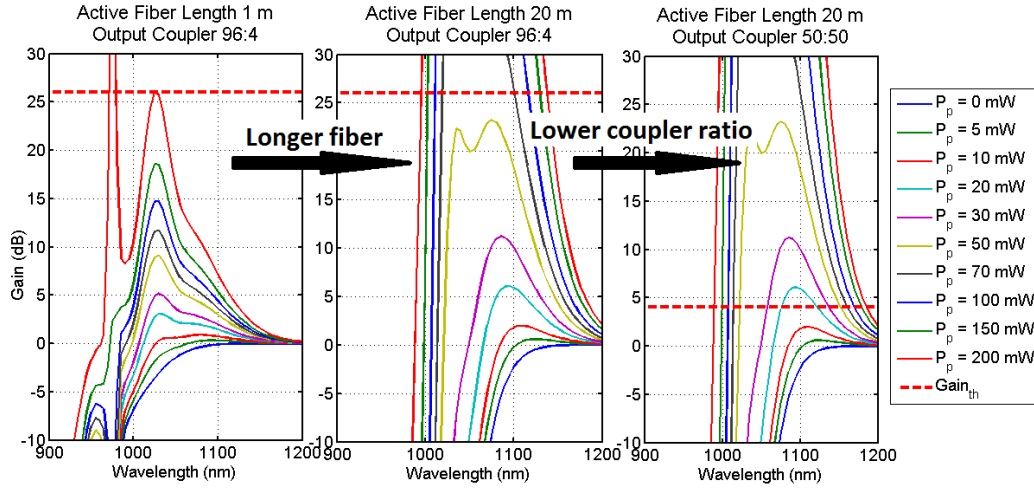


Figure 3.13: Gain maps showing effect of fiber length, and coupler ratio

constant across all wavelengths. Thus as the pump power P_P is increased from zero, the first wavelength λ whose gain $G(\lambda)$ exceeds δ_0 will be the lasing wavelength. (Subsequently increasing P_P will increase the output power but will not change the lasing wavelength.) Also, as P_P increases from zero, the gain increases for all wavelengths, but it increases faster for lower wavelengths. For high δ_0 , a high G and thus a high P_P will be necessary to overcome the losses. But a high P_P will most likely drive lasing at low wavelengths. Conversely, a lower δ_0 will usually result in lasing at lower P_P , typically at longer wavelengths. Changing the cavity length changes the Q , thus reducing the cavity losses for the resonating frequencies and thus decreasing the required gain (if the increased cavity length does not introduce significant losses of its own). Meanwhile, increasing the active fiber length introduces reabsorption at the lower wavelengths, but not at the higher wavelengths. Thus the longer wavelengths are much more likely to lase at high resonator Q , and at long active fiber lengths. Figure 3.13 shows this effect: increasing the active fiber length reabsorbs the lower wavelengths but adds gain to the higher wavelengths. Decreasing the coupler ratio lowers the lasing threshold and so effectively lengthens the lasing wavelength (decreasing the cavity losses would have the same effect).

The lasing wavelength and threshold can be calculated analytically, using terms defined in Table 3.1. First the saturation power is calculated for a given pump and fiber.

$$P_{sat} = \frac{h\nu_p A}{(\sigma_{ep} + \sigma_{ap})\tau\Phi_P} \quad (3.5)$$

The pump power at the end of the active doped fiber can then be computed, along with the power absorbed in the fiber.

$$\log\left(\frac{P_P(L)}{P_P(0)}\right) + \frac{P_P(L) - P_P(0)}{P_{sat}} = -N\sigma_{ap}L \quad (3.6)$$

$$P_a = P_P(0) - P_P(L) \quad (3.7)$$

The single-pass gain in the fiber can then be computed (given here in decibels).

$$G = 4.34\left[\frac{\Phi_p(\sigma_{el} + \sigma_{al})\tau P_a}{Ah\nu_p} - N\sigma_{al}L\right] \quad (3.8)$$

A useful plot of the gain at each wavelength, for various pump powers, can then be made. The first wavelength whose single-pass gain reaches the cavity loss will be the lasing wavelength, and the absorbed pump power that generates this gain will be the threshold pump power.

3.2.1.2 Lasing Power and Efficiency (Analytical Solution)

The lasing efficiency can be calculated from

$$\eta = \frac{(1 - R) \lambda_p}{\delta_0} \frac{\lambda_l}{\lambda_l} \quad (3.9)$$

The output power can then be obtained from the efficiency, the threshold pump power, and the absorbed power.

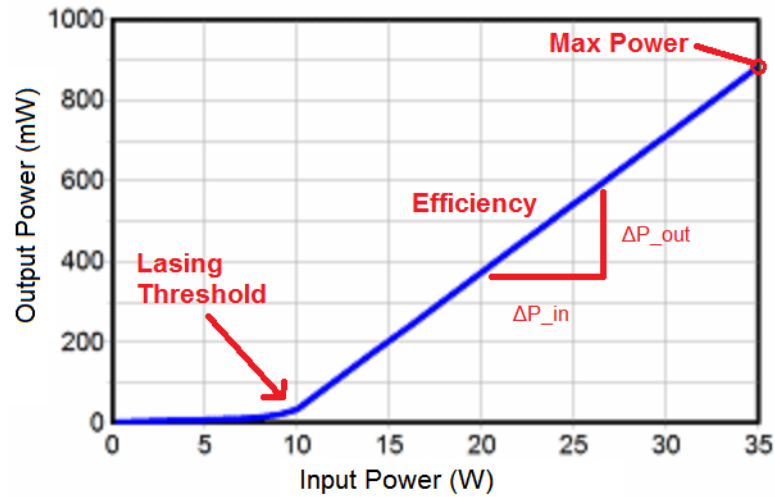
$$P_{out} = \eta(P_a - P_{th}) \quad (3.10)$$

3.2.1.3 Comparison of Performance of Various Designs

The output power from a fiber ring can be very high, but tradeoffs may be necessary between efficiency, lasing threshold, and wavelength control. High efficiency can be obtained by using a high-ratio output coupler, but this will also result in a high

Table 3.1: Fiber Ring Laser Calculation Parameters (Ytterbium)

Parameter	Symbol	Value	Units	Description
Wavelength	λ	[variable]	m	976 pump, many λ may lase
Pump absorption coeff.	σ_{ap}	3×10^{25}	m^{-2}	Absorption at 976 nm
Pump emission coeff.	σ_{ep}	3×10^{25}	m^{-2}	Emission at 976 nm
Laser absorption coeff.	σ_{al}	[varies]	m^{-2}	Absorption at all λ [88]
Laser emission coeff.	σ_{el}	[varies]	m^{-2}	Emission at all λ [88]
Cavity loss	δ_0	[calculated]	1	Total P lost, round trip
Output reflectance	R	[variable]	1	P reflected to cavity
Gain	G	[calculated]	1	Gain in active fiber
Distance	z	0	m	0 at pump end of active fiber
Pump power	$P_P(z)$	[variable]	W	
Absorbed pump power	P_a	[calculated]	W	P_P absorbed in active fiber
Saturation pump power	P_{sat}	[calculated]	W	P_P reducing σ_{ap} by 2x
Threshold pump power	P_{th}	[calculated]	W	P_a at lasing threshold
Laser efficiency	η	[calculated]	1	Slope of P_{out} vs P_a
Dopant ion concentration	N	4×10^{25}	m^{-3}	Total dopant per volume
Photon frequency	ν_p	c/λ	Hz	
Fiber cross section	A	30×10^{-12}	m^2	Doped core cross-section
Upper state lifetime	tau	10^{-3}	s	Spontaneous decay halflife
Quantum efficiency	Φ_P	1	1	Photons out per photon in

**Figure 3.14: Example laser power curve showing lasing threshold, max power, and efficiency**

lasing threshold and may reduce total output power. Likewise, a short active fiber length will give a low lasing threshold, but a very high discrimination wavelength control will be needed to lase at longer (>1030 nm) wavelengths. And, wavelength control may in some cases be helped by extra components, e.g. isolators or circulators, but these will decrease the efficiency.

Care must also be taken when operating at 1064 nm: there are many good fiber ring laser designs in the literature at 1550 nm, but most become inefficient or impossible at 1064 nm. For example, 1550 nm ring lasers often use 0.1-1.0 nm-wide tunable bandpass filters for wavelength control, but at 1064 nm such narrow filters are not widely available; 1064 nm filters are usually at least 8 nm wide, and often much wider. As an alternative to bandpass filters, 1550 nm lasers often use circulators to direct the laser path to reflective fiber Bragg gratings (FBGs) for wavelength control. But while circulators at 1550 nm have total insertion losses of about 1 dB, a standard 1064 nm circulator will typically add 4-5 dB to a cavity loss. Similarly, if a given manufacturer offers 1550 nm isolators with 0.5 dB loss, their 1064 nm model will likely have up to 2 dB loss. Thus the guiding rule at 1064 nm must be to minimize components used, especially avoiding circulators, while still finding ways to use reflective wavelength control (i.e. FBGs) since bandpass filters are not effective.

Taking these factors into account, we can compare the performance of several possible fiber ring laser designs: a circulator-based ring [89] and two external-reflector topologies: we will call them the “feedback-reflector” and the “reversing-reflector” for clarity [90,91]. Using 1064 nm components from a single vendor (Thorlabs) for consistency across cases, we posit insertion losses for the isolator (1.8 dB), the circulator (4.2 dB), the WDM (0.5 dB), and the coupler (0.2 dB), with an additional 0.1 dB per component for fusion splice loss. Then the circulator-ring has ~ 7.4 dB loss, the feedback-reflector has ~ 3.2 dB losses, and the reversing-reflector has just ~ 1.1 dB losses. Using these cavity loss numbers, coupling ratios from the literature, and assuming that each design can deliver 20 dB of wavelength suppression via identical FBGs, performance can then be compared in terms of lasing threshold (at 1064 nm) and efficiency. A simple single-number comparison is to calculate the output power

when 250 mW of pump power is absorbed; since we have single-mode pumps ranging up to 300 mW launched, this is a realistic upper limit on the pump power that reaches the active fiber. Performance is also compared for various output coupler ratios and active fiber lengths, to try to optimize each design's parameters for 250 mW absorbed pump.

Table 3.2: Performance Comparison Between Ring Laser Designs

Value	Circ.	R.R.	F.R.
T:R	50:50	80:20	80:20
δ_0	7.4dB	1.1dB	3.2dB
η	48%	84%	80%
P_{th}	80mW	30mW	50mW
L_{th}	1.25m	0.5m	1.0m
LD_{1030}	16dB	7.5dB	7dB
G_{th}	22.0dB	8.1dB	13.1dB
P_{250}	82mW	184mW	159mW

P_{th} : Pump power absorbed at threshold; L_{th} : Active fiber length; LD_{1030} : Loss difference imposed on 1030 nm peak to allow 1064 nm to lase; G_{th} : Single-pass gain; P_{250} : Output power at 250 mW pump absorbed; T:R:

Transmittance:reflectance ratio of output coupler; δ_0 : Cavity losses

The most promising topology is the reversing-reflector, with its few components and minimized insertion loss. The reversing reflector has both the highest efficiency and the lowest threshold, so it will produce the highest output power. If the reversing-reflector can achieve true unidirectional propagation, it should generate a high power signal at the correct wavelength, with no corrupting interference. Varying the output coupler and fiber length, the best combination can be confirmed.

Table 3.3: Performance Comparison Between Coupling Ratios (Reversing-Reflector)

Value	50:50	80:20	90:10
η	57%	84%	89%
P_{th}	20mW	30mW	50mW
L_{th}	0.25m	0.25m	0.5m
LD_{1030}	5dB	7.5dB	14dB
G_{th}	5.2dB	8.1dB	14.3dB
P_{250}	131mW	184mW	178mW

The expected lasing thresholds, single-pass gain, and necessary wavelength dis-

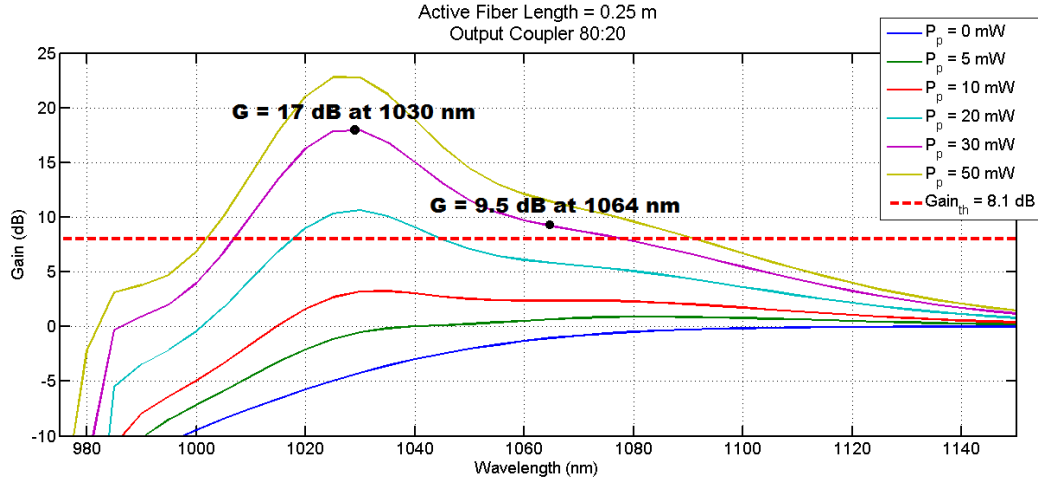


Figure 3.15: Gain Map for the Reversing-reflector Ring Laser

crimination are found by the gain map for the reversing-reflector lasing at 1064 nm (as shown in Figure 3.15 and compared for various coupler ratios in Table 3.3).

3.2.2 Fiber Amplifiers

Small-signal gain calculations, similar to the laser single-pass gain calculation, are helpful for approximating the required parameters, but for high-power amplification, gain saturation will always be a concern. Steady-state numerical simulation can help with proper selection of pump power, active fiber length, and other parameters in the fiber amplifiers. Ultimately, dynamic numerical simulation is required for this high-frequency, high-power amplifier chain, to ensure that this stressing case will not result in distortion of the intensity-modulated signal.

3.2.2.1 Pump Absorption and Small-Signal Gain (Analytical Solution)

Small-signal gain for the preamplifier is shown. The methodology is just as described for the fiber laser: the absorbed pump is calculated, and this determines the gain from stimulated emission. Figure 3.16 shows that while increasing pump power leads to exponential signal gain, the length of the fiber determines the total gain in the system and thus the maximum pump power that can be effectively absorbed and used for amplification. Unfortunately this analysis is not definitive since it does not account for gain depletion by the increasingly large signal. Additionally, it is

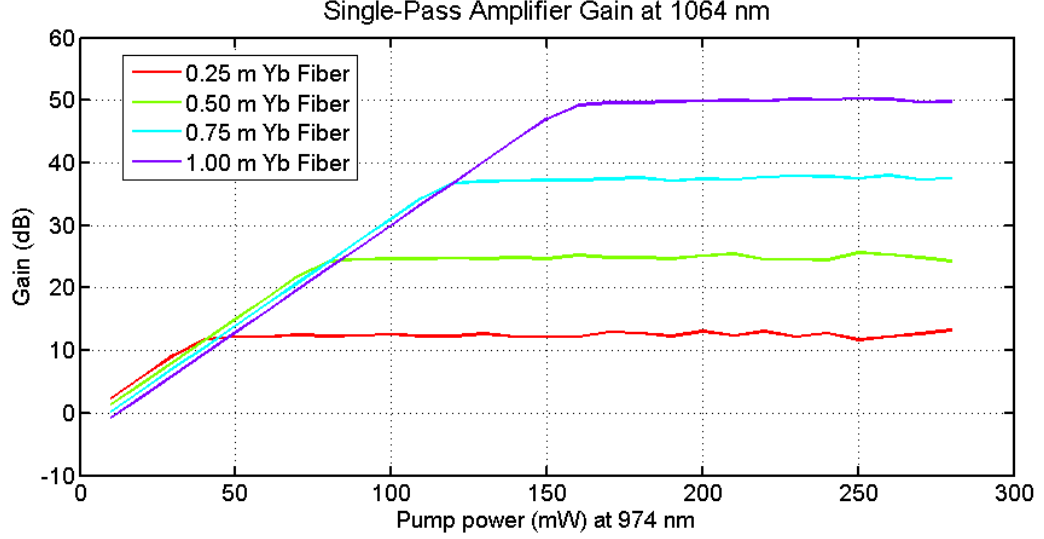


Figure 3.16: Preamplifier small-signal gain for various fiber lengths

suspect, since it is known that single-pass gains exceeding 30 dB will usually lead to strong and undesired ASE [87, 92]. Thus more detailed numerical simulation is required.

3.2.2.2 Steady-State Signal Amplification in Saturating Conditions (Numerical Simulation)

Steady-state numerical calculation is done by solving an ordinary differential equation (ODE) system along the length of the fiber [92]. Since the solution is steady-state, no time-domain terms are required. The system is described by the steady-state inversion in terms of pump and signal transition rates

$$n_2(z) = N_2(z)/N_{tot} = \frac{R_{12} + W_{12}}{R_{12} + R_{21} + W_{12} + W_{21} + A_{21}} \quad (3.11)$$

$$n_1(z) = N_1(z)/N_{tot} = 1 - n_2$$

where the transition rates are

$$\begin{aligned}
R_{12} &= I_P \frac{\sigma_{12}^P}{h\nu_p} \\
R_{21} &= I_P \frac{\sigma_{21}^P}{h\nu_p} \\
W_{12} &= I_S \frac{\sigma_{12}^S}{h\nu_s} \\
W_{21} &= I_S \frac{\sigma_{21}^S}{h\nu_s} \\
A_{21} &= \frac{1}{\tau}
\end{aligned} \tag{3.12}$$

The pump and signal powers are then propagated along the fiber according to

$$\begin{aligned}
\frac{dP_P}{dz} &= \eta_P(\sigma_{21}^P n_2(z) - \sigma_{12}^P(1 - n_2))N_{tot}P_P(z) \\
\frac{dP_S}{dz} &= \eta_S(\sigma_{21}^S n_2(z) - \sigma_{12}^S(1 - n_2))N_{tot}P_S(z)
\end{aligned} \tag{3.13}$$

where $N_1(z)$ and $N_2(z)$ are the ground and excited state ion populations along the fiber, N_{tot} is the total dopant ion population, and $P_P(z)$ and $P_S(z)$ are the propagating pump and signal powers (forward- and backward-propagating beams are both included in the calculation). The intensities $I_P(z)$ and $I_S(z)$ are related to the power by $I(z) = P(z)/A$, where A is the core cross-sectional area. The pump and signal absorption cross-sections are σ_{12}^P and σ_{12}^S , and the pump and signal emission cross-sections are σ_{21}^P and σ_{21}^S . The spontaneous emission is described by τ , the upper state lifetime. Overlap of the pump and signal with the doped core is accounted for by η_P and η_S , which is important for cladding-pumped amplifiers. The quantum defect is accounted for by the pump and signal photon energies $h\nu_p$ and $h\nu_s$.

The solver assumes no excitation at first. The pump and signal power are inputs at the left end of the fiber, and they are propagated down the fiber each calculation step. The excitation is recalculated, and the propagation performed again based on the new excitation values. After the solution converges, the expected signal

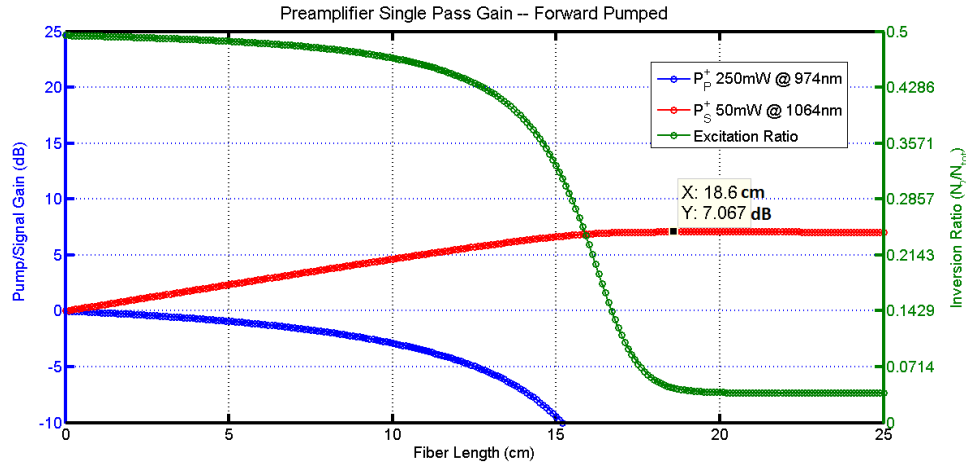


Figure 3.17: Preamplifier Steady-state Gain Saturation

amplification and best fiber length can be seen for a given input pump and signal. An example solution is shown in Figure 3.17 for a 250 mW core-pumped amplification of a 50 mW signal (giving margin to the expected fiber laser output power for insertion loss and unexpected inefficiency). Here the signal gains 7.1 dB, for a signal output power of 254 mW. Subtracting the initial 50 mW signal, the conversion efficiency is $204 / 250 = 82\%$. Expected performance versus fiber length and pump power can be expected by solving several different scenarios (see Figure 3.18). It is interesting that with this high power 50 mW input signal, the pump is fully depleted in all but the shortest fiber lengths, whereas when a 1 mW input signal is used, even 50 and 75 cm fibers are not enough to fully absorb the pump, and transparency occurs. High signal powers clearly can lead to more efficient amplifiers.

3.2.2.3 Comparison of Steady-State Performance of Various Designs

Different amplifier designs have different insertion losses, before or after the active fiber, and thus they will have different efficiency. Starting with a 280 mW pump and a 20 mW signal, the input insertion losses are given in Table 3.4, assuming losses of 0.5 dB for WDM (W), 1.5 dB for isolator (I), 4 dB for circulator (CR), and 0.5 dB for a coupler (CP). Simulating all four configurations (the forth is a double-pass amplifier with a reflector at one end [88]), the gain across the fiber is seen in Figure 3.19, and the final output power, incorporating insertion losses at

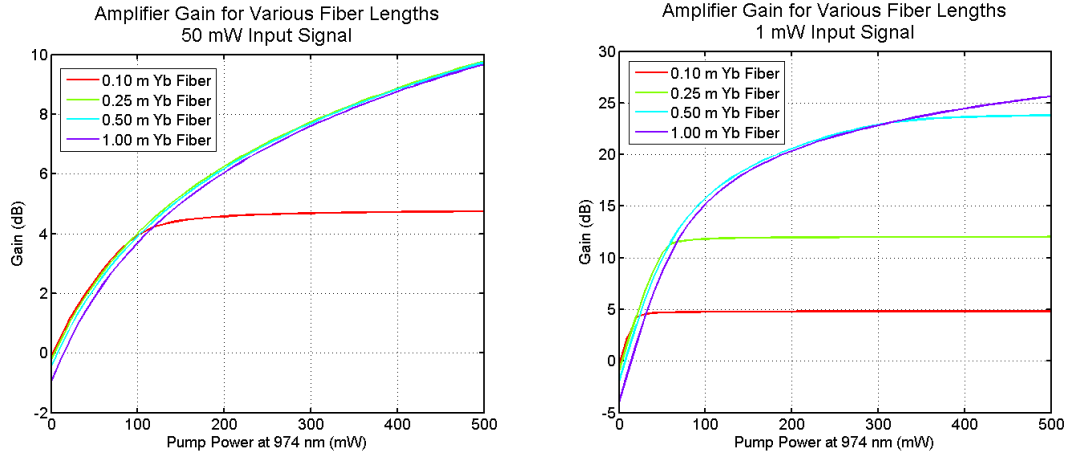


Figure 3.18: Preamplifier steady-state gains for various fiber lengths and pump powers. Left: A 50 mW signal strongly depletes the pump, and transparency occurs only for the 10 cm fiber length. Right: 1 mW input does not deplete the gain, and so the pump absorption is much less. Transparency occurs even for long fibers.

Table 3.4: Preamplifier Input Values

Configuration	Pump IL	Signal IL	P_P to Fiber	P_S to Fiber
SP Forward	0.5 dB (W)	2 dB (W/I)	250 mW	32 mW
SP Backward	0.5 dB (W)	2 dB (W/I)	250 mW	32 mW
SP Bidirectional	1 dB (2xW)	2 dB (W/I)	225 mW	32 mW
DP Forward	0.5 dB (W)	6 dB (W/I/CR)	250 mW	13 mW

P_P : Pump power; P_S : Signal power; IL: Insertion loss; SP: Single-pass; DP: Double-pass

the output, is given in Table 3.5. These relative comparisons make it clear that the single-pass forward-pumped arrangement is the most efficient for our purposes, so it will be used for both the preamplifier and the gain amplifier.

Using a core-pumped single-pass forward-pumped preamplifier with an input signal of 50 mW and a pump power of 280 mW, we then expect to generate about 8.5 dB gain for an output power of 230 mW (Figure 3.19). After ~ 2 dB of insertion losses from an isolator and a combiner, approximately 150 mW will enter the gain amplifier. This cladding-pumped single-pass forward-pumped amplifier will yield >19 dB gain for an output of 12.5 W when pumped with 20 W of multimode 915

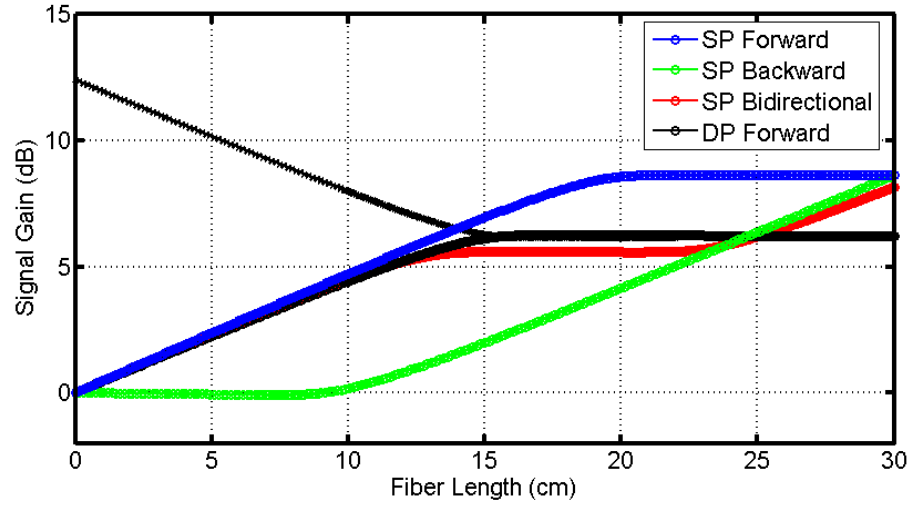


Figure 3.19: Preamplifier steady-state gains for various amplifier configurations

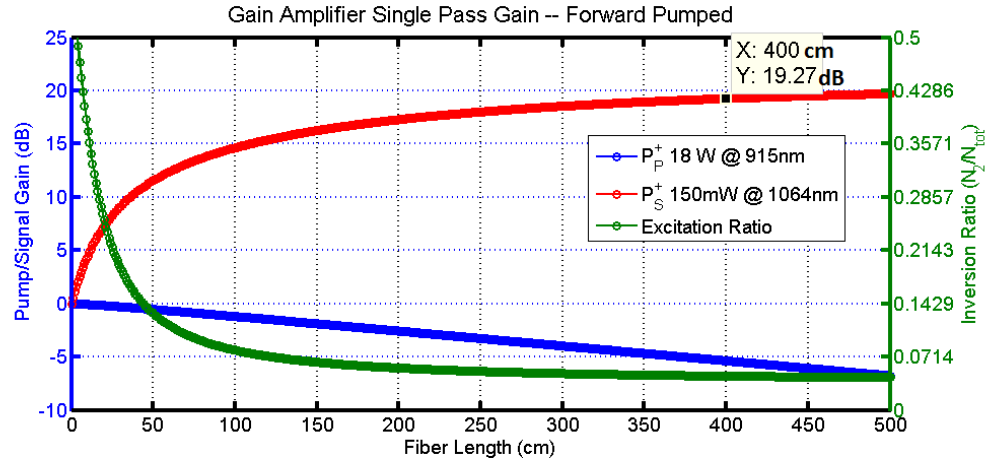


Figure 3.20: Gain amplifier steady-state gain for predicted signal and pump inputs

Table 3.5: Preamplifier Output Values

Configuration	η	G	P_{out} Fiber	L_{out}	P_{out} Preamp
Units	%	dB	mW	dB	mW
SP Forward	80	8.6	233	0	233
SP Backward	79	8.6	230	0.5 (W)	205
SP Bidirectional	79	8.1	207	0.5 (W)	184
DP Forward	82	12.4	218	4.5 (W/CR)	77

η : Efficiency; G: Gain; P_{out} : Output power; L_{out} : Output insertion losses; SP: Single-pass; DP: Double-pass

nm energy (Figure 3.20). After a final isolator (IL ~ 1.5 dB), the power to free space should be approximately 9 W.

3.2.2.4 Amplified Spontaneous Emission and Amplifier Limits (Numerical Simulation)

The ultimate amplifier limit is the quantum defect:

$$\eta_{max} = h\nu_p/h\nu_s \quad (3.14)$$

However, practical amplifiers will usually be limited by the signal gain achieved before the onset of strong ASE. Numerical simulation of multiple wavelengths is thus required for high-gain stages. (As a rule of thumb, ASE is unlikely to occur for small-signal gains below 20 dB, but should be considered for higher-gain stages and for highly saturated amplifiers [87, 92].) ASE channels can be incorporated in an ODE simulation [93], but since we developed a PDE model (see below) to account for the time-varying input signal, we included multiple ASE channels there.

3.2.2.5 Modulated Signal Amplification Dynamics (Numerical Simulation)

We performed a PDE simulation as a final solution to the various concerns of ASE, intensity-modulated input, and transient response of the amplifiers. These calculations describe core- or cladding-pumped amplifiers [94]. Solution of these equations give: the forward propagating power $P^+(z, t, \lambda_k)$ for all position, time, and wavelengths of interest; the backward propagating power $P^-(z, t, \lambda_k)$ moving from output to input; and the excited state population $N_2(z, t)$ at all points on the fiber.

$$\begin{aligned}
\frac{\delta P^+(z, t, \lambda_k)}{\delta z} + \frac{1}{v} \frac{\delta P^+(z, t, \lambda_k)}{\delta t} &= \eta_k [\sigma_{e,k} N_2(z, t) - \sigma_{a,k} N_1(z, t)] \\
&\quad * P^+(z, t, \lambda_k) - \alpha_k P^+(z, t, \lambda_k) \\
&\quad + 2\sigma_{e,k} N_2(z, t) \frac{hc^2}{\lambda_k^3} \Delta\lambda + S\alpha_{RS,k} P^-(z, t, \lambda_k), k = 1 \dots K
\end{aligned} \tag{3.15}$$

$$\begin{aligned}
\frac{\delta P^-(z, t, \lambda_k)}{\delta z} + \frac{1}{v} \frac{\delta P^-(z, t, \lambda_k)}{\delta t} &= \eta_k [\sigma_{e,k} N_2(z, t) - \sigma_{a,k} N_1(z, t)] \\
&\quad * P^-(z, t, \lambda_k) - \alpha_k P^-(z, t, \lambda_k) \\
&\quad + 2\sigma_{e,k} N_2(z, t) \frac{hc^2}{\lambda_k^3} \Delta\lambda + S\alpha_{RS,k} P^+(z, t, \lambda_k), k = 1 \dots K
\end{aligned} \tag{3.16}$$

$$\begin{aligned}
\frac{\delta N_2(z, t)}{\delta t} &= \frac{1}{hcA} \sum_{k=1}^K \{ \eta_k \lambda_k [\sigma_{a,k} N_1(z, t) - \sigma_{e,k} N_2(z, t)] \\
&\quad * (P^+(z, t, \lambda_k) + P^-(z, t, \lambda_k)) \} - \frac{N_2(z, t)}{\tau}
\end{aligned} \tag{3.17}$$

These parameters are as described before, with additional uses of: c , the speed of light in a vacuum; α , the attenuation in the fiber; $S\alpha_{RS}$, the Rayleigh scattering occurring in the direction counter to propagation; and v , the wave speed in the medium ($v = c/n_{fiber}$, where n_{fiber} is the index of refraction). Parameter values used in simulation are given in Tables 3.6 and 3.7.

The initial and boundary conditions vary with amplifier configuration. In the case of forward-pumped amplifiers, the backward power at the fiber output may be set to zero for all wavelengths for all time. The forward power at the fiber input is zero for all wavelengths except the pump and signal, whose powers are known for all time. The excited state population can initially be set to zero, but no boundaries

Table 3.6: Preamplifier YDFA Dynamic Simulation Parameters

Parameter	Symbol	Value	Units	Description
Pump wavelength	λ_P	976	nm	Core-pumped
Signal wavelength	λ_S	1064	nm	
ASE wavelength	λ_k	1020-1100	nm	Steps of 2 nm
Pump absorption coeff.	σ_{ap}	24.8×10^{25}	m^{-2}	Absorption at 976 nm
Pump emission coeff.	σ_{ep}	24.8×10^{25}	m^{-2}	Emission at 976 nm
Signal absorption coeff.	σ_{as}	1.3×10^{26}	m^{-2}	Absorption at 1064 nm
Signal emission coeff.	σ_{es}	3.0×10^{25}	m^{-2}	Emission at 1064 nm
ASE absorption coeff.	σ_{ak}	[varies]	m^{-2}	From [88]
ASE emission coeff.	σ_{ek}	[varies]	m^{-2}	From [88]
Input pump power	P_P	250	mW	Forward power at fiber
Input signal amplitude	P_S	32	mW	At fiber; avg. power
Input signal frequency	f_S	1×10^9	Hz	Sinusoid modulation
Fiber length	L	30	cm	Active doped fiber
Gain	G	[calculated]	1	$10 \log_{10}(P_{out,S}/P_S)$
Attenuation coeff.	α	3×10^{-3}	m^{-1}	With propagation
Scattering coeff.	$S\alpha_{RS}$	1.2×10^{-7}	m^{-1}	Against propagation
Amplifier efficiency	η	[calculated]	1	$(P_{out,s} - P_S)/P_P$
Dopant ion concentration	N	6×10^{25}	m^{-3}	Total dopant per volume
Fiber cross section	A	30×10^{-12}	m^2	Doped core cross-section
Doped core overlap	Γ	0.85	1	Signal and pump same
Upper state lifetime	τ	0.84	ms	Spontaneous decay halflife
Index of refraction	n	1.5	1	SiO_2 glass fiber host

Table 3.7: Gain Amplifier YDFA Dynamic Simulation Parameters

Parameter	Symbol	Value	Units	Description
Pump wavelength	λ_P	915	nm	Cladding-pumped
Pump absorption coeff.	σ_{ap}	8×10^{25}	m^{-2}	Absorption at 915 nm
Pump emission coeff.	σ_{ep}	5×10^{26}	m^{-2}	Emission at 915 nm
Input pump power	P_P	18	W	Forward power at fiber
Input signal amplitude	P_S	150	mW	At fiber; avg. power
Fiber length	L	500	cm	Active doped fiber
Pump core overlap	Γ_P	0.01	1	Cladding/core ratio
Signal core overlap	Γ_S	0.85	1	Spatial mode overlap

Values not listed are identical to those used for preamplifier.

are enforced.

Initial Conditions:

$$\begin{aligned}
 P^+(z, 0, \lambda_k) &= 0 \\
 P^-(z, 0, \lambda_k) &= 0 \\
 N_2(z, 0) &= 0
 \end{aligned} \tag{3.18}$$

Boundary Conditions:

$$\begin{aligned}
 P^+(0, t, \lambda_P) &= P_P \\
 P^+(0, t, \lambda_S) &= P_S \\
 P^+(0, t, \lambda_k) &= 0, k \neq P, S \\
 P^-(0, t, \lambda_k) &= 0, \text{all } k
 \end{aligned} \tag{3.19}$$

Here, $P^+(0, t, \lambda_P)$ is the known pump power, and $P^+(0, t, \lambda_S)$ is set to the input signal power. It is understood that there is no other input, thus $P^+(0, t, \lambda_k) = 0$ while k is not P or S . Similarly, no signals are inserted from the end of the fiber, thus $P^-(0, t, \lambda_k) = 0$ for all k . The primary values of interest are then the output signal power $P^+(L, t, \lambda_S)$, the residual (unabsorbed) pump power $P^+(L, t, \lambda_P)$, and the shape of the excitation along the fiber $N_2(z, t)$. For a modulated signal, either pulsed or CW, the boundary condition relating to the input signal must be modified. Rather than maintaining a constant value, $P^+(0, t, \lambda_S)$ is computed as a function of simulation time, and can be made any arbitrary time-domain waveform.

The simulation of these fiber amplifiers was performed using the finite-difference time-domain (FDTD) explicit method, with forward marching time steps and a first-order approximation for the derivatives. Starting with the initial conditions, and using the boundary conditions, we march these updates forward in time until convergence is achieved on each of the output variables (either a steady state in the case of constant input, or a periodic function in the case of periodic inputs). Thus the amplifier behavior can be fully predicted for any input, pump, and initial-boundary conditions. This simulation was implemented in Fortran 90. Visualization

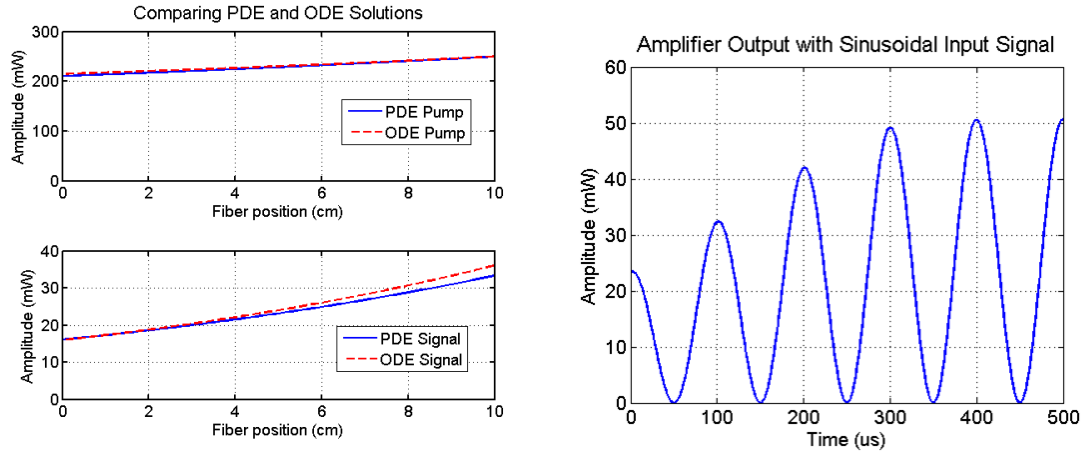


Figure 3.21: Fiber amplifier dynamic simulations. Left: Validation that the unmodulated PDE result matches the ODE well, noting the PDE has additional terms that attenuate the signal slightly. Right: Dynamic simulations show the modulated output of the fiber amplifier, and the transient time to final peak amplitudes.

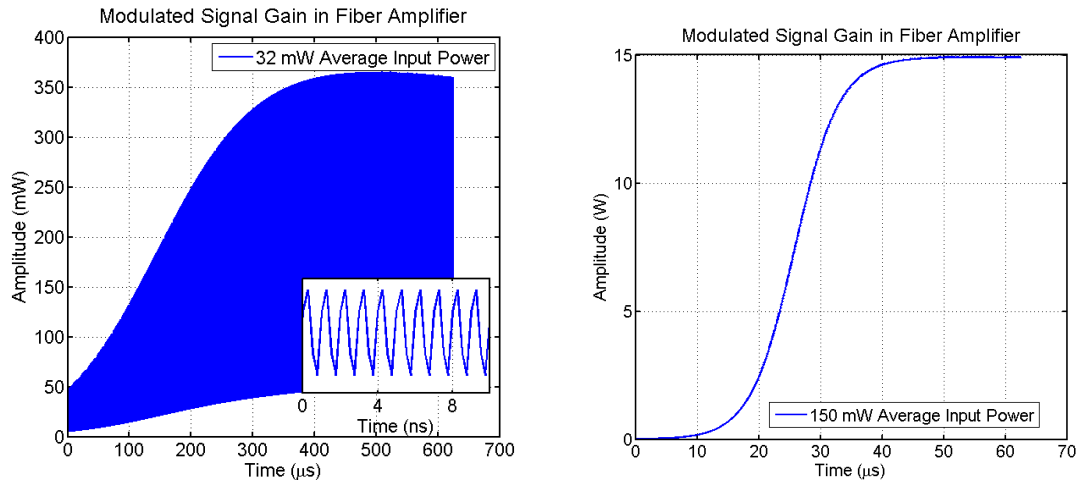


Figure 3.22: Amplifier dynamic simulation using 1 GHz intensity modulation. Left: The preamplifier's output modulation reproduces the input signal; the average amplitude matches the DC (unmodulated) prediction. Right: Gain amplifier output is also satisfactory at high frequencies.

of the Fortran-generated output was done using Matlab.

Performing this PDE simulation showed that the gain amplifier dynamics were robust enough to handle the high frequency intensity modulation expected from the input signal. As shown in Figure 3.21, the output amplitude shows the same intensity modulation as the input amplitude, with no obvious distortion. The transient envelope can also be seen; it is small relative to the planned operating timescale of the system, but it is worth noting that the system takes some finite time to achieve full power when starting from zero inversion. In Figure 3.22, the output modulation is plotted for a 1 GHz input sinusoid, for both the preamp and the gain amp. Since there is no distortion on this high frequency signal, we expect these amplifiers to faithfully reproduce the DC-1 GHz input signals of the transmitter.

3.2.3 Frequency Doubler

3.2.3.1 Efficiency and Output Power

The frequency doubler is expected to generate green light at a single-pass efficiency that is approximately quadratic with the input power. Data from the manufacturer indicated the efficiency shown in Figure 3.23, suggesting that 10 W infrared would yield nearly 1 W of green light. Also shown is the instantaneous bandwidth of the conversion, limited to about 0.1 nm optical wavelength. (A wide range of center wavelengths can be used by simply tuning crystal temperature, but only 0.1 nm, or 18 GHz, will be operated on at once.) This informs the choice of a fiber Bragg grating at the seed laser: the lasing bandwidth should be limited to about 0.1 nm so as to efficiently pass through the crystal.

3.2.3.2 Beam Shaping and Power Density

It must be noted that the best-case efficiency given is likely to be difficult to achieve practically. This is so because of the polarization dependence of the crystal, and the crystal's response to power density rather than to launched power. Only a single polarization will be operated on, so any nonlinear polarization elements in the infrared beam will pass through unaffected. Since maintaining truly linear polarization is unlikely given the amount of birefringence in the fiber system, an

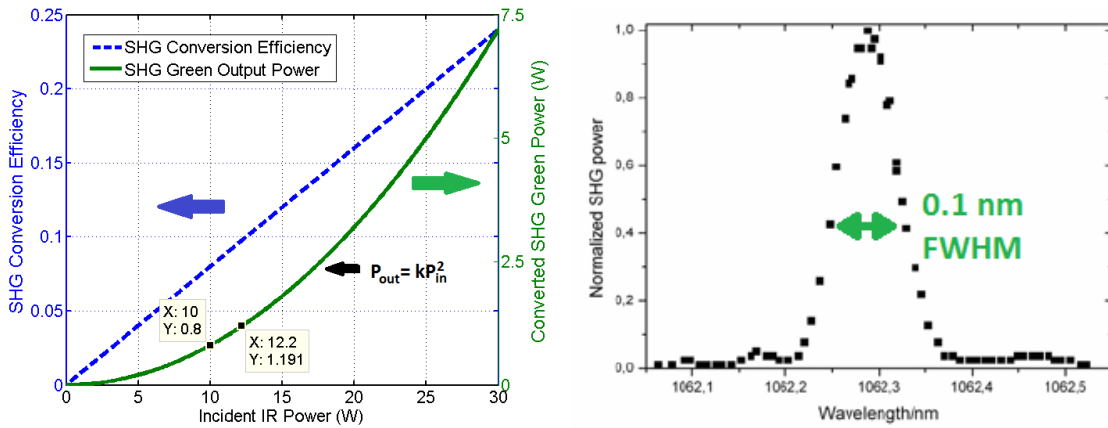


Figure 3.23: Nominal values for SHG crystal conversion efficiency and bandwidth. Left: Efficiency increases with input power; an output of 1 W green requires >10 W infrared. Right: Instantaneous bandwidth is about 0.1 nm, so the laser bandwidth should be limited accordingly.

elliptical polarization is to be expected, and a linearly polarized fraction of e.g. 75% should be estimated relative to the total power in the IR beam.

There is a tradeoff in beam shape between maximum power density and maximum interaction volume: a very small focus point can be obtained only with a large initial beamwaist and a fast focusing lens [95]. However, this setup will lead to a quickly diverging beam away from the focus point, and so it becomes unlikely that the entire beam will remain inside the 0.5 x 0.5 mm cross section of the crystal for the entire 20 mm interaction length. An alternative is to use a slow focusing lens, maximizing interaction volume, but sacrificing power density, since the focus spot will be larger. This tradeoff is shown in Figure 3.24, and is quantified by the Rayleigh range. The Rayleigh range is the distance from the focus at which the beam diameter is twice the diameter of the focus spot size. Conceptually, a longer Rayleigh range translates to a longer beam with a wider focus spot that will fill most of the crystal, and will be mostly contained within the crystal. A shorter Rayleigh range corresponds to a short, small focus that will be very high density at the focus spot, but will quickly escape the crystal. An industry rule of thumb is that the Rayleigh range of the focused beam should be half of the length of the crystal, or

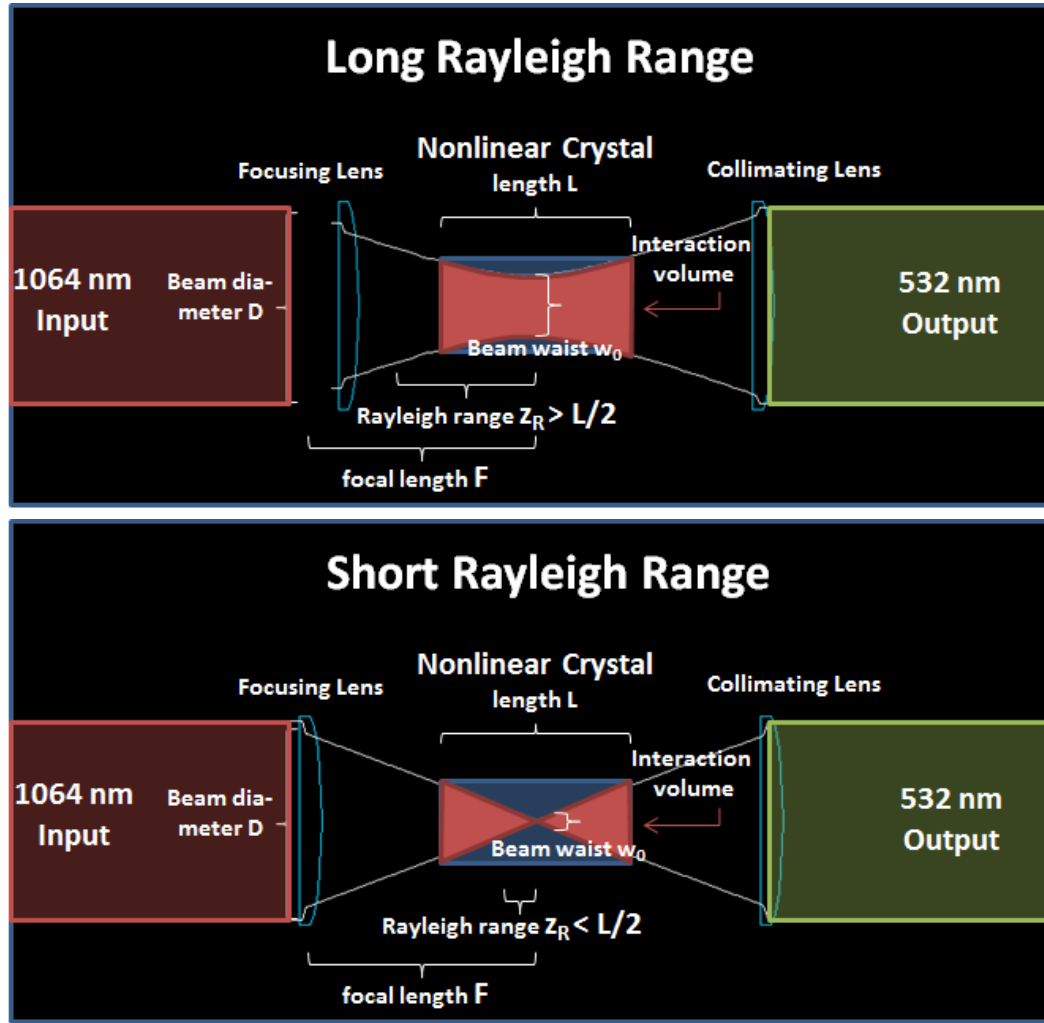


Figure 3.24: IR Beam Interaction with Crystal for Short and Long Rayleigh Lengths

$$z_R \approx L/2 = 10mm \quad (3.20)$$

which maximizes the average intensity in the crystal (here z_R is the Rayleigh range and L is the total length of the crystal). Moreover, the Rayleigh range is only a function of the beam waist radius w_0 , the mode quality M^2 , and the wavelength λ [96], as

$$z_R = \frac{\pi w_0^2}{\lambda M^2} \quad (3.21)$$

and therefore can be set by selection of the desired beam waist, i.e. focal spot size. The spot size obtained using a given beam and lens is determined by the $1/e^2$ diameter D of the Gaussian beam incident on the lens, and the focal length F of the lens [97], as

$$w_0 = \frac{2\lambda}{\pi} \left(\frac{F}{D} \right) \quad (3.22)$$

which implies that for any diameter beam, a lens focal length can be chosen that will yield the appropriate Rayleigh range (or vice versa, if the lens F is fixed):

$$\frac{F}{D} = \sqrt{\frac{\pi M^2 z_R}{4\lambda}} \quad (3.23)$$

In our case we assume a 10 mm Rayleigh range and a wavelength of 1064 nm, and a mode quality of 1.15. Practically, the beam diameter can be conveniently and continuously varied by means of a telescope, but lens choices are discrete and must be at least 100 mm to account for lab mounting equipment. Choosing the beam size by

$$D = F \sqrt{\frac{4\lambda}{\pi M^2 z_R}} = (1/f\#)F = 0.34F \quad (3.24)$$

implies a desired beam diameter of 34 mm for a 100 mm focusing lens. Acknowledging that the mode quality and the beam size are difficult to measure directly, slight experimental variation is expected, and the telescope lens controlling beam size is placed on a translation stage.

If the 75% linear polarization holds true, and 9 W is indeed the output to free space of the amplifiers $P_{1064,amp}$, then the expected green output P_{532} can be calculated as

$$P_{1064} = P_{1064,amp} * T_{optics} * 0.75 \quad (3.25)$$

$$P_{532} = P_{1064}(0.008 * P_{1064}) \quad (3.26)$$

where T_{optics} is the net transmission of the free space optical components, which may be as low as 60% for Fresnel reflective lenses and low-grade mirrors, or much

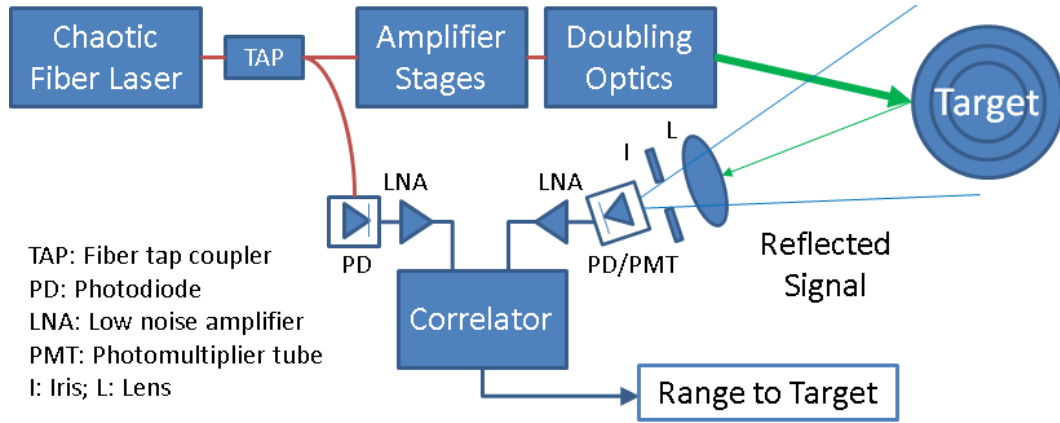


Figure 3.25: Ranging Setup Using Chaotic Transmitter

higher in the case of anti-reflection coated lenses. In any case, a green output power in the range of 150-300 mW can be reasonably expected.

3.3 Applications and Proposed Implementation

3.3.1 Rangefinding

With its wide bandwidth and high frequency content, the chaotic transmitter is well-suited for underwater ranging. To measure the distance to a target, the laser output is split into a reference and a probe signal, and the probe signal is reflected off a target [82, 83]. On its return, the probe signal is cross-correlated with the reference signal; the lag in the correlation indicates the round trip distance to the target. Figure 3.25 shows how this approach can be used in a practical ranging system. The correlator indicated can be either analog or digital. If the correlator is analog, the output of the system will be the cross-correlation value corresponding to the opto-electrical path length difference (i.e. lag) seen by the reference and reflected signals. The output will be near zero unless the reflected signal round trip path is exactly the same as the reference path, at which point the output signal will go to its maximum. Thus the transmitter can be used with an analog correlator for high-resolution proximity detection. If the correlator is digital, the reference signal and the reflected signals are digitized, and these two signals are slid against each other to produce the full cross-correlation plot over all lags of interest [98]. Any arbitrary distance can be measured (as limited by the channel, but not the

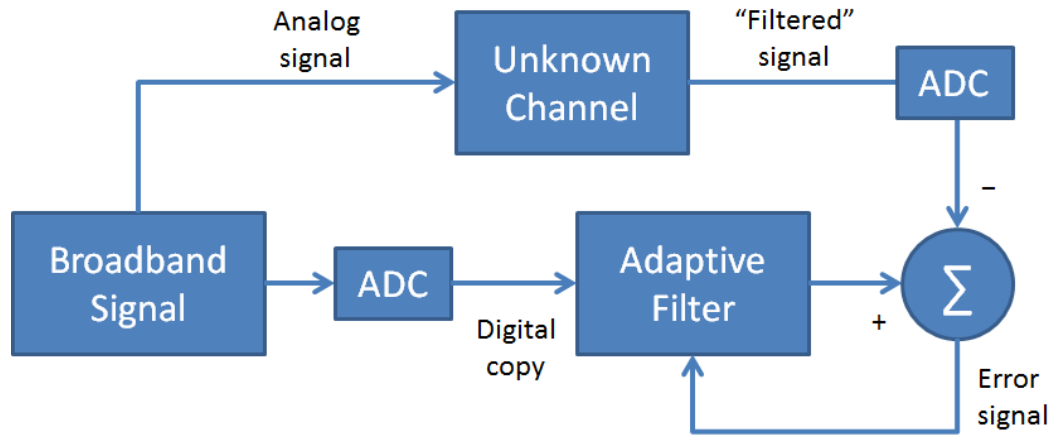


Figure 3.26: Channel Identification Concept Using Broadband Signal with an Adaptive Filter

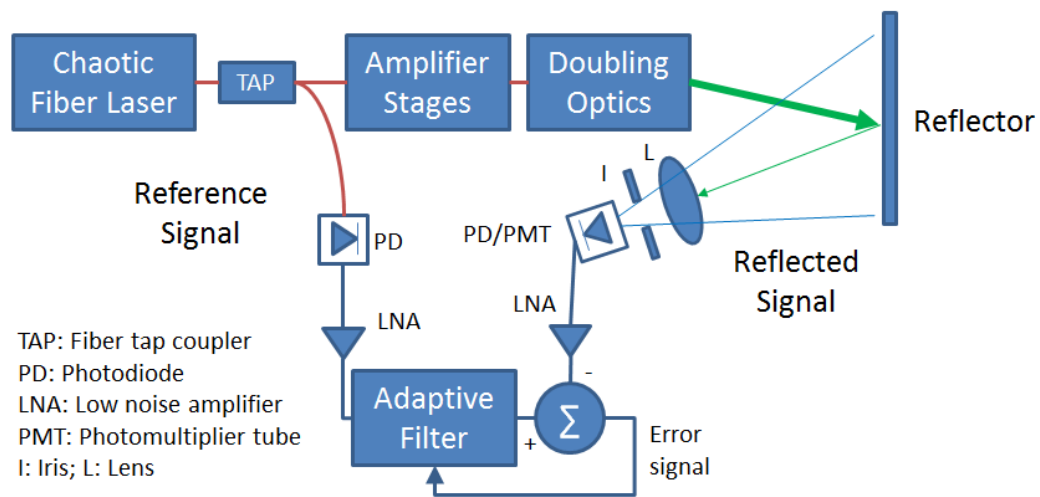
signal processing). The advantage of the analog correlator is that wideband analog components can be used, while the digital receiver's resolution is limited by the bandwidth of the digitizer.

A proof-of-concept experiment was conducted to show the effectiveness of range-finding using the chaotic transmitter and a digital receiver (see Section 4.3.1).

3.3.2 Channel Identification

A second proposed use of this wideband noiselike signal is for channel identification. Here we show that by using the signal to drive an adaptive filter, we can force the filter to match the channel, and thus identify the modulation frequency response of the channel (Figure 3.26). This is useful for determining the best operating conditions for wideband signals, since some frequency regions may be severely attenuated relative to others. White noise or a pseudo-random training signal are usually used to drive the adaptive filter and probe the channel, but the wideband noiselike properties of the chaotic laser make it well-suited for this purpose. Using the chaotic signal underwater, the modulation frequency response of the water channel can be determined as shown in Figure 3.27.

A proof-of-concept experiment was conducted to show the effectiveness of range-finding using the chaotic transmitter and a digital receiver (see Section 4.3.2).



1. Adaptive filter uses least means squared algorithm to minimize error
2. Adaptive filter becomes an estimate for the unknown channel

Figure 3.27: Underwater Modulation Response Using Chaotic Transmitter

CHAPTER 4

EXPERIMENTAL RESULTS

4.1 Transmitter Experimental Setup

4.1.1 Fiber Ring Laser

4.1.1.1 Feedback-Reflector Unidirectional Ring Laser

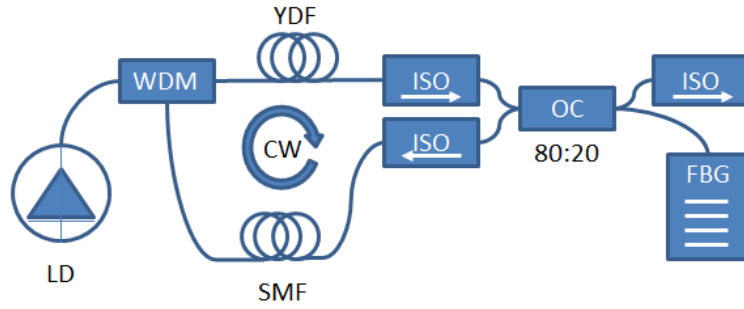
Several alternative designs were implemented before the feedback-reflector topology (see Section 4.1.1.5 below for discussion). However, no other design offered acceptable performance in terms of unidirectional flow, efficiency, wavelength control, and component flexibility, and so the feedback-reflector was selected. The laser was constructed at 1550 nm, and several modifications were made to the originally proposed design [91]:

- The saturable absorber was removed from the fiber Bragg grating (FBG) reflector branch, since multi-mode competition was to be encouraged for chaotic behavior.
- A 1 km passive fiber was added to encourage many modes to lase, making the output signal noise-like even at low pump powers, and improving the autocorrelation.
- A single isolator was used successfully in the original long (~ 15 m) cavity. When the ultralong fiber was added, two isolators proved necessary to enforce unidirectional propagation.
- An angle cleaved fiber face was used to reduce interference patterns from reflections off the fiber tip, which were seen in the frequency domain.

The final laser architecture is shown in Figure 4.1, and itemized in Table 4.1.

4.1.1.2 Lasing Threshold, Power, and Efficiency

Since two isolators were used, the gain was recalculated for both 1550 nm and 1064 nm (Figure 4.2), and the threshold estimated to be 15 mW for the 1550 nm



LD: Laser diode; WDM: Wavelength-division multiplexer;
YDF: Ytterbium-doped fiber; ISO: Isolator; OC: Output coupler;
SMF: Single-mode fiber; FBG: Fiber Braggs grating; CW: clockwise

Figure 4.1: 1550 nm Feedback Reflector Ring: As Built

Table 4.1: 1550 nm Feedback Reflector Ring: Components Used

Component	Description	Specification
Pump laser	980 nm diode	100 mW
Wave-div. mux	980/1550 nm	≤ 0.5 dB ins. loss
Er ³⁺ -doped fiber	OFS HP980	5 m
Polarization cont.	3-paddle manual	QWP/HWP/QWP
Output coupler	80:20	Bidirectional
Resonator isolators	Single-stage P	40 dB isolation
Output isolator	Single-stage	30 dB isolation
Output connector	APC/FC	8° cleave
Fiber Braggs grating	1549 nm HR	0.25 nm bandwidth
Single-mode fiber	SMF-28e	1000 m

QWP/HWP: Quarter/half wave plate; HR: High reflectivity

laser and 60 mW pump power for the 1064 nm laser.

The lasing threshold for the 1550 nm feedback reflector ring was found to be just 10 mW. From this point, the power increased at an approximate efficiency of 24%, as shown in Figure 4.3.

4.1.1.3 Temporal Output Signal

The output signal exhibits various behaviors depending on the pumping power and the polarization controller position. In general, the signal exhibits one of several behaviors: self-pulsing, periodic, and noiselike. These behaviors vary widely between the traditional "long" cavity and our novel "ultralong" cavity.

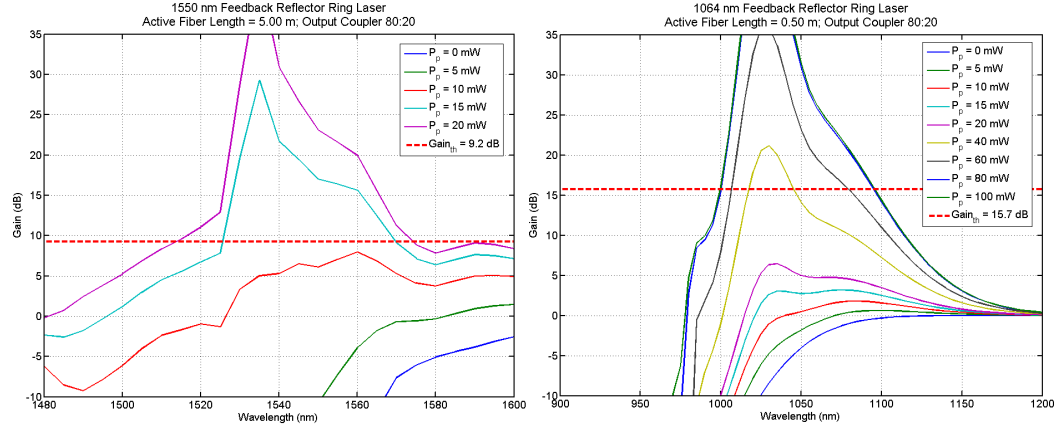


Figure 4.2: 1550 nm Feedback Reflector Ring: Gain Map for As Built Components

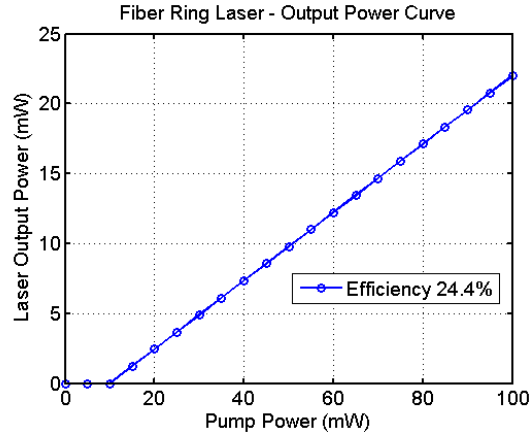


Figure 4.3: 1550 nm Feedback Reflector Ring: Power Curve

For the long cavity, the signal processes slowly from pulsing to noiselike behavior. Near the lasing threshold, self-pulsing is observed at the cavity round trip time (See Figure 4.4). As the power is increased, pulsing gives way to more complex periodic behavior. At several times threshold, the periodicity breaks down, and the waveform becomes noiselike. Through this progression, the autocorrelation becomes less periodic and more pronounced, but it does not become sharp enough to be useful for ranging (Figure 4.5). Within this basic pulsed-to-periodic-to-noise progression, adjustment of the polarization controller can bring the two polarizations in and out of phase, creating another interference pattern between the polarizations (see Figure 4.6).

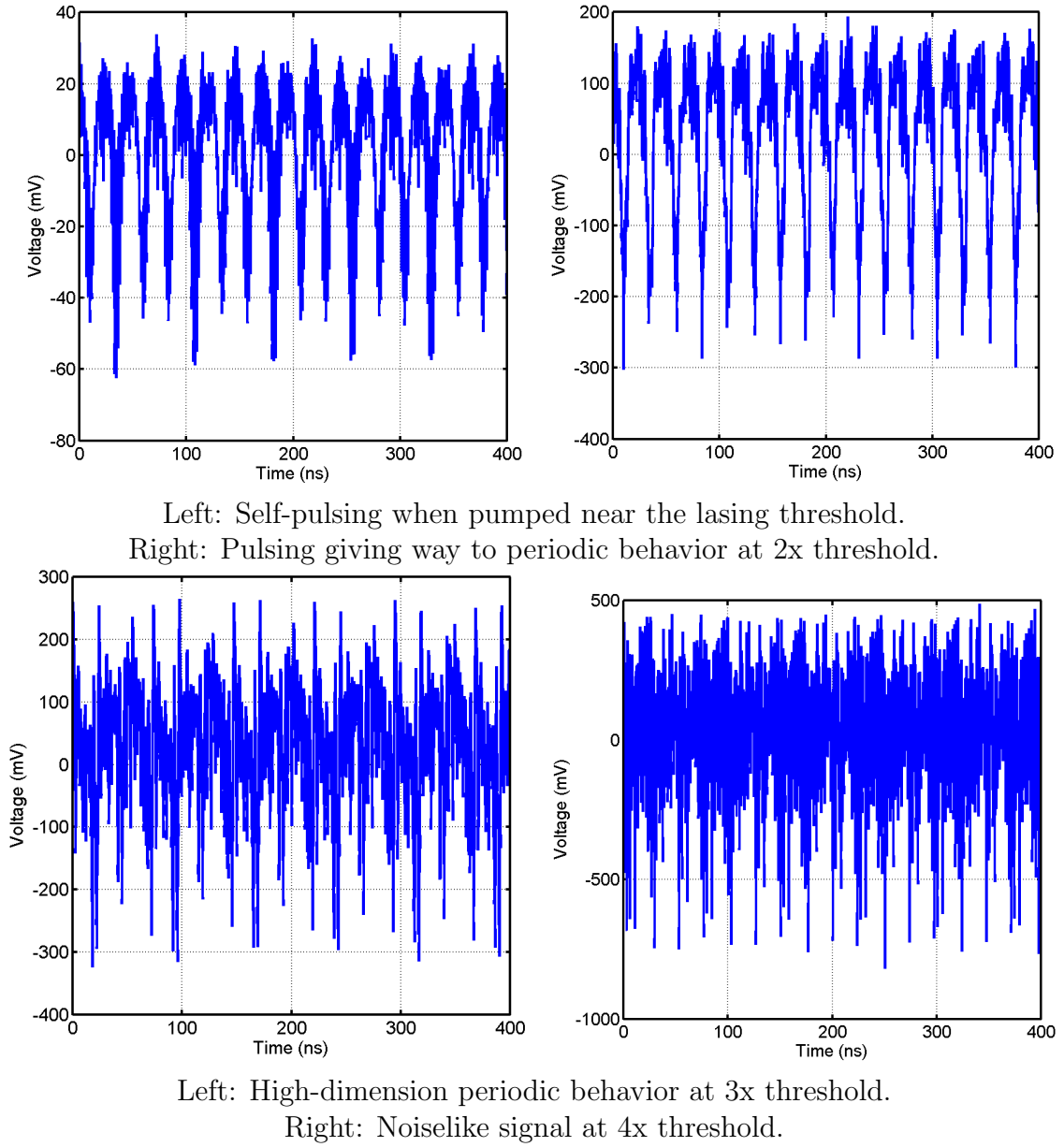


Figure 4.4: Progression in total output signal behavior with increasing pump power (Long cavity)

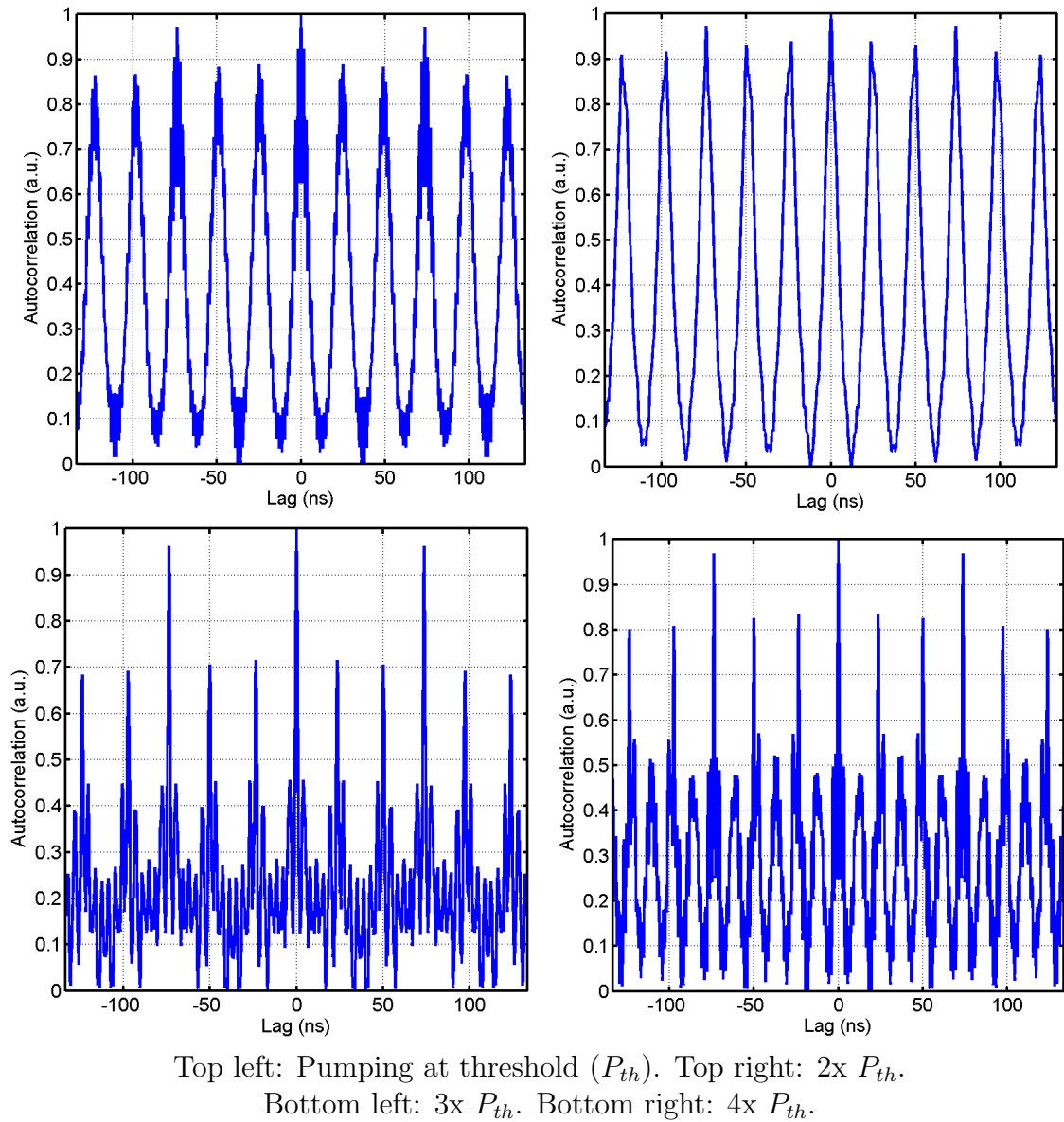
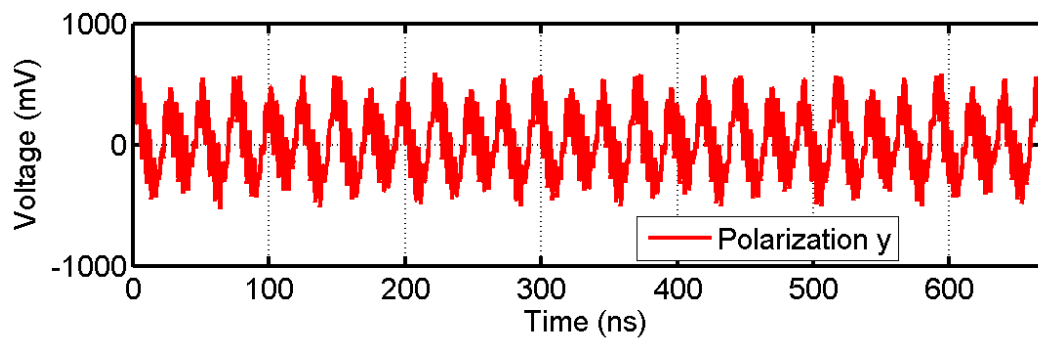
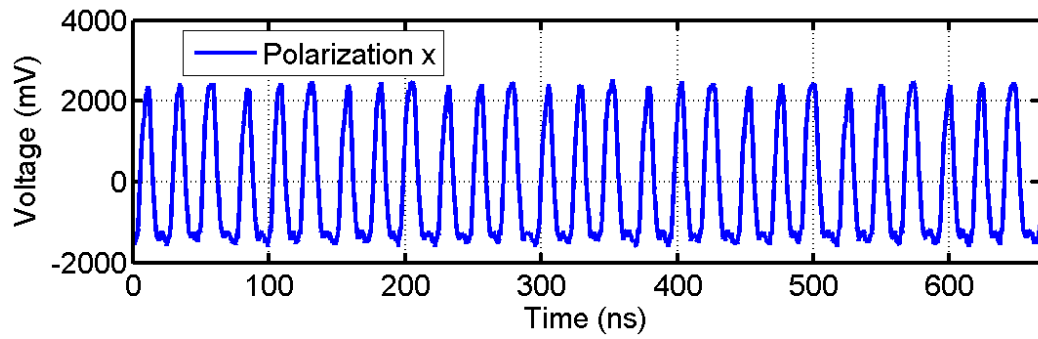
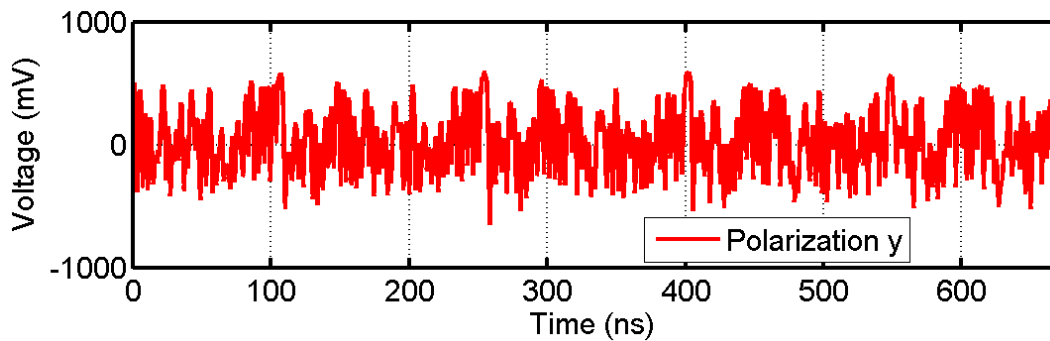
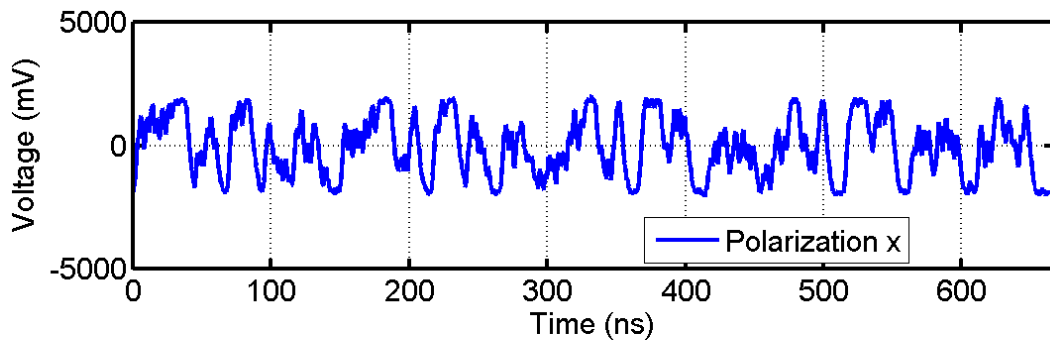


Figure 4.5: Change in autocorrelation of total output signal with increasing pump power (Long cavity)

In the ultralong cavity, the huge increase in number of modes leads to stronger constructive and destructive interference patterns between modes. The pulsed-periodic-chaotic progression is highly accelerated, such that the signal becomes noiselike even at low pump powers (as in Figure 4.7). As the signal becomes chaotic and noiselike, the autocorrelation is dramatically sharpened, and it goes to a near-ideal thumbtack at increasing pump powers (Figure 4.8). While the polarization controller does affect



Pulsing and periodic behaviors appear simultaneously in different polarizations.

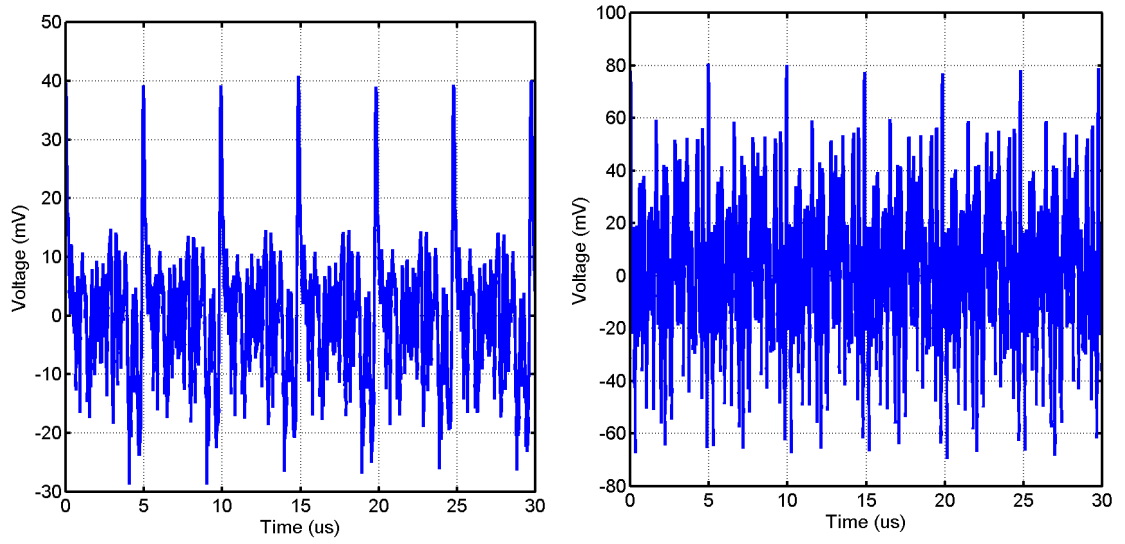


Periodic and noiselike behaviors appear simultaneously in different polarizations.

Figure 4.6: Simultaneous polarization traces showing different behaviors (Long cavity)

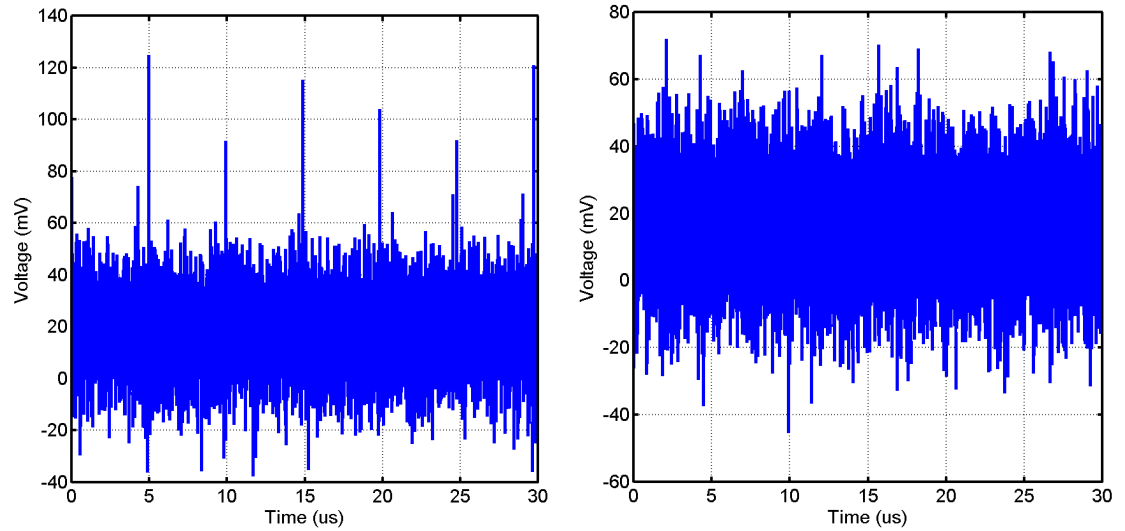
the signal, most behaviors are strongly noiselike regardless of polarization controller (Figure 4.9).

This progression from pulsed to periodic to chaotic behaviors can be intuitively thought of in terms of mode competition. When the pump power is low, the first mode to lase dominates the others, and becomes a strong feedback to the cavity. Feedback of a single tone is a perfect way to actively mode-lock a laser, and so it is not surprising that pulsing results. As the pump power increases, more gain is available, and other modes can lase even while the first mode is lasing strongly. These modes may well be out of phase with the first mode; if this is the case, then a periodic interference pattern is formed between sets of phase-locked modes (each lasing mode will attempt to phase-lock some adjacent modes, so several phase-coherent sets may emerge). Increasing the pump power further, the system gain becomes too high to be dominated by just a few modes. Many modes lase strongly, and they all provide feedback to the cavity; the result is that the modes compete for gain in a chaotic cycle of each mode giving and taking gain from its neighbors. Thus the modes are chaotically coupled through the finite cavity gain. This effect is most strongly seen in an ultralong-cavity laser, where there are many modes to balance and compete with each other (for comparison, see Figure 4.10). For the chaotic ranging application, chaotic mode competition should be encouraged by an ultralong cavity and high pump powers.



Left: Self-pulsing when pumped near the lasing threshold.

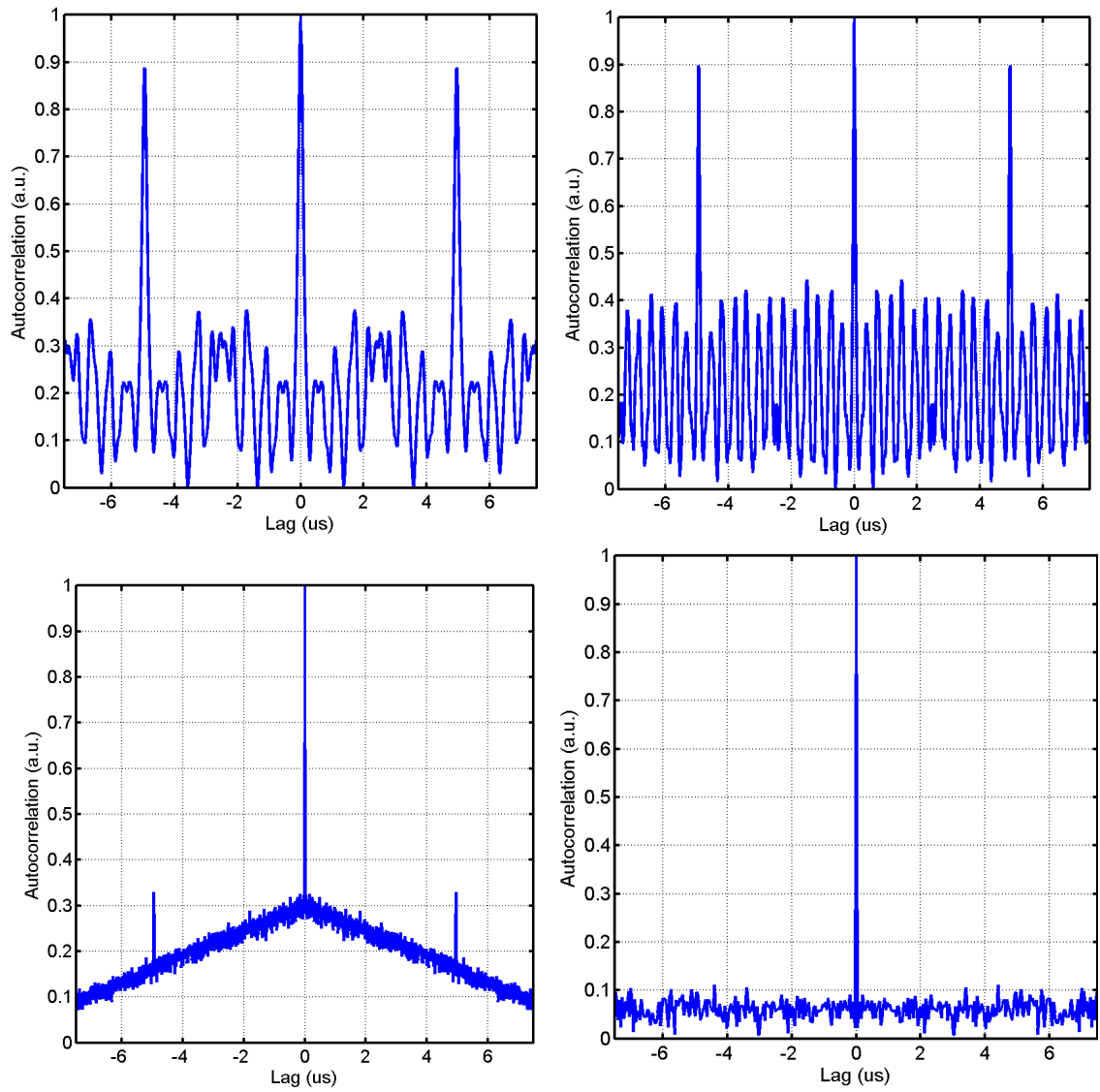
Right: Pulsing giving way to periodic behavior at 1.5x threshold.



Left: Becoming noiselike at 2.5x threshold.

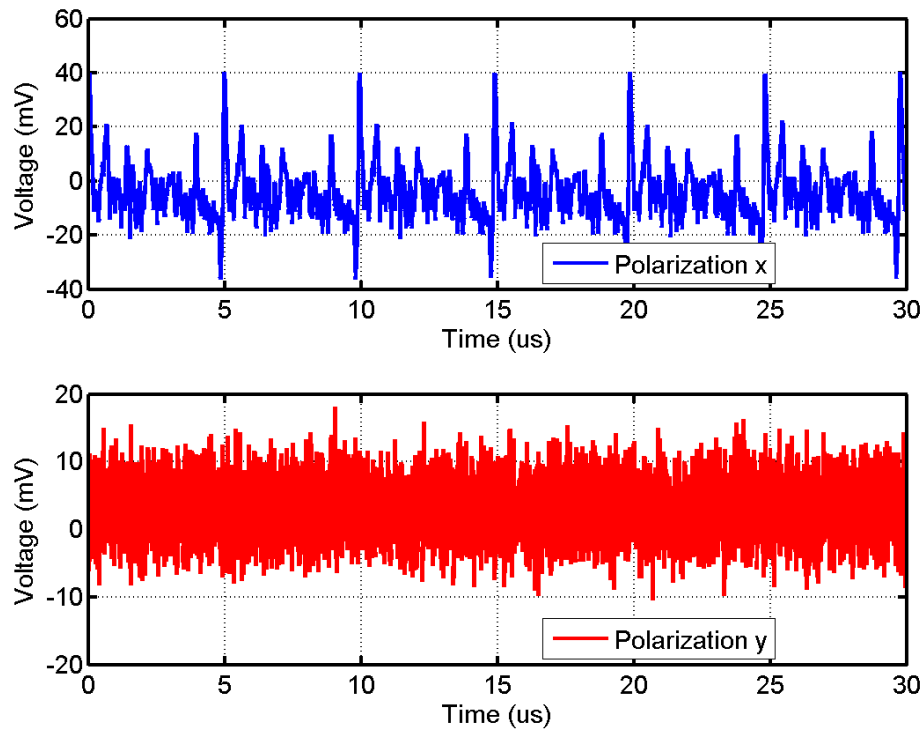
Right: Noiselike signal at 4x threshold.

Figure 4.7: Progression in total output signal behavior with increasing pump power (Ultralong cavity)

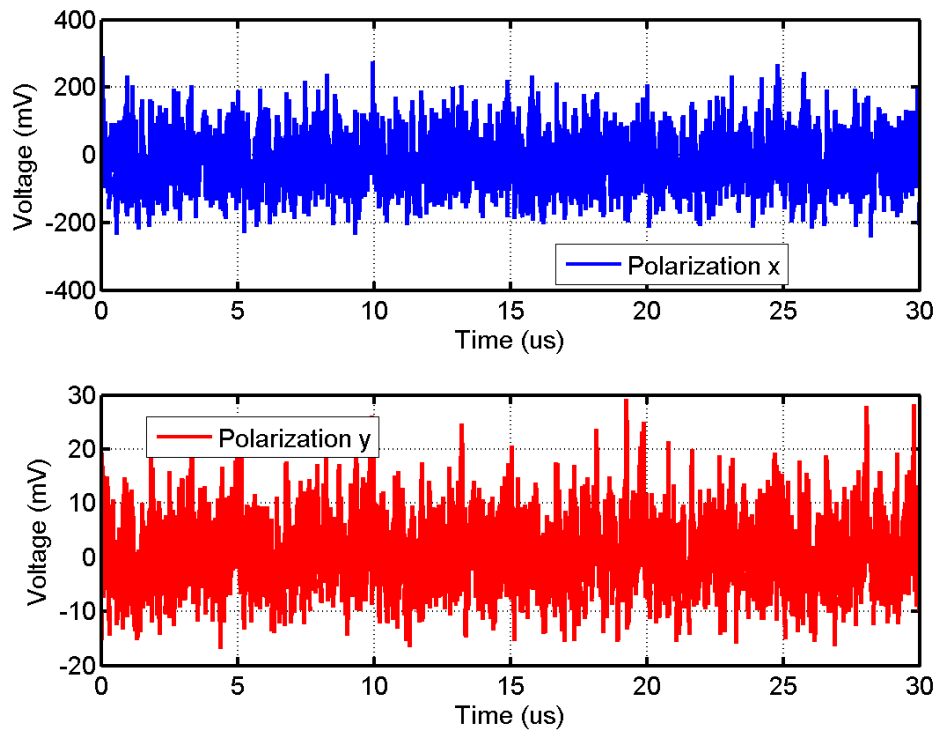


Top left: Pumping at threshold (P_{th}). Top right: $1.5x P_{th}$.
 Bottom left: $2.5x P_{th}$. Bottom right: $4x P_{th}$.

Figure 4.8: Change in autocorrelation of total output signal with increasing pump power (Ultralong cavity)



Periodic and noiselike behaviors can appear simultaneously in different polarizations when pumped near threshold.



At $1.5 \times P_{th}$ and above, polarization-resolved waveforms are noiselike regardless of polarization.

Figure 4.9: Simultaneous polarization traces showing chaotic behavior, except near threshold (Ultralong cavity)

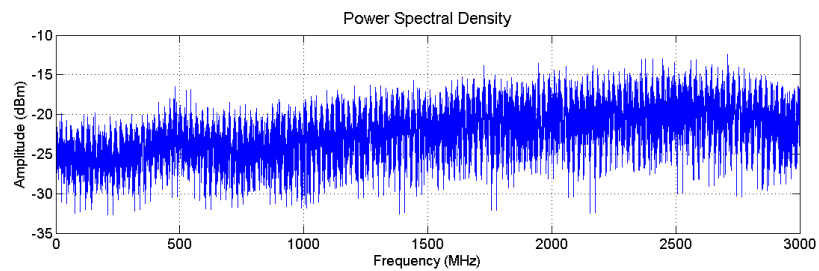
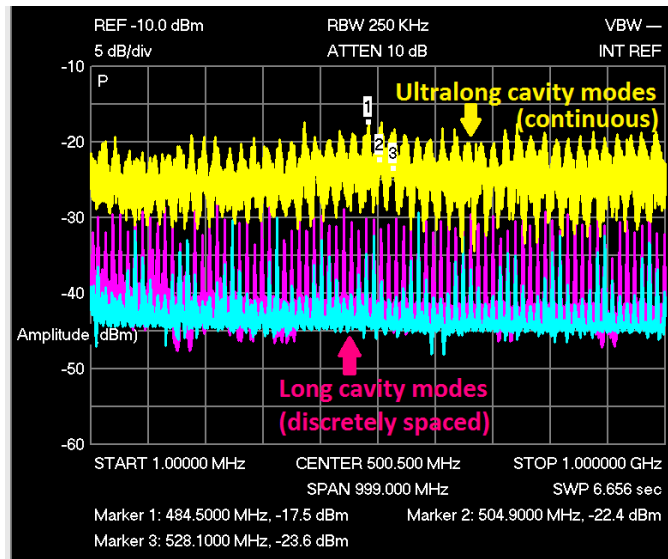
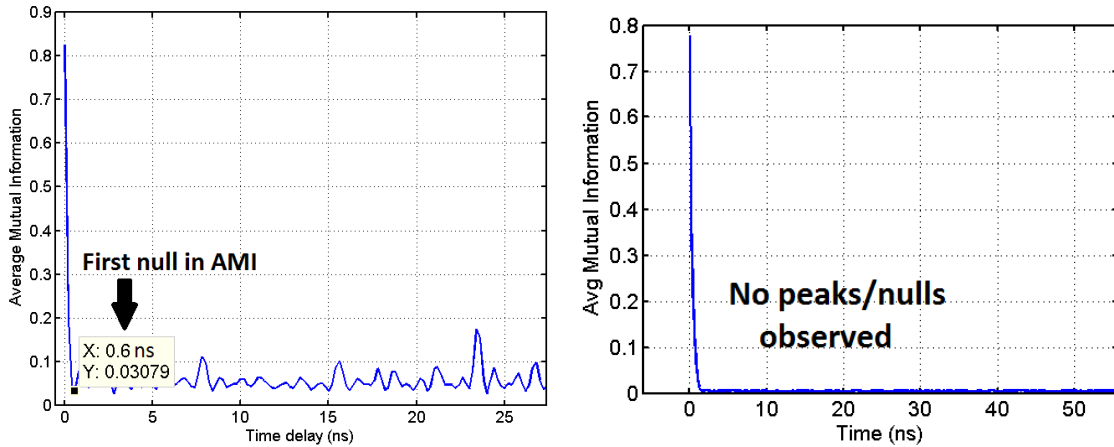


Figure 4.10: Comparison of frequency-domain content between long and ultralong cavities. Top: The long cavity's discrete modes are shown in magenta; the ultralong cavity's quasi-continuous spectrum is overlaid in yellow. Bottom: DC-3 GHz uniform, near-flat spectrum of ultralong cavity laser.



Left: Avg mutual information (AMI), long cavity laser. Right: AMI, ultralong cavity.

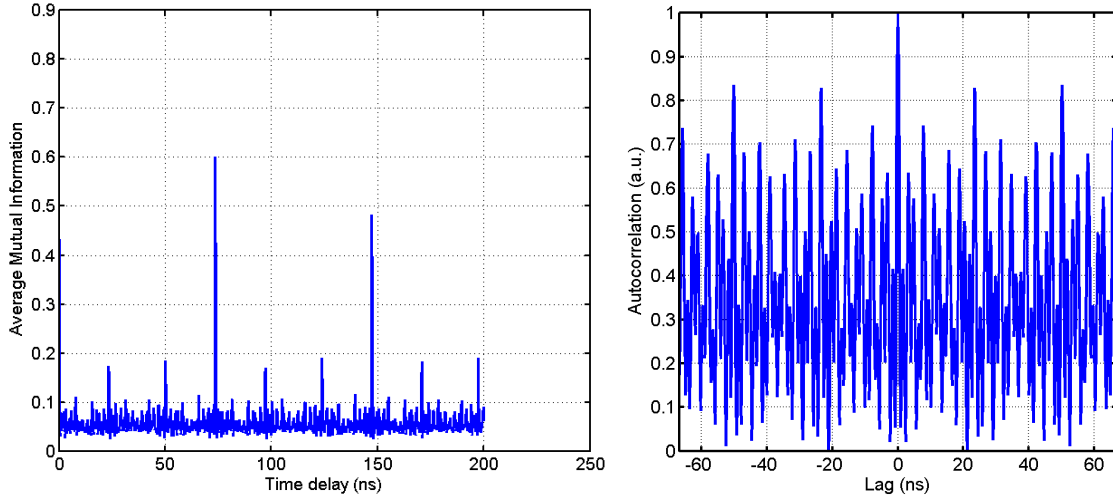
Figure 4.11: Average mutual information in long and ultralong cavity laser

4.1.1.4 Analysis of Chaotic Behavior

Analysis of the chaotic behavior of the ultralong fiber laser was performed in the following steps.

1. Calculate average mutual information (AMI) in signal (AMI is a sort of non-linear autocorrelation)
2. Select proper embedding delay
3. Make 2-D and 3-D phase plots using this delay; look for deterministic periodic nonlinear structures

The AMI was calculated for both the long- and ultralong-cavity lasers (Figure 4.11). The AMI for the long-cavity laser indicated that there some periodicity to the signal, although interestingly the AMI does a better job than the linear autocorrelation at discriminating between the signal and time-delayed copies of itself (Figure 4.12). The ultralong-cavity laser AMI shows increasingly little periodicity in the time series, and no clear attractor structure (not shown) which probably indicates that the sampling speed was too low to resolve the structure of the chaos. However, analysis on the long-cavity time series was performed.



Left: Avg mutual information, long cavity laser, multiple round trips. Right: Autocorrelation, long cavity.

Figure 4.12: Average mutual information versus autocorrelation as a means of uniquely identifying the quasi-periodic chaotic signal

As a first-order estimate, the embedding delay is usually taken to be the lag corresponding to the first null in the AMI delay plot. For the long-cavity, the embedding delay is estimated at 0.6 ns as indicated in Figure 4.11. A phase plot is then made of the laser output intensity time series versus a delayed version of the same time series (Figure 4.13). Several other embedding delays are also used for this phase plot, as a check on the selected delay: a delay that is too small will lead to a nearly linear phase plot, indicating the data points are too closely correlated to be interesting; a delay that is too large will lead to structureless plots that also give no information. In this case it appears the delay is well selected, since an interesting and clear structure does emerge. Meanwhile, the 0.2 ns delay plot seems too linear, and its structure very simple compared to the 0.6 ns phase plot. The higher delay values lead to increasingly complex structures, which may be starting to devolve into uncorrelated scatter as the delay gets too large. Forming a three-dimensional phase plot using the same 0.6 ns delay, a clear attractor pattern is seen (Figure 4.14).

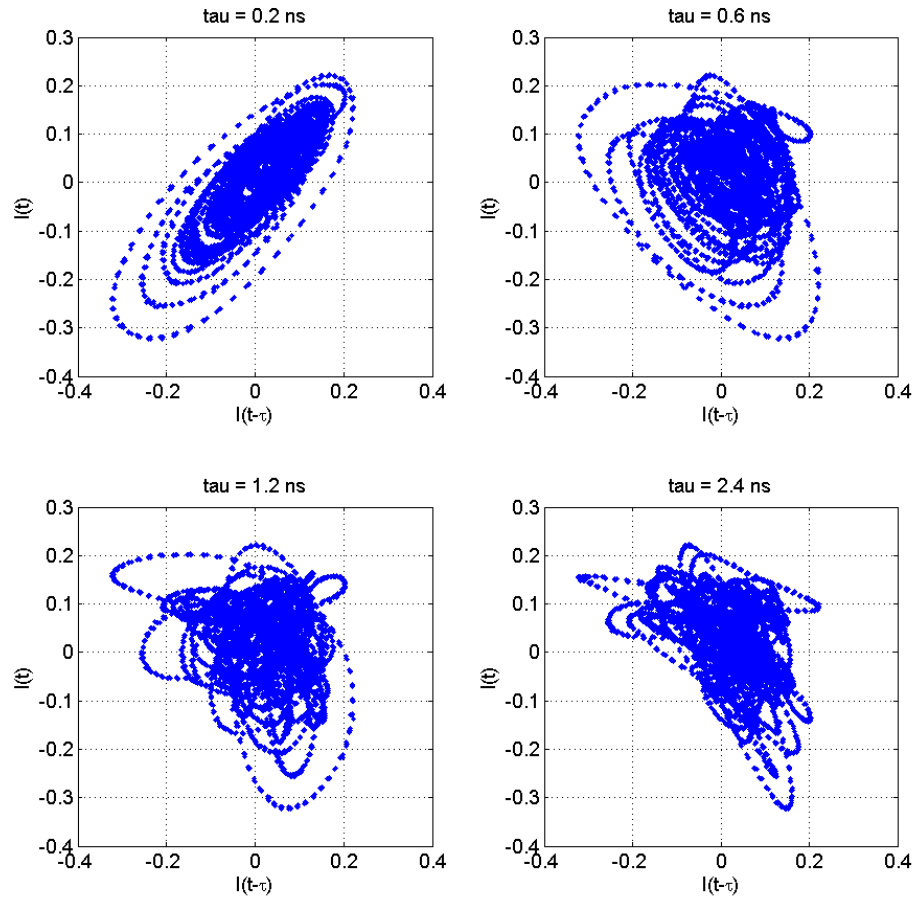


Figure 4.13: 2D phase plots for laser output intensity timeseries, for various embedding delays

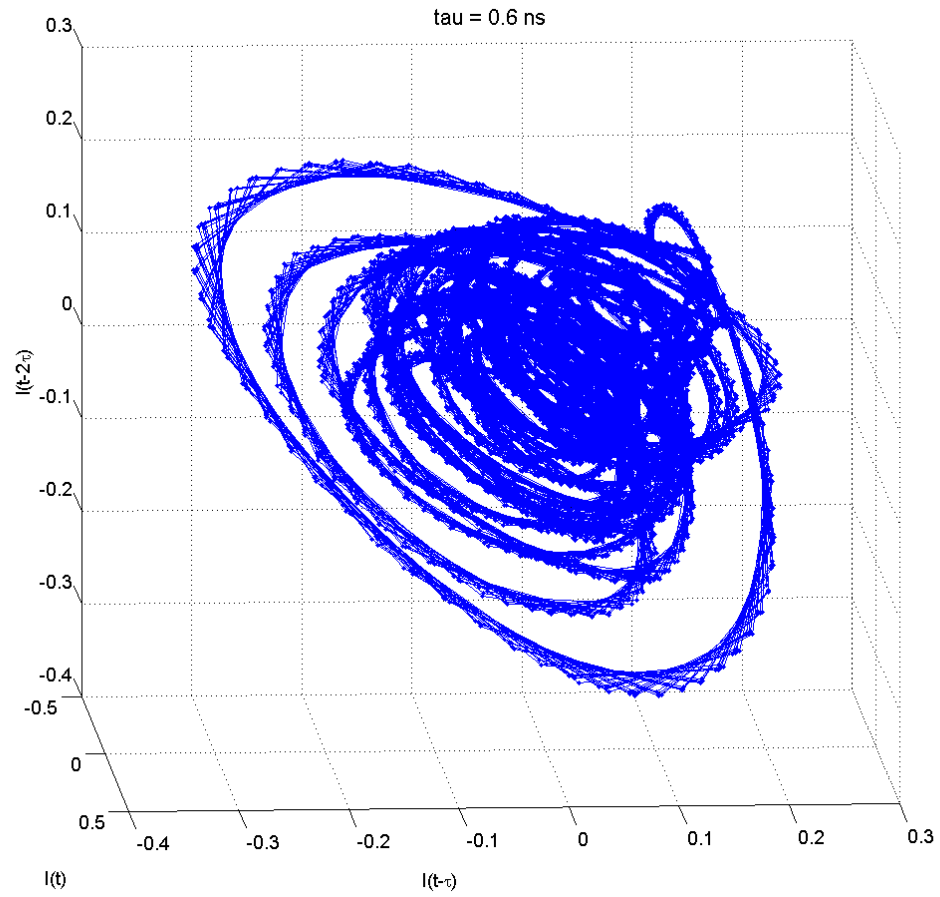


Figure 4.14: 3D phase plot for laser output intensity timeseries, showing chaotic attractor structure ($\tau = 0.6$ ns)

4.1.1.5 Implementation of Alternative Designs

Circulator-Based Unidirectional Ring Laser Initial chaotic laser designs used a circulator to create a reflective FBG branch in the resonator ring [16, 17]. This worked well at 1550 nm, and led to moderate output powers on the order of 10 mW with a 100 mW pump. However, when a 1064 nm ring was constructed, the additional cavity loss of the less efficient circulator led to unacceptably low output powers. In one test, before the circulator was inserted, a 1064 nm fiber ring laser with a 280 mW pump produced ~ 35 mW output power. Adding the circulator's 4-5 dB of cavity loss, the power dropped to 3.5 mW. This power was so low that it failed to properly drive the preamplifier: the preamplifier cleanly boosted the signal to ~ 25 mW output, but beyond that all additional output power was undesired ASE. This 25 mW was in turn insufficient to drive the gain amplifier, and so the circulator-based design was scrapped in favor of the Fabry-Perot, whose efficiency was far better.

Bidirectional Ring and Fabry-Perot Lasers The Fabry-Perot laser used two matched FBGs to create a wavelength-selective resonator cavity. First single- and then dual-side pumping were used through the FBGs. An 80:20 coupler inside the cavity provided output since the FBGs were $>99\%$ reflective at 1064 nm. This design proved to be reasonably efficient, yielding output powers of 70 mW when 280 mW pump power was launched, which was more than sufficient to drive the preamplifier. However, inspection of the temporal output signal showed that while the cavity modes did appear at the correct frequency spacing, their amplitudes varied wildly, with a strong polarization-dependence to the mode structure (Figure 4.15). Moreover, a pronounced long-time-scale interference pattern was observed at the output, with a sort of extreme amplitude modulation imposed on the desired chaotic waveform. This non-stationarity made the signal both impossible to characterize and difficult to use; of particular concern was the implication of trying to achieve long-distance ranging with a signal of unpredictable amplitude. Experiment and analysis indicated that the main cause of this unwanted interference was the coherent summation of the bidirectional waves at the output coupler. The counter-

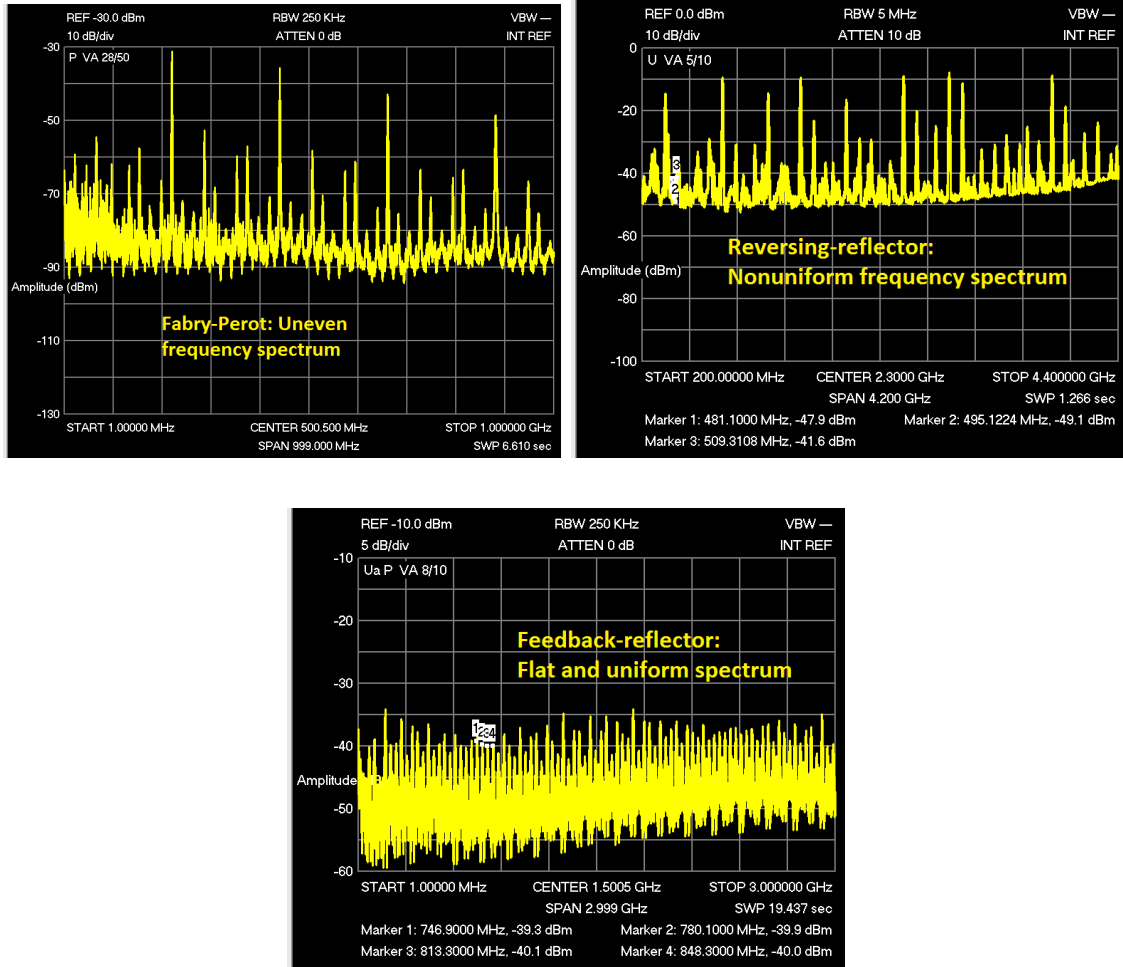


Figure 4.15: Frequency spectra for several fiber ring laser designs. Top left: Fabry-Perot laser output. Top right: Reversing reflector laser output. Bottom: Feedback reflector laser output. The power spectral density is near-flat and uniform, as desired.

propagating polarization modes were being added up and were creating constructive and destructive interference patterns that swamped the desired output. Thus a unidirectional configuration was sought, and the Fabry-Perot configuration discarded.

The reversing-reflector design was expected to be the most efficient unidirectional traveling-wave configuration [90]. However, it suffered from a tenuous trade-off between wavelength control and unidirectional flow that precluded any component flexibility. It was found that using an 80:20 output coupler, unidirectional propagation was enforced, but the wavelength was not properly controlled by the FBG.

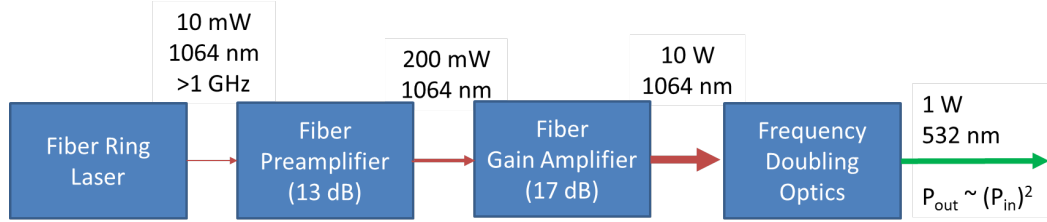


Figure 4.16: Chaotic Transmitter Block Diagram

The feedback from the FBG was insufficient to discriminate against the 1535 nm free-running lasing wavelength. On the other hand, a 97:3 coupler provided proper wavelength control at 1549 nm (the wavelength of the FBG), but unidirectional propagation was not observed. The strength of the counter-clockwise (ccw) beam was about 19 dB higher than the clockwise (cw) path, but this proved insufficient suppression, since strong interference patterns were observed at the output coupler. Insertion of a 40 dB isolator provided fully unidirectional flow, but since the FBG is only in the cw path, the wavelength control was now eliminated. While the original researcher used a 90:10 coupler, which may have provided the correct trade-off between the wavelength control and the interference, the balance was judged to be too tenuous to be relied on without detailed numerical simulation. Additionally, the addition of an ultra-long passive fiber in this laser was expected to cause additional counter-propagating scattering effects, and so we wanted the ability to use an isolator to counteract these if necessary. Thus the reversing-reflector topology was shelved in favor of the feedback-reflector, which both allowed use of an isolator as necessary, and could be used at various coupler ratios.

4.1.2 Fiber Amplifiers

The implemented amplifier chain included a core-pumped, forward-pumped preamplifier, to boost the seed power and compensate for insertion losses, and a cladding-pumped, forward-pumped gain amplifier, to develop sufficient power for frequency doubling (shown in Figure 4.16). The components used for the preamplifier and gain amplifier are given in Tables 4.2 and 4.3, respectively.

Table 4.2: 1064 nm Premplifier: Components Used

Component	Description	Specification
Pump laser	980 nm SM diode	280 mW
Wave-div. mux	980/1064 nm	≤ 0.5 dB IL
Yb ³⁺ -doped fiber	6/125 μ m DC	30 cm
Tap coupler	99:1	≥ 50 dB RL
Output isolator	Single-stage	30 dB iso

All fiber used was HI-1060 single-mode.

SM: Single-mode; RL: Return loss; IL: Insertion loss; DC: Double-clad

Table 4.3: 1064 nm Gain Amplifier: Components Used

Component	Description	Specification
Pump lasers	915 nm MM diode	3 at 8 W each
Pump-signal combiner	SC input/DC output	10 μ m/105 μ m
Yb ³⁺ -doped fiber	10/105/125 μ m DC	4 m
Output isolator	Fiber-to-free space	≥ 50 dB RL

MM: Multi-mode; SC: Single-clad; DC: Double-clad; RL: Return loss

4.1.2.1 Two-Stage Core/Cladding Pumped Amplifier Chain

The preamplifier boosted the fiber laser seed signal from ~ 70 mW to above 150 mW, for a nominal pump conversion efficiency of 37% (the actual fiber efficiency is somewhat higher since the pump sees the insertion loss of the WDM and two splices on its way to the fiber). This level was sufficient to drive the gain amplifier, which produced 5.5 W of infrared output power when driven with 12.5 W of launched pump power.

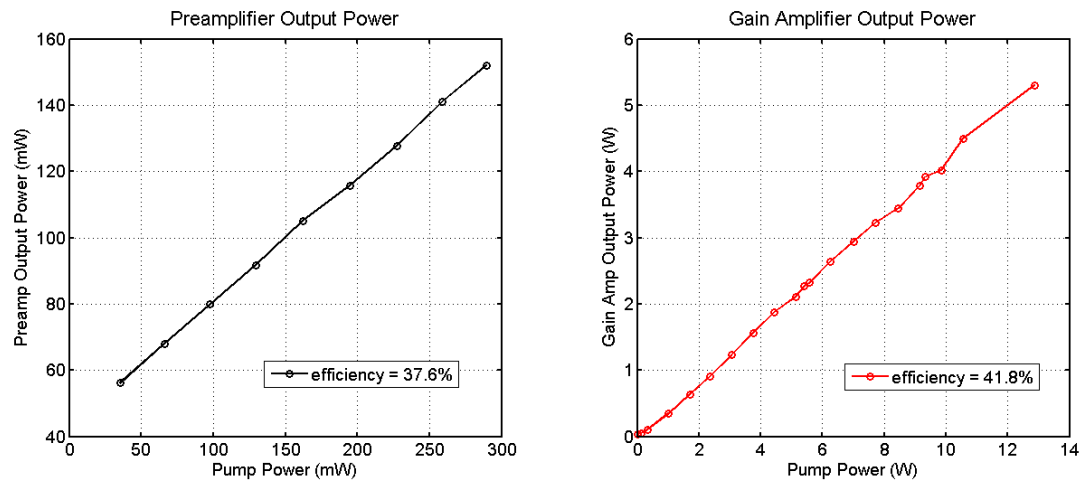
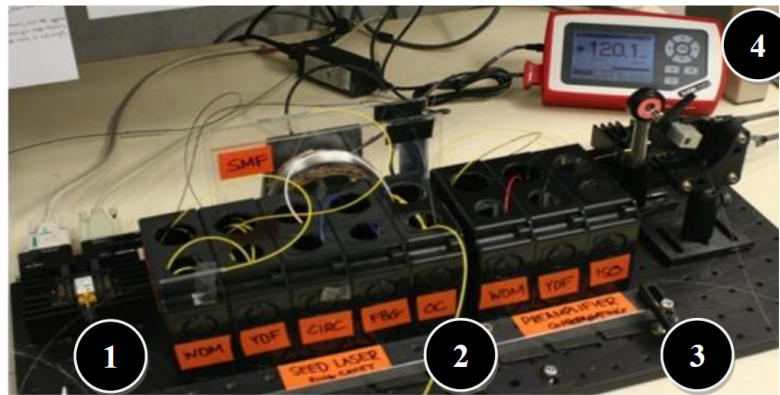


Figure 4.17: Amplifier Power Output Versus Launched Pump Power

Seed and Pre-amplifier:

1. Pump diode
2. Seed laser including 100 m SMF
3. Pre-amplifier including output isolator
4. Metering for output power



Gain Amplifier:

1. Power supplies
2. Pump diodes and cooling
3. Fiber pump/signal combiner
4. Active ytterbium doped fiber
5. Metering for temperature, back reflection, and output power

Figure 4.18: Preamplifier and Amplifier Experimental Setups

4.1.2.2 Amplified Spontaneous Emission and Amplifier Limits

The preamplifier was initially used to amplify a 3.5 mW seed signal from a circulator-based fiber ring laser. When this was attempted, 25 mW of seed signal was developed, but further increasing the preamplifier pump power only led to ASE. Thus the preamplifier was ASE-limited when large gains were required (the amplifier was likely operating at about 10 dB gain, considering the insertion losses seen by the input signal). The preamplifier did not seem to be saturated at its maximum output power; that is, its performance was limited not by a quantum defect or a maximum system gain, but by the amplifier's conversion efficiency.

No ASE-limiting cases were observed in the gain amplifier. No saturation or non-linear gain regions were seen either; the amplifier output seemed to be a linear function of the power and was determined by the overall conversion efficiency. Thus as with the preamplifier, more pump power would increase the output power linearly, and any improvement in the efficiency would increase the output power even if the same pumps were used.

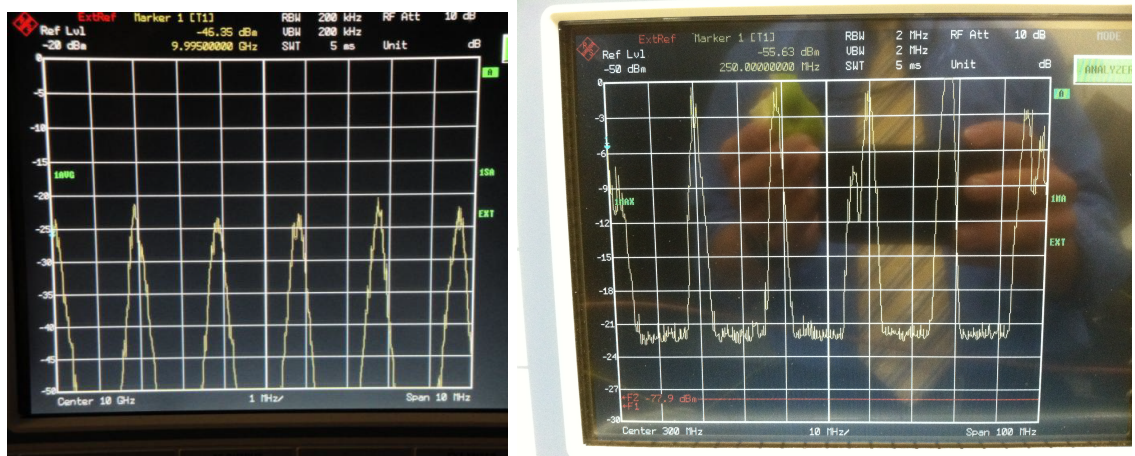
4.1.2.3 Modulated Signal Amplification Dynamics

The high-frequency, wideband seed signal was faithfully transmitted by the amplifier. The power spectral density of the high power signal at the output of the gain amplifier was the same as that produced by the seed laser. (See Figure 4.19.)

4.1.3 Frequency Doubler

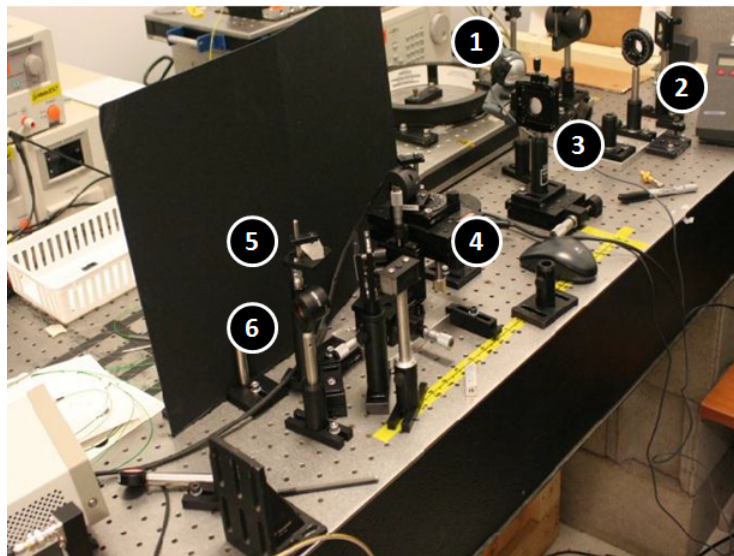
4.1.3.1 Free Space Optical SHG Setup

A series of free space optical components were used to focus the infrared beam through the crystal, and then to separate and collimate the green light for transmission. The free-space optical setup used is shown in Figure 4.20, and includes: a telescope for controlling beam width; a half-wave plate for controlling polarization orientation; a focusing lens for focusing the beam into the crystal; the nonlinear crystal with a temperature controller; a focusing lens to collimate the output; a Pellin-Broca prism to separate the residual infrared from the green; and a KG3 near-IR filter to completely eliminate infrared prior to transmission.



Left: Low power signal from seed laser. Right: High power signal out of gain amplifier.

Figure 4.19: Intensity Modulation Transmitted by Amplifier



Frequency Doubler:

1. Beam expander
2. Half-waveplate
3. Focusing lens
4. Nonlinear crystal
5. Pellin-Broca prism
6. Collimating lens

Figure 4.20: Frequency Doubling Optical Setup

4.1.3.2 Efficiency and Output Power

The crystal produced green light at a quadratic rate relative to the input infrared light. Projecting along this quadratic curve, satisfactory output power nearing 1 W are expected from attainable infrared powers (Figure 4.22).

The frequency doubling did not seem to systematically affect the intensity modulation of the signal (see Figure 4.23). This is to be expected, since the intensity modulation is a “slow-time” phenomenon relative to the crystal’s optical wavelength

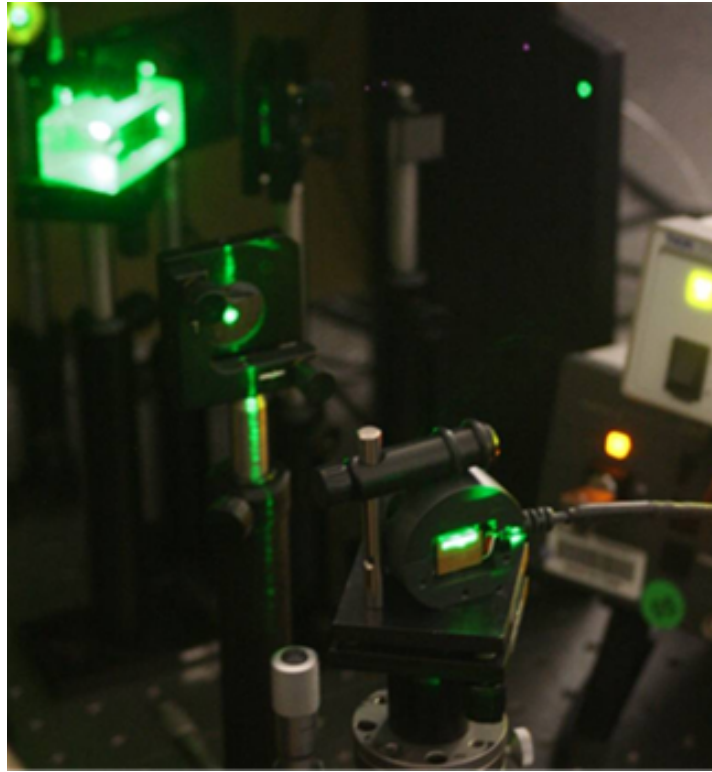


Figure 4.21: Frequency Doubling Crystal: Green output signal from infrared input

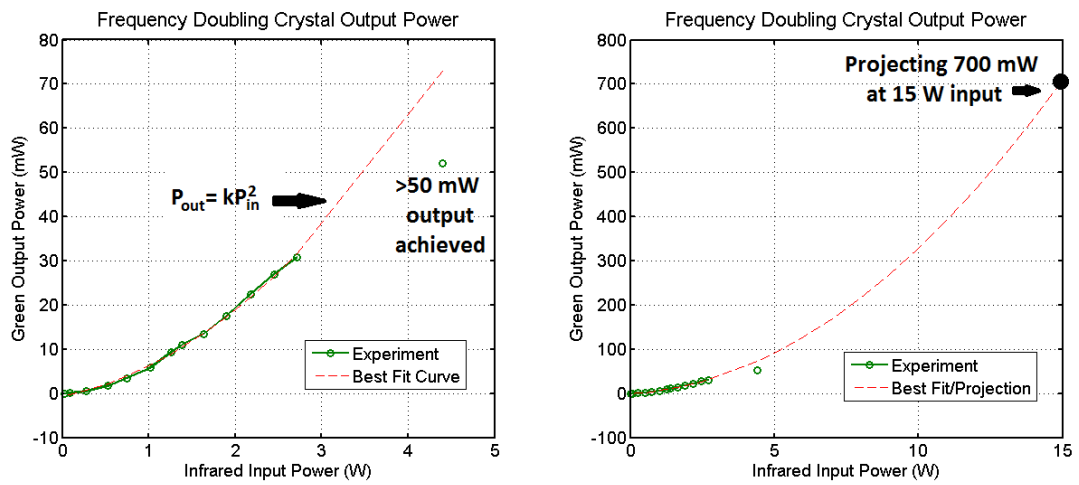


Figure 4.22: Green output power versus infrared input power. Left: Low power conversion achieved. Right: High power conversion projected.

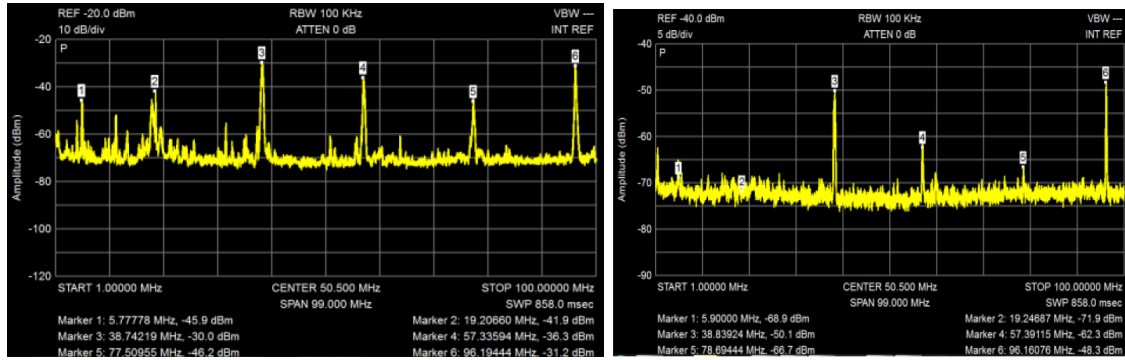


Figure 4.23: The frequency spectrum transmitted by the SHG crystal. Left: Infrared PSD at 1064 nm. Right: Green spectrum at 532 nm.

conversion speed.

4.1.3.3 Beam Shaping and Power Density

Beam shaping was found to be critical to success. The best results were obtained from a large beam (15 mm beamwaist) and a long focusing lens (300 mm). This was found to put $>90\%$ of the power into a $400\text{ }\mu\text{m}$ pinhole over a 20 mm depth; in other words, the beam shape was such that the entire beam was contained within the crystal. At the center of the crystal, $>80\%$ of the power passed through a $150\text{ }\mu\text{m}$ pinhole, indicating that the power density was very high in the volumetric center of the crystal. This corresponded to a Rayleigh range of about 10 mm, in accordance with the manufacturer's recommendations.

It should be noted that the conversion results shown in Figure 4.25 were obtained with a different beamshape, whose Rayleigh range was significantly longer than recommended.

4.2 Transmitter Experimental Results

4.2.1 Chaotic Fiber Laser Transmitter Setup

The final transmitter setup is shown in Figure 4.24. End-to-end performance is shown in Figure 4.25.

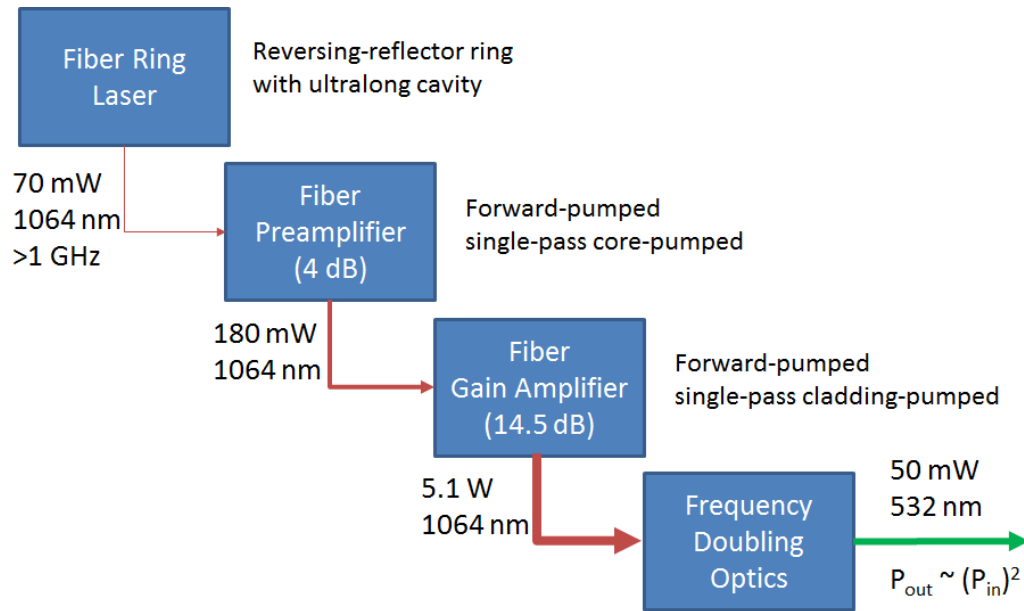


Figure 4.25: Final Transmitter Performance As Built

- The laser losses are likely higher than estimated.

At the pump input to the WDM, 0.5 dB was estimated for mode mismatch and insertion loss.

In the cavity, attenuation losses were not included in calculations, and splice losses may have been underestimated at 1 dB total.

At the output, an isolator and a cleaved connector were both spliced on during measurement. These were estimated at 0.5 dB total.

Increasing the estimated input loss by 1.5 dB, the cavity loss by 2 dB, and the output loss by 1 dB, brings the estimated efficiency down to 24%. Investigation is necessary into the true losses seen.

- The preamplifier may suffer from excessive signal propagating in the cladding.

This could occur with bad splices, or with a long uncoiled fiber run.

Coiling may be useful for eliminating cladding modes prior to amplification.

The slight mode mismatch between the passive WDM pigtail and the active doped fiber may make it more likely that light could leak to the cladding.

Simulations indicate that mode overlaps on the order of 0.6 (rather than the 0.95 estimate used in the initial simulations) would account for the inefficiency seen.

- The infrared-to-green conversion efficiency is likely a combination of several factors.

The infrared signal is not linearly polarized. Since the crystal operates only on a single polarization, the infrared power on the other polarization is wasted. A polarization controller can be added to enforce linear polarization.

Different beam shapes should be explored. Preliminary experiments using a 10 cm Rayleigh range were more successful, and can be returned to.

Increased infrared beam strength will improve the performance of the crystal. Linear improvements to the amplifier efficiency will impact the final output quadratically.

The single-pass efficiency of the crystal will be relatively low ($\leq 10\%$) even for corrected polarization, optimal beam shape, and beam powers above 10 W. However, dramatically higher efficiencies ($\leq 85\%$) have been reported by placing a resonator around the nonlinear crystal [11]. Such a multi-pass approach could reduce infrared power requirements by an order of magnitude while producing hundreds of mW of green light.

Notwithstanding the clear opportunities for improvement, the 50 mW signal output obtained is sufficient to run several system experiments on the applications of interest.

4.3 Application Proof-of-Concept Experiments

4.3.1 High Resolution Ranging by Correlation

A proof-of-concept ranging experiment demonstrates how the new chaotic laser can be used for high resolution rangefinding. Using a 5 GSPS digitizer with 500 MHz

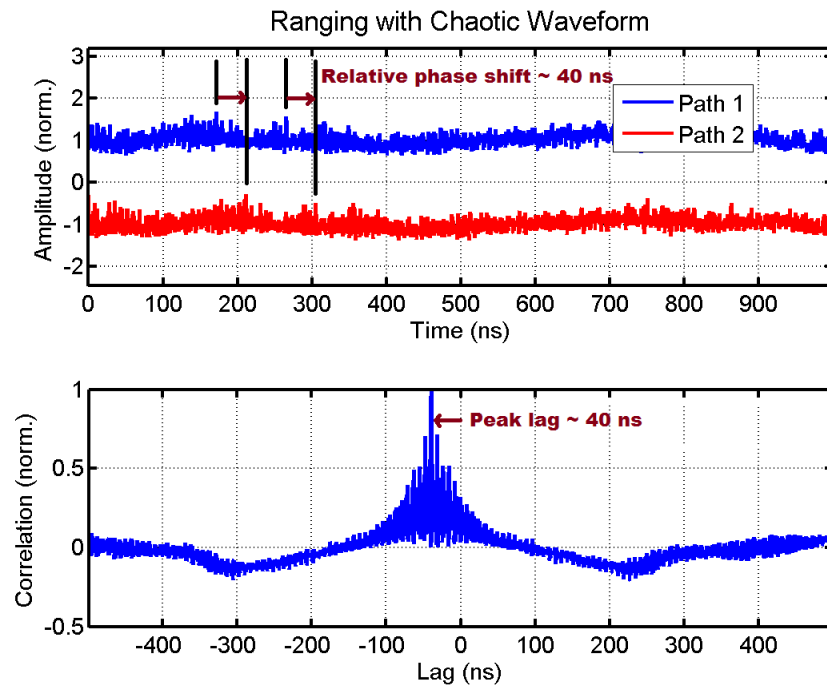


Figure 4.26: Digital Correlation of Phase-shifted Waveforms for Ranging

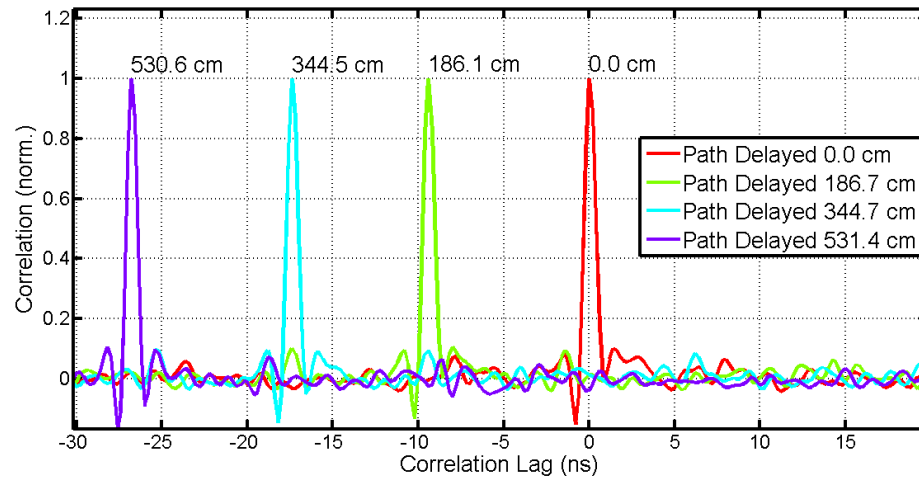


Figure 4.27: Ranging Proof-of-concept Using Digital Receiver

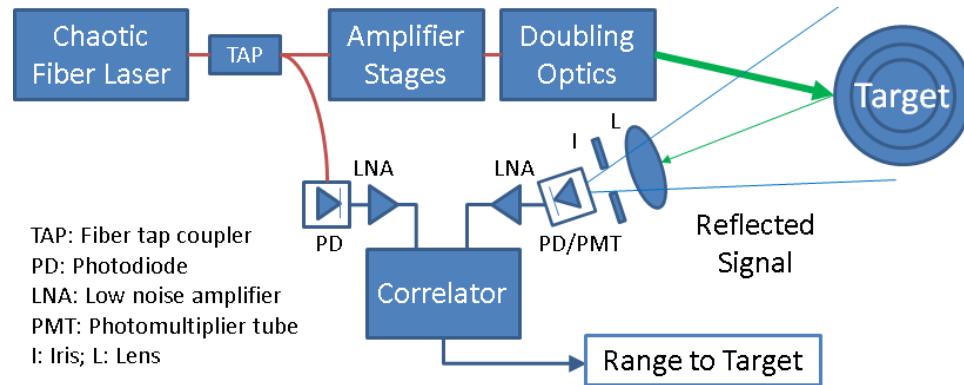


Figure 4.28: General Transceiver Setup for Ranging and Imaging

analog bandwidth, the laser signal was reflected off a target, and the target return was correlated against the transmitted signal (an example of digital correlation of two phase-shifted signals is shown in Figure 4.26). The lag of this correlation showed the round trip distance to the target. As the relative path distance to the reflector was changed, the lag of the correlation peak likewise changed. As shown in Figure 4.27, the results show digitizer-limited accuracy of ± 2 cm, with no ambiguity and 1 ns resolution thanks to the sharp and aperiodic autocorrelation peak. The resolution (peak width) is limited to 1 ns by the 500 MHz bandwidth of the receiver.

The correlator-based receiver approach used here (Figure 4.28) is one commonly implemented in the noise radar literature. In general, its correlator can be analog [82] or digital [98]. Digital correlators, as used here, are bandwidth-limited by the sampling speed of the digital receiver, here 500 MHz, which may be significantly less than is afforded by many-GHz analog components. This bandwidth limit restricts the sharpness of the peak, i.e. restricts the resolution. However, the digital approach is more flexible, since any arbitrary delay can be detected. In contrast, the analog approach will output the correlation of the transmitted signal and the reflected signal only at a single delay. Thus the analog receiver is useful for high-resolution proximity detection where there is a single delay of interest, but the digital approach allows ranging at any arbitrary distance.

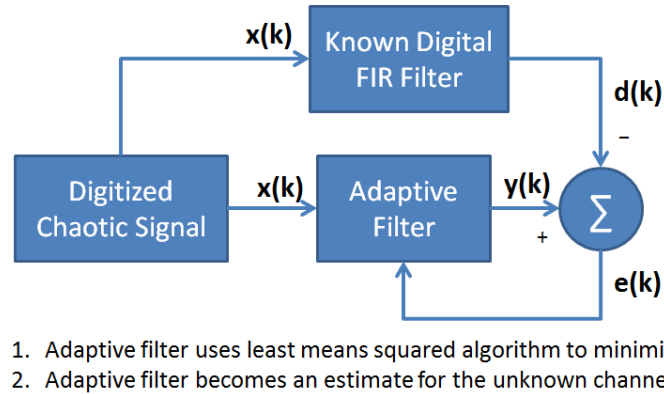


Figure 4.29: Channel Identification Setup Using Broadband Signal

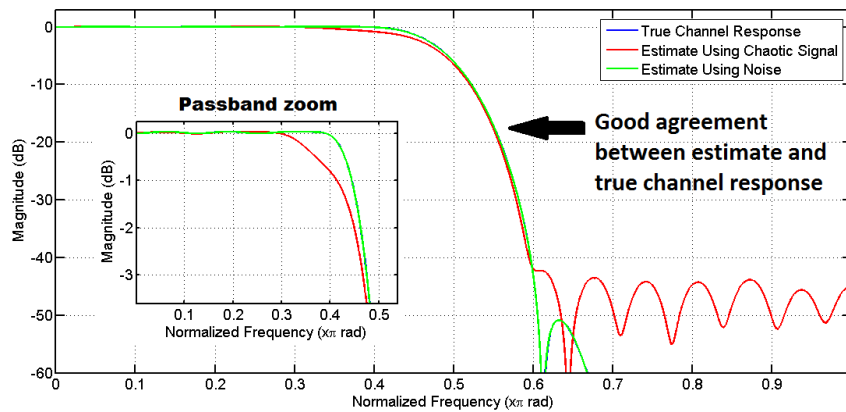


Figure 4.30: Channel Identification Results Using Noise and Chaotic Signals

4.3.2 Channel Identification

A second proposed use of this wideband noiselike signal is for channel identification, as proposed in Figure 3.26. Here we show that by using the signal to drive an adaptive filter, we can force the filter to match the channel, and thus estimate the modulation frequency response of the channel. This will be useful for determining the best operating conditions for wideband signals, since some frequency regions may be severely attenuated relative to others.

The proof-of-concept experiment is shown in Figure 4.29. Such a setup is commonly used in communications systems when equalization of the communications channel is desired; white noise or a random training signal are usually used, but

the wideband noiselike properties of the chaotic laser make it well-suited for this purpose. As shown, the signal $x(k)$ is split and sent into both the unknown channel to be characterized and into an adaptive filter running a least-means-squared error minimization algorithm. The filter coefficients then adjust to minimize the difference (error) $e(k)$ between the signal shaped by the unknown channel $d(k)$, and the signal shaped by the adaptive filter $y(k)$. When the error goes to zero, the adaptive filters response is known to match the unknown channels. Here, a known filter is used as the channel, and its response is compared with the adaptive filters estimation. As shown in Figure 4.30, using the chaotic signal yields results nearly as good as using wideband Gaussian noise. The close comparison validates the approach, which will be used in upcoming experiments to probe water channels.

CHAPTER 5

CONCLUSION

5.1 Transmitter Design and Experimental Results

This thesis has presented a new lidar transmitter developed to meet detailed specifications for the underwater environment. This transmitter addresses the two main challenges of water absorption and particle scattering by operating at high frequency in the green. Moreover, it generates a wideband noiselike signal useful for high resolution, unambiguous ranging, imaging, and detection, as well as for channel identification.

This transmitter is unique in several ways.

1. This is the first known fiber laser used for wideband noise lidar (equivalently “chaotic radar/lidar” or “chaotic signal radar/lidar”).
2. In particular the ultralong cavity was very successful in enhancing the chaotic mode interactions and thus allowing high resolution ranging. This was a novel development, as was the comparison of chaotic behaviors between long and ultralong cavity fiber lasers.
3. This is the first application of chaotic lidar to the underwater environment, i.e. the first chaotic lidar transmitter operating at moderate powers in the blue-green.
4. This is to our knowledge the first blue-green transmitter capable of full modulation depth at arbitrary frequencies above 500 MHz; that it is also wideband and scalable to high powers make it completely unique among blue-green transmitters.
5. The feedback-reflector fiber laser topology is novel in that it is designed for efficient stationary wideband signal generation at 1064 nm. Previous fiber lasers have been either single-frequency at 1064 nm or have been wideband at 1550 nm using components that do not allow efficient use at 1064 nm.

6. The use of a wideband signal for underwater channel identification is new, and the expected data collected will be the first known high-resolution, instantaneous modulation frequency response of underwater channels.

The transmitter was designed using analytical and numerical calculation including dynamic simulation of amplifiers. The transmitter as built met the desired specifications, delivering the high-frequency wideband signal at 532 nm for use underwater. The chaotic behavior is pronounced and easily characterized, and the autocorrelation is sharp and unambiguous. The optical wavelength is effectively controlled both at the seed and through the frequency doubling circuit. The crystal output modulation faithfully reproduces the input modulation, and the power level is sufficient for demonstration of the desired applications underwater.

5.2 Application Experimental Results

Ranging and channel characterization experiments were performed, demonstrating the usefulness of the laser for underwater work.

The proof-of-concept ranging experiment showed digitizer-limited ± 2 cm accuracy in measuring the distance to a target. This result was obtained using a 500 MHz digital receiver that provides unambiguous rangefinding at any distance. This result could be improved even further with a higher speed receiver, since the resolution is inversely proportional to the system bandwidth, and the transmitter signal extends well beyond 500 MHz.

Channel identification is also demonstrated using the transmitter. We probed an "unknown channel" — for proof-of-concept, a known FIR filter — with the wideband signal and determined its frequency response using an adaptive filter running an LMS algorithm. Convergence to the correct coefficients occurred on the order of 10 μ s. Again, the bandwidth of the receiver, rather than the transmitter, was the limit on performance: using 500 MHz the estimate was good but not exact. Performance would be improved by a wider receiver bandwidth.

These experiments provide two paths toward the practical application of this chaotic transmitter.

5.3 Future Work

This thesis documents a transmitter that is nearing its final form [99]. Several improvements should be made on the transmitter itself to increase the output power efficiency, and engineering of the system for packaging and mobility must be done for some applications. Nonetheless, the transmitter is now at a stage when productive work can begin.

The efficiency of the transmitter can be boosted significantly with a few small changes:

- Polarization control should be enforced to maximize frequency doubling efficiency. Currently, there is a strong elliptical polarization, and since the SHG crystal operates only on a single polarization, all non-linearly polarized light is wasted. Thus polarization controllers should be added to ensure linear polarization.
- Spatial mode control should be attempted to improve amplifier conversion efficiency. Currently, the efficiency of the amplifiers lags the projected efficiency significantly, and experiment indicates that some signal light is traveling in the fiber cladding, rather than in the doped core. This light will not be amplified, and should be restricted to the core by tightened fiber windings or other physical techniques.
- A resonator that allowed multiple passes through the frequency doubler would improve efficiency dramatically. While single-pass efficiency at 1 W infrared input is below 1%, reports of >80% efficiency from a resonator are common using free-space resonators [11]. Such a structure would reduce the infrared power requirement dramatically, saving cost, space, and weight from power supplies, pump laser diodes, and fiber.

Application tests will be performed using the chaotic transmitter. Ranging in turbid water can be demonstrated immediately. A synchronized scanner and digital receiver must be designed and implemented for 3D imaging, but that too is within reach. Channel identification for underwater environments of interest can be best performed with the help of a large-aperture collector (i.e. photo-multiplier tube)

that allows collection of scattered light. Water science applications will be explored, particularly investigating if modulation frequency response can help identify particle composition. Channel equalization is the next step beyond channel identification, and may be valuable for improving signal fidelity in underwater communications and imaging.

Longer-term goals for the transmitter include a means of bandwidth control on the transmitter so as not to waste power transmitting outside the receiver's operating bandwidth. Active control of the chaotic waveform may be possible by insertion of a modulator in the cavity, which could either encode a message as an amplitude modulation on the chaos, or it could perturb the cavity in a deterministic and repeatable way that would lead to easily identifiable parameter changes in the signal. Chaotic communications or ranging performance at poor SNR could be dramatically enhanced by synchronization of chaos at the transmitter and receiver [18, 19]. Finally, restricting the lasing to a controllable single mode may well be possible using a saturable absorber and a modulator. Such an approach could allow wideband transmission of more conventional radar signals such as FDR and FMCW, with 100% modulation depth even at high frequencies.

REFERENCES

- [1] Linda J Mullen, Amarildo JC Vieira, PR Herezfeld, and Vincent M Contarino. Application of RADAR technology to aerial LIDAR systems for enhancement of shallow underwater target detection. *Microwave Theory and Techniques, IEEE Transactions on*, 43(9):2370–2377, 1995.
- [2] Seibert Q Duntley. Underwater lighting by submerged lasers and incandescent sources. Technical report, DTIC Document, 1971.
- [3] T. Wiener and S. Karp. The Role of Blue/Green Laser Systems in Strategic Submarine Communications. *Communications, IEEE Transactions on*, 28(9):1602–1607, Sep 1980.
- [4] Frank Hanson and Stojan Radic. High bandwidth underwater optical communication. *Appl. Opt.*, 47(2):277–283, Jan 2008.
- [5] Curtis D Mobley and Charles D Mobley. *Light and water: Radiative transfer in natural waters*, volume 592. Academic press San Diego, CA, 1994.
- [6] Theodore G Pavlopoulos. Blue-Green Dye Lasers for Underwater Illumination. *Naval engineers journal*, 114(4):31–40, 2002.
- [7] C. H. Whitlock, L. R. Poole, J. W. Usry, W. M. Houghton, W. G. Witte, W. D. Morris, and E. A. Gurganus. Comparison of reflectance with backscatter and absorption parameters for turbid waters. *Appl. Opt.*, 20(3):517–522, Feb 1981.
- [8] CJ Funk, SB Bryant, and PJ Heckman Jr. Handbook of underwater imaging system design. Technical report, DTIC Document, 1972.
- [9] Jules S Jaffe, Kad D Moore, John McLean, and MP Strand. Underwater optical imaging: status and prospects. *Oceanography*, 14(3):66–76, 2001.
- [10] William J Kozlovsky, CD Nabors, and Robert L Byer. Efficient second harmonic generation of a diode-laser-pumped CW Nd: YAG laser using monolithic MgO: LiNbO₃ external resonant cavities. *Quantum Electronics, IEEE Journal of*, 24(6):913–919, 1988.
- [11] ZY Ou, SF Pereira, ES Polzik, and H Jeffrey Kimble. 85% efficiency for cw frequency doubling from 1.08 to 0.54, μm . *Optics letters*, 17(9):640–642, 1992.
- [12] D. J. Richardson, J. Nilsson, and W. A. Clarkson. High power fiber lasers: current status and future perspectives [Invited]. *J. Opt. Soc. Am. B*, 27(11):B63–B92, Nov 2010.

- [13] Vincent Jezequel, Frederic Audo, Fabrice Pellen, and Bernard Le Jeune. Experimentally based simulations on modulated lidar for shallow underwater target detection and localization. *SPIE Remote sensing of the ocean, sea ice, and large water regions*, 7825:78250E1–14, 2010.
- [14] Brandon Cochenour, Linda Mullen, and John Muth. Modulated pulse laser with pseudorandom coding capabilities for underwater ranging, detection, and imaging. *Applied Optics*, 50(33):6168–6178, 2011.
- [15] QL Williams, J Garcia-Ojalvo, and Rajarshi Roy. Fast intracavity polarization dynamics of an erbium-doped fiber ring laser: Inclusion of stochastic effects. *Physical Review A*, 55(3):2376, 1997.
- [16] Luke Rumbaugh, William D Jemison, Yifei Li, and Todd A Wey. Wide bandwidth source for high resolution ranging. In *Ultra-Wideband (ICUWB), 2012 IEEE International Conference on*, pages 482–485. IEEE, 2012.
- [17] V Roy, M Piche, F Babin, and G Schinn. Nonlinear wave mixing in a multilongitudinal-mode erbium-doped fiber laser. *Optics express*, 13(18):6791–6797, 2005.
- [18] Gregory D Vanwiggeren and Rajarshi Roy. Communication with chaotic lasers. *Science*, 279(5354):1198–1200, 1998.
- [19] WT Wu, YH Liao, and FY Lin. Noise suppressions in synchronized chaos lidars. *Opt. Express*, 18(25):26155–26162, 2010.
- [20] VA Del Grosso. Modulation transfer function of water. In *OCEAN 75 Conference*, pages 331–347. IEEE, 1975.
- [21] R Urick. Principles of Underwater Sound for Engineers, 1967.
- [22] Brandon M Cochenour, Linda J Mullen, and Alan E Laux. Characterization of the beam-spread function for underwater wireless optical communications links. *Oceanic Engineering, IEEE Journal of*, 33(4):513–521, 2008.
- [23] Theodore J Petzold. Volume scattering functions for selected ocean waters. Technical report, DTIC Document, 1972.
- [24] Dominic M Di Toro. Optics of turbid estuarine waters: approximations and applications. *Water research*, 12(12):1059–1068, 1978.
- [25] Brandon Cochenour. *Experimental Measurements of Temporal Dispersion for Underwater Laser Communications and Imaging*. PhD thesis, N. Carolina State Univ., 2013.

- [26] F Pellen, X Intes, P Olivard, Y Guern, J Cariou, and J Lotrian. Determination of sea-water cut-off frequency by backscattering transfer function measurement. *Journal of Physics D: Applied Physics*, 33(4):349, 2000.
- [27] Brandon Cochenour, Linda Mullen, and Alan Laux. Spatial and temporal dispersion in high bandwidth underwater laser communication links. In *Military Communications Conference, 2008. MILCOM 2008. IEEE*, pages 1–7. IEEE, 2008.
- [28] Linda Mullen, Alan Laux, and Brandon Cochenour. Propagation of modulated light in water: implications for imaging and communications systems. *Applied optics*, 48(14):2607–2612, 2009.
- [29] Joseph M Schmitt. Optical coherence tomography (OCT): a review. *Selected Topics in Quantum Electronics, IEEE Journal of*, 5(4):1205–1215, 1999.
- [30] Linda J Mullen and V Michael Contarino. Hybrid lidar-radar: seeing through the scatter. *Microwave Magazine, IEEE*, 1(3):42–48, 2000.
- [31] Paul Perez, William D Jemison, Linda Mullen, and Alan Laux. Techniques to enhance the performance of hybrid lidar-radar ranging systems. In *Oceans, 2012*, pages 1–6. IEEE, 2012.
- [32] D. G. Illig, L. K. Rumbaugh, L. J. Mullen, and W. D. Jemison. Frequency Domain Reflectometry for Unambiguous High Resolution Ranging in Underwater Lidar. Submitted to Oceans 2013.
- [33] Linda Mullen, Alan Laux, Brian Concannon, Eleonora P. Zege, Iosif L. Katsev, and Alexander S. Prikhach. Amplitude-Modulated Laser Imager. *Appl. Opt.*, 43(19):3874–3892, Jul 2004.
- [34] Linda Mullen, Alan Laux, Brandon, Eleonora P. Zege, Iosif L. Katsev, and Alexander S. Prikhach. Demodulation techniques for the amplitude modulated laser imager. *Appl. Opt.*, 46(30):7374–7383, Oct 2007.
- [35] Alan Laux, Linda Mullen, Paul Perez, and Eleonora Zege. Underwater laser range finder. In *Proc. of SPIE Vol*, volume 8372, pages 83721B–1, 2012.
- [36] Karl D Moore and Jules S Jaffe. Time-evolution of high-resolution topographic measurements of the sea floor using a 3-D laser line scan mapping system. *Oceanic Engineering, IEEE Journal of*, 27(3):525–545, 2002.
- [37] F Pellen, P Olivard, Y Guern, J Cariou, and J Lotrian. Radio frequency modulation on an optical carrier for target detection enhancement in sea-water. *Journal of Physics D: Applied Physics*, 34(7):1122, 2001.

- [38] Gary C Guenther and Robert WL Thomas. Depth measurement biases for an airborne laser bathymeter. In *Proceedings 4th Laser Hydrography Symposium, ERL-0193-SD*, pages 428–452. DTIC Document, 1980.
- [39] Georges R Fournier, Deni Bonnier, J Luc Forand, and Paul W Pace. Range-gated underwater laser imaging system (Journal Paper). *Optical Engineering*, 32(09):2185–2190, 1993.
- [40] William C Cox, Jim A Simpson, Carlo P Domizioli, John F Muth, and Brian L Hughes. An underwater optical communication system implementing Reed-Solomon channel coding. In *OCEANS 2008*, pages 1–6. IEEE, 2008.
- [41] Donna M Kocak, Fraser R Dalgleish, Frank M Caimi, and Yoav Y Schechner. A focus on recent developments and trends in underwater imaging. *Marine Technology Society Journal*, 42(1):52–67, 2008.
- [42] Thorlabs Inc. Model APD210. High-Speed Avalanche Silicon Detector specification.
<http://thorlabs.com/thorProduct.cfm?partNumber=APD210/>, March 2013.
- [43] Thorlabs Inc. Model PMM01. High Gain, Low Dark Current Amplified Photomultiplier Tube.
<http://thorlabs.com/thorProduct.cfm?partNumber=PMM01/>, March 2013.
- [44] L Mullen, PR Herczfeld, and M Contarino. Analytical and experimental evaluation of an optical fiber ocean mass simulator. *Microwave and Guided Wave Letters, IEEE*, 4(1):17–19, 1994.
- [45] Gottfried Mandlbauer, M Pfennigbauer, F Steinbacher, and N Pfeifer. Potential of a novel airborne hydrographic laser scanner for capturing shallow water bodies. In *EGU General Assembly Conference Abstracts*, volume 14, page 8378, 2012.
- [46] Gary C Guenther. Airborne laser hydrography: System design and performance factors. Technical report, DTIC Document, 1985.
- [47] MF Penny, RH Abbot, DM Phillips, B Billard, D Rees, DW Faulkner, DG Cartwright, B Woodcock, GJ Perry, PJ Wilsen, et al. Airborne laser hydrography in Australia. *Applied optics*, 25(13):2046–2058, 1986.
- [48] Paul E LaRocque and Geraint R West. Airborne laser hydrography: an introduction. In *Proc. ROPME/PERSGA/IHB Workshop on Hydrographic Activities in the ROPME Sea area and Red Sea*, volume 4, pages 1–15, 1999.
- [49] Optech Inc. Coastal Zone Mapping and Imaging Lidar. Summary Specification Sheet.

- <http://www.optech.ca/pdf/CZMIL-specsheet-121105-WEB.pdf>, March 2013.
- [50] Airborne Hydrography AB Model Hawkeye II. Technical Specification. <http://www.airbornehydro.com/hawkeye-ii-technical-specification/>, March 2013.
 - [51] Fugro LADS Corp. Model LADS Mk 3. Datasheet. <http://www.fugrolads.com/download/datasheets/Fugro-LADS-Mk3>, March 2013.
 - [52] Riegl Laser Measurement Systems GmbH Model VQ-820-Q. Datasheet. <http://www.riegl.com/nc/products/airborne-scanning/produktdetail/product/scanner/32/>, March 2013.
 - [53] EA McLean, HR Burris Jr, MP Strand, et al. Short-pulse range-gated optical imaging in turbid water. *Applied optics*, 34(21):4343–4351, 1995.
 - [54] Alexei Kouzoubov, Michael J Brennan, and John C Thomas. Treatment of polarization in laser remote sensing of ocean water. *Applied optics*, 37(18):3873–3885, 1998.
 - [55] John W McLean. High resolution 3-D underwater imaging. In *Proc. SPIE*, volume 3761, pages 10–19, 1999.
 - [56] Bryan Coles. Laser line scan systems as environmental survey tools. *Ocean News & Technology [Ocean News Technology]*, 3(4):22–27, 1997.
 - [57] L. Mullen, A. Laux, B. Cochenour, and W. McBride. Extended range underwater imaging using a time varying intensity (TVI) approach. In *OCEANS 2009, MTS/IEEE Biloxi - Marine Technology for Our Future: Global and Local Challenges*, pages 1–8, Oct.
 - [58] Andreas Arnold-Bos, Jean-Philippe Malkasse, and Gilles Kervern. Towards a model-free denoising of underwater optical images. In *Oceans 2005-Europe*, volume 1, pages 527–532. IEEE, 2005.
 - [59] S. Karp. Optical Communications Between Underwater and Above Surface (Satellite) Terminals. *Communications, IEEE Transactions on*, 24(1):66–81, 1976.
 - [60] JP Singhal and DK Srivastava. Modulation method of laser for underwater communication. *Defence Science Journal*, 34:79–84, 1984.
 - [61] Jeffery J Puschell, Robert J Giannaris, and Larry Stotts. The Autonomous Data Optical Relay Experiment: first two way laser communication between an aircraft and submarine. In *Telesystems Conference, 1992. NTC-92., National*, pages 14–27. IEEE, 1992.

- [62] Judith Bannon Snow, James P Flatley, Dennis E Freeman, Mark A Landry, Carl E Lindstrom, Jacob R Longacre, and Joshua A Schwartz. Underwater propagation of high data rate laser communications pulses. In *Proc. SPIE*, volume 1750, pages 419–427, 1992.
- [63] John W Giles and Isaac N Bankman. Underwater optical communications systems. Part 2: basic design considerations. In *Military Communications Conference, 2005. MILCOM 2005. IEEE*, pages 1700–1705. IEEE, 2005.
- [64] N Fair, AD Chave, Lee Freitag, James Preisig, SN White, Dana Yoerger, and F Sonnichsen. Optical modem technology for seafloor observatories. In *OCEANS 2006*, pages 1–6. IEEE, 2006.
- [65] B. Cochenour, L. Mullen, A. Laux, and T. Curran. Effects of Multiple Scattering on the Implementation of an Underwater Wireless Optical Communications Link. In *OCEANS 2006*, pages 1–6, Sept.
- [66] Davide Anguita, Davide Brizzolara, and Giancarlo Parodi. Building an Underwater Wireless Sensor Network Based on Optical: Communication: Research Challenges and Current Results. In *Sensor Technologies and Applications, 2009. SENSORCOMM'09. Third International Conference on*, pages 476–479. IEEE, 2009.
- [67] Heather Brundage. *Designing a wireless underwater optical communication system*. PhD thesis, Massachusetts Institute of Technology, 2010.
- [68] W.C. Cox, J.A. Simpson, and J.F. Muth. Underwater optical communication using software defined radio over LED and laser based links. In *Military Communications Conference, 2011 - MILCOM 2011*, pages 2057–2062, Nov.
- [69] Mingsong Chen, Shengyuan Zhou, and Tiansong Li. The implementation of PPM in underwater laser communication system. In *Communications, Circuits and Systems Proceedings, 2006 International Conference on*, volume 3, pages 1901–1903. IEEE, 2006.
- [70] Chadi Gabriel, Mohammad-Ali Khalighi, Salah Bourennane, Pierre Léon, and Vincent Rigaud. Investigation of suitable modulation techniques for underwater wireless optical communication. In *Optical Wireless Communications (IWOW), 2012 International Workshop on*, pages 1–3. IEEE, 2012.
- [71] Stephan Lutgen, Adrian Avramescu, Teresa Lerner, Marc Schillgalies, Desiree Queren, J Muller, Dimitri Dini, Andreas Breidenassel, and Uwe Strauss. Progress of blue and green InGaN laser diodes. In *Proc. SPIE*, volume 7616, page 76160G, 2010.

- [72] IPG Photonics. YLS series kW-level CW fiber laser.
http://www.ipgphotonics.com/apps_materials_multi_yls.htm, April 2013.
- [73] RP-Photonics. Frequency Doubling.
http://www.rp-photonics.com/frequency_doubling.html, April 2013.
- [74] Omicron A350 Diode Lasers. Ultra-fast analogue modulation specification.
<http://www.omicron-laser.de/english/lasers/diode-lasers/modulated-lasers/a350.html>, April 2013.
- [75] Osram OS Model PL520. Green light for laser projectors (press release and specification). http://www.osram-os.com/osram_os/en/press/press-releases/ir-devices-and-laser-diodes/2012/green-light-for-laser-projectors/index.jsp?mkturl=pr-greenlaser, April 2013.
- [76] Nichia Model NDG4216. Green laser diode specification. <http://www.nichia.co.jp/specification/en/product/ld/NDG4216-E.pdf>, April 2013.
- [77] IPG Photonics. YLS series 30 ps Q-switched pulsed fiber laser.
http://www.ipgphotonics.com/apps_materials_qswitch.htm, April 2013.
- [78] Nufern. 1.0 um fiber laser offerings.
http://www.nufern.com/pam/fiber_lasers/, April 2013.
- [79] H Lim, F Ilday, and F Wise. Femtosecond ytterbium fiber laser with photonic crystal fiber for dispersion control. *Optics Express*, 10(25):1497–1502, 2002.
- [80] DJ Richardson, J Nilsson, and WA Clarkson. High power fiber lasers: current status and future perspectives [Invited]. *JOSA B*, 27(11):B63–B92, 2010.
- [81] Thorlabs Inc. Model LN05S. 40 Gbps Intensity Modulator with Polarizer.
<http://thorlabs.com/thorProduct.cfm?partNumber=LN05S-FC/>, April 2013.
- [82] RM Narayanan, Y Xu, PD Hoffmeyer, and JO Curtis. Design, performance, and applications of a coherent ultra-wideband random noise radar. *Optical Engineering*, 37(6):1855–1869, 1998.
- [83] FY Lin and JM Liu. Chaotic lidar. *Selected Topics in Quantum Electronics, IEEE Journal of*, 10(5):991–997, 2004.
- [84] Yuncai Wang, Bingjie Wang, and Anbang Wang. Chaotic correlation optical time domain reflectometer utilizing laser diode. *Photonics Technology Letters, IEEE*, 20(19):1636–1638, 2008.

- [85] Jeffrey L Rogers, Slaven Peles, and Kurt Wiesenfeld. Model for high-gain fiber laser arrays. *Quantum Electronics, IEEE Journal of*, 41(6):767–773, 2005.
- [86] A. E. Siegman. *Lasers*. University Science Books (Mill Valley, CA, 1986.
- [87] HM Pask, Robert J Carman, David C Hanna, Anne C Tropper, Colin J Mackechnie, Paul R Barber, and Judith M Dawes. Ytterbium-doped silica fiber lasers: versatile sources for the 1-1.2 μm region. *Selected Topics in Quantum Electronics, IEEE Journal of*, 1(1):2–13, 1995.
- [88] John R Marciante and Jonathan D Zuegel. High-gain, polarization-preserving, Yb-doped fiber amplifier for low-duty-cycle pulse amplification. *Applied optics*, 45(26):6798–6804, 2006.
- [89] Xiangfei Chen, Zhichao Deng, and Jianping Yao. Photonic generation of microwave signal using a dual-wavelength single-longitudinal-mode fiber ring laser. *Microwave Theory and Techniques, IEEE Transactions on*, 54(2):804–809, 2006.
- [90] Lei Wei. *Fiber resonators and lasers*. PhD thesis, University of Waterloo, 2000.
- [91] Y Cheng, JT Kringlebotn, WH Loh, RI Laming, and DN Payne. Stable single-frequency traveling-wave fiber loop laser with integral saturable-absorber-based tracking narrow-band filter. *Optics letters*, 20(8):875–877, 1995.
- [92] Rudiger Paschotta, Johan Nilsson, Anne C Tropper, and David C Hanna. Ytterbium-doped fiber amplifiers. *Quantum Electronics, IEEE Journal of*, 33(7):1049–1056, 1997.
- [93] Ido Kelson and Amos A Hardy. Strongly pumped fiber lasers. *Quantum Electronics, IEEE Journal of*, 34(9):1570–1577, 1998.
- [94] Yong Wang and Hong Po. Dynamic characteristics of double-clad fiber amplifiers for high-power pulse amplification. *Lightwave Technology, Journal of*, 21(10):2262–2270, 2003.
- [95] Thorlabs Catalog. PPLN Tutorial. www.thorlabs.com/catalogpages/693.pdf, April 2013.
- [96] RP-Photonics. Rayleigh length. http://www.rp-photonics.com/rayleigh_length.html, April 2013.
- [97] Newport. Gaussian optics tutorial. <http://www.newport.com/servicesupport/tutorials/default.aspx?id=112>, April 2013.

- [98] Chieh-Ping Lai and Ram M Narayanan. Ultrawideband random noise radar design for through-wall surveillance. *Aerospace and Electronic Systems, IEEE Transactions on*, 46(4):1716–1730, 2010.
- [99] L. K. Rumbaugh, E. M. Bollt, Y. Li, and W. D. Jemison. A 532 nm Chaotic Lidar Transmitter for High Resolution Underwater Ranging and Imaging. Submitted to Oceans 2013.